Davis, E.E., Fisher, A.T., Firth, J.V., et al., 1997
Proceedings of the Ocean Drilling Program, Initial Reports, Vol. 168

5. ROUGH BASEMENT TRANSECT (SITES 1026 AND 1027)[1]

Shipboard Scientific Party[2]

HOLE 1026A

Position: 47°45.757′N, 127°45.552′W

Start hole: 0615 hr, 30 June 1996

End hole: 0430 hr, 1 July 1996

Time on hole: 22.25 hr (0.93 days)

Seafloor (drill pipe measurement from rig floor, mbrf): 2669.1

Total depth (drill pipe measurement from rig floor, mbrf): 2770.5

Distance between rig floor and sea level (m): 11.0

Water depth (drill pipe measurement from sea level, m): 2658.1

Penetration (mbsf): 101.4

Coring totals:
  Type: APC; Number: 12; Cored: 101.4 m; Recovered: 105.57 m (104.1%)

Formation:
  Unit I: 0−101.4 mbsf; Quaternary
    Interbeds of sand and silt turbidites, sandy debris flows, and hemipelagic mud

HOLE 1027A

Position: 47°45.412′N, 127°43.854′W

Start hole: 0545 hr, 1 July 1996

End hole: 0845 hr, 1 July 1996

Time on hole: 3.00 hr (0.13 days)

Seafloor (drill pipe measurement from rig floor, mbrf): no mudline

Total depth (drill pipe measurement from rig floor, mbrf): 2677.5

Distance between rig floor and sea level (m): 11.0

Water depth (drill pipe measurement from sea level, m): 2657.0

Penetration (mbsf): 9.5

Coring totals:
  Type: APC; Number: 1; Cored: 9.5 m; Recovered: 9.92 m (104.4%)

Formation:
  Unit I: 0−9.5 mbsf; Quaternary
    Hemipelagic mud

HOLE 1027B

Position: 47°45.412′N, 127°43.853′W

Start hole: 0845 hr, 1 July 1996

End hole: 0945 hr, 6 July 1996

Time on hole: 121.00 hr (5.04 days)

Seafloor (drill pipe measurement from rig floor, mbrf): 2668.3

Total depth (drill pipe measurement from rig floor, mbrf): 3246.2

Distance between rig floor and sea level (m): 11.0

Water depth (drill pipe measurement from sea level, m): 2657.3

Penetration (mbsf): 577.9

Coring totals:
  Type: APC; Number: 10; Cored: 87.7 m; Recovered: 77.82 m (88.7%)
  Type: XCB; Number: 52; Cored: 490.2 m; Recovered: 337.09 m (68.8%)
  Total: Number: 62; Cored: 577.9 m; Recovered: 414.91 m (71.8%)

Formation:
  Unit I: 0−466.95 mbsf; Quaternary
    Interbeds of sand and silt turbidites, sandy debris flows, and hemipelagic mud
  Unit II: 466.95−568.85 mbsf; Pliocene
    Hemipelagic mud/stone
  Unit III and Units 1 and 2: 568.85−577.90 mbsf; Pliocene
    Basalt talus and hemipelagic mudstone

HOLE 1027C

Position: 47°45.387′N, 127°43.867′W

Start hole: 0945 hr, 6 July 1996

End hole: 1745 hr, 11 July 1996

Time on hole: 128.0 hr (5.33 days)

Seafloor (drill pipe measurement from rig floor, mbrf): 2667.3

Total depth (drill pipe measurement from rig floor, mbrf): 3252.1

Distance between rig floor and sea level (m): 11.2

Water depth (drill pipe measurement from sea level, m): 2656.1

Penetration (mbsf): 584.8

Coring totals:
  Type: 14Ω-in tricone; Number: 0; Cored: 0 m; Recovered: 0 m (0.0%)

HOLE 1026B

Position: 47°45.759′N, 127°45.552′W

Start hole: 1745 hr, 11 July 1996

End hole: 0915 hr, 15 July 1996

Time on hole: 87.5 hr (3.65 days)

Seafloor (drill pipe measurement from rig floor, mbrf): 2669.1

Total depth (drill pipe measurement from rig floor, mbrf): 3252.1

Distance between rig floor and sea level (m): 11.2

Water depth (drill pipe measurement from sea level, m): 2657.9

Penetration (mbsf): 256.0

---

[1] Davis, E.E., Fisher, A.T., Firth, J.V., et al., 1997. *Proc. ODP, Init. Repts,* 168: College Station, TX (Ocean Drilling Program).

[2] Shipboard Scientific Party is given in the list preceding the Table of Contents.

Previous Chapter
Table of Contents
Next Chapter

Coring totals:
Type: 14¾-in tricone; Number: 0; Cored: 0.0 m; Recovered: 0 m (0.0%)

HOLE 1027C

Position: 47°45.387′N, 127°43.867′W

Continue hole: 0915 hr, 15 July 1996

End hole: 0730 hr, 17 July 1996

Time on hole: 46.25 hr (1.93 days)

Seafloor (drill pipe measurement from rig floor, mbrf): 2667.3

Total depth (drill pipe measurement from rig floor, mbrf): 3299.7

Distance between rig floor and sea level (m): 11.2

Water depth (drill pipe measurement from sea level, m): 2656.1

Penetration (mbsf): 632.4

Coring totals:
Type: RCB; Number: 5; Cored: 47.6 m; Recovered: 29.13 m (61.2%)

Formation:
Unit 3: 584.8–594.4 mbsf; Pliocene
Diabase
Unit III: 594.4–606.3 mbsf; Pliocene
Mudstone
Unit 4: 606.3–632.4 mbsf; Pliocene
Basalt

HOLE 1026B

Position: 47°45.759′N, 127°45.552′W

Continue hole: 0730 hr, 17 July 1996

End hole: 1730 hr, 19 July 1996

Time on hole: 58.00 hr (2.42 days)

Seafloor (drill pipe measurement from rig floor, mbrf): 2669.1

Total depth (drill pipe measurement from rig floor, mbrf): 2964.3

Distance between rig floor and sea level (m): 11.2

Water depth (drill pipe measurement from sea level, m): 2657.9

Penetration (mbsf): 295.2

Coring totals:
Type: RCB; Number: 5; Cored: 39.2 m; Recovered: 1.95 m (5.0%)

Formation:
Unit 1: 256.0–267.4 mbsf; Pliocene
Basalt
Unit 2: 267.4–277.0 mbsf; Pliocene
Basalt breccia
Unit 3: 277.0–295.2 mbsf; Pliocene
Basalt

HOLE 1027C

Position: 47°45.387′N, 127°43.867′W

Continue hole: 1730 hr, 19 July 1996

End hole: 2100 hr, 21 July 1996

Time on hole: 51.50 hr (2.15 days)

Seafloor (drill pipe measurement from rig floor, mbrf): 2667.3

Total depth (drill pipe measurement from rig floor, mbrf): 3299.7

Distance between rig floor and sea level (m): 11.2

Water depth (drill pipe measurement from sea level, m): 2656.1

Penetration (mbsf): 632.4

Remarks: conducted packer tests; installed CORK

HOLE 1026B

Position: 47°45.759′N, 127°45.552′W

Continue hole: 2100 hr, 21 July 1996

End hole: 1700 hr, 22 July 1996

Time on hole: 20.0 hr (0.83 days)

Seafloor (drill pipe measurement from rig floor, mbrf): 2669.1

Total depth (drill pipe measurement from rig floor, mbrf): 2964.3

Distance between rig floor and sea level (m): 11.2

Water depth (drill pipe measurement from sea level, m): 2657.9

Penetration (mbsf): 295.2

Remarks: installed drill string liner at base of hole

HOLE 1026C

Position: 47°46.261′N, 127°45.186′W

Start hole: 1345 hr, 2 August 1996

End hole: 0545 hr, 4 August 1996

Time on hole: 40.00 hr (1.67 days)

Seafloor (drill pipe measurement from rig floor, mbrf): 2669.1

Total depth (drill pipe measurement from rig floor, mbrf): 2917.3

Distance between rig floor and sea level (m): 11.3

Water depth (drill pipe measurement from sea level, m): 2657.8

Penetration (mbsf): 248.2

Coring totals:
Type: RCB; Number: 17; Cored: 163.6 m; Recovered: 49.8 m (30.4%)

Formation:
Unit I: 84.6–216.13 mbsf; Quaternary
Interbeds of sand and silt turbidites and hemipelagic mud
Unit II: 216.13–228.9 mbsf; Quaternary
Hemipelagic mud
Unit 1: 228.9–248.2 mbsf; Pliocene
Basalt

HOLE 1026B

Position: 47°45.759′N, 127°45.552′W

Continue hole: 0545 hr, 4 August 1996

End hole: 0800 hr, 5 August 1996

Time on hole: 26.25 hr (1.09 days)

Remarks: checked hole depth and sampled basement fluids with WSTP

HOLE 1026B

Position: 47°45.759′N, 127°45.552′W

Continue hole: 2045 hr, 6 August 1996

End hole: 1830 hr, 7 August 1996

Time on hole: 21.75 hr (0.91 days)

Remarks: installed CORK

GEOLOGIC CONTEXT

Objectives for drilling along the Rough Basement Transect (Sites 1026 and 1027) are discussed in detail in the “Introduction and Summary” chapter (this volume), and extensive discussions of site survey data are provided there and in Davis et al., (this volume). The regional context is shown in the composite seismic reflection profile (Fig. 5, “Introduction and Summary” chapter, [back-pocket foldout]). The sites are situated over crust roughly 3.6 Ma in age, 100 km east of the crest of the Juan de Fuca Ridge and roughly 80 km east of the nearest area of extensive basement outcrop.

In brief, the holes at these sites were drilled to determine the differences in the nature and history of basement alteration and in the temperature, pressure, and composition of hydrothermal fluids between a buried basement ridge and an adjacent buried valley to constrain the efficiency of fluid, heat, and solute transport in upper basement rocks. The local geologic context of the sites is illustrated in Figures 1 and 2. The area is characterized by linear basement ridges and troughs produced at the time of crustal creation. These have a characteristic wavelength of several kilometers and a relief of several hundred meters. Regionally, this relief is completely buried by turbidite sediments, although basement rocks are exposed locally in outcrop along two of the ridges where three small volcanic edifices stand above the regionally flat turbidite plain (Fig. 1). Transects of heat-flow measurements across the ridges and the basement outcrops show that (1) basement is maintained at a remarkably uniform temperature (to within 10 K or less) by hydrothermal fluid flow in basement (Davis et al., 1997), despite large local contrasts in sediment burial (conductive conditions would result in temperature differences of up to 50 K), and (2) warm formation water rises through the basement edifices and discharges at the seafloor through the outcrops (Thomson et al., 1995). Extensive pore-fluid geochemical data from the smallest, most southerly outcrops constrain the rate of flow and show that fluids discharge everywhere on the outcrop (M. Mottl, unpubl. data). Scattered samples collected over the basement ridge near the northerly outcrop along the same ridge show that slow upward fluid seepage through the sediment occurs where the ridge is buried by less than about 100 m.

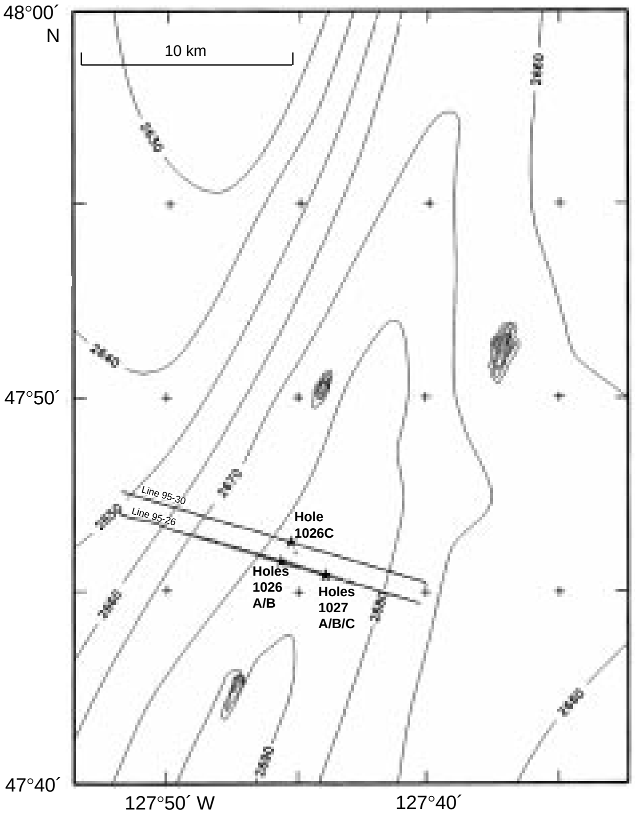

Figure 1. Hole locations and seafloor bathymetry for the Rough Basement drilling transect. Contours are given at 10-m intervals and were calculated assuming a sound velocity of 1500 m/s. Circles indicate locations of nearby heat-flow measurements (Davis et al., this volume).

Site 1026 is located over one of the larger basement ridges in the area, about midway between and roughly 7 km from two of the outcropping basement edifices (Fig. 1), where the local sediment thickness is roughly 250 m (Figs. 2, 3). Site 1027 is located about 2.2 km to the east over the adjacent basement valley, which is buried by as much as 600 m of sediment (Figs. 2, 3). Heat flow measured over the buried ridge (see Davis et al., this volume) reaches a maximum of 353 mW/m^2 at the location of Site 1026 and decreases both to the east and west over the adjacent basement valleys. At the location of Site 1027, the measured seafloor heat flow is 160 mW/m^2, and it reaches a minimum of 150 mW/m^2 over the point of maximum sediment thickness.

In addition to defining the basement topography, the seismic reflection profiles across the Rough Basement sites also provide information about the local sediment depositional history. As at several other locations on the eastern flank of the Juan de Fuca Ridge, basement topography controlled the location of channelized turbidite sediment transport early in the history of sedimentation, and the positions of the distributary channels have remained stable well after the basement ridges were buried. Site 1027 is located in the center of a major distributary channel (Fig. 1) that was initially confined by the basement valley into which holes at this site were drilled (Fig. 2). Site 1026 is located at the western edge of the channel; holes there intersect the contact where the channel deposits onlap onto the sediments of the adjacent levee to the west about halfway through the 250-m-thick section.

OPERATIONS

Site 1026

Hole 1026A

The 3.5-hr transit to Site 1026 (proposed site PP-5A) was brief and uneventful. Once the beacon was deployed, the pipe was run to the seafloor, and advanced hydraulic piston corer (APC) coring commenced. The first core recovered 5.41 m of sediment, which established the mudline 3.3 m higher than the precision depth recorder (PDR) indicated (Table 1). The hole was cored to APC refusal (as defined in this hole by failure to fully stroke). Adara temperature tool measurements were taken on every other core beginning with Core 168-1026A-4H. Drilling operations were routine with no major problems or incidents. Seawater was the only circulation fluid used during the coring operation. The hole was displaced with heavy mud (10.5 lb/gal) before abandonment. After clearing the seafloor with the drill bit, a jet-in test was conducted to determine the amount of 16-in casing (conductor pipe) to be used with the reentry cone for this site. The beacon was left on bottom and turned on because the site was to be reoccupied relatively soon.

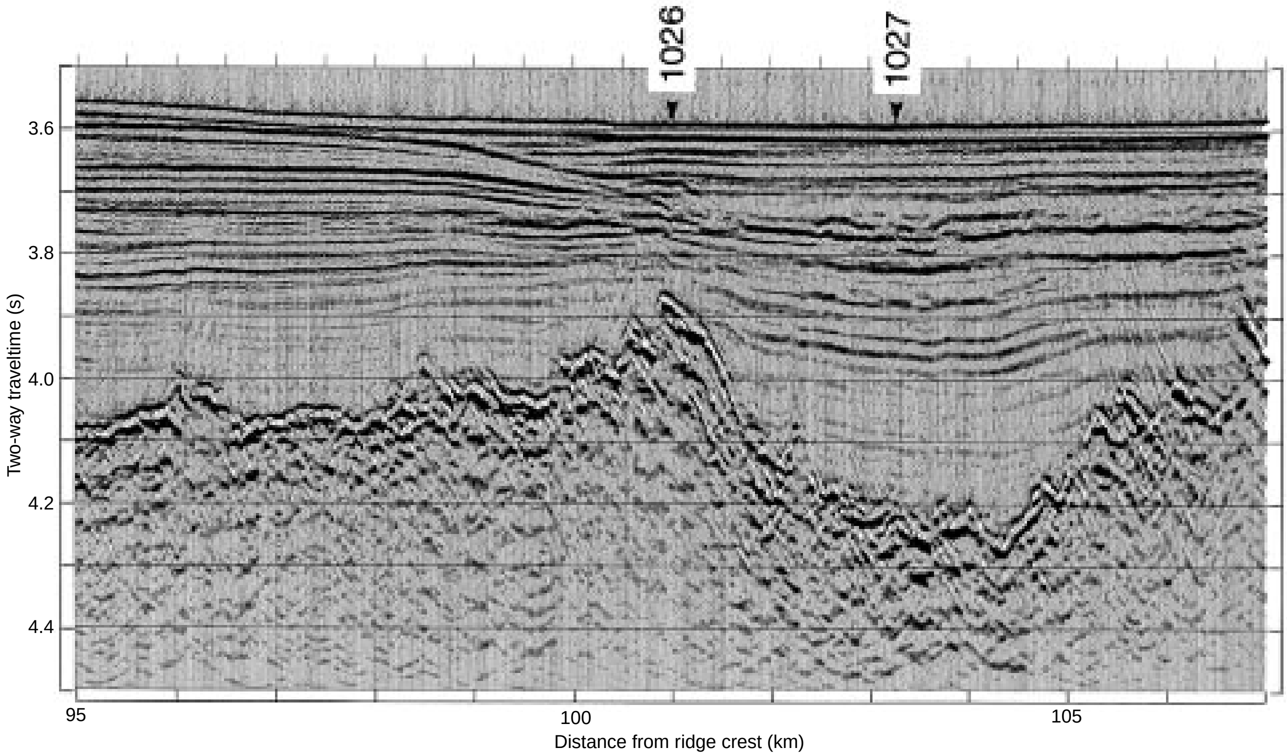

Figure 2. Seismic reflection profile along which holes of the Rough Basement Sites 1026 and 1027 were drilled (see Fig. 4 for location of profiles). All seismic data were collected using a 1.5-L (90-in^3) Generator-Injector gun source and a digital acquisition and processing system operated by the University of Bremen.

Site 1027

Hole 1027A

The drillship was offset 1.2 nmi to Site 1027 (proposed site PP-4A) in dynamic positioning (DP) mode with the drill string suspended in the same manner as on the other DP moves this leg. Based on earlier mudline depths, the bit was positioned 6.4 m above the PDR depth for the first spud attempt. Sediment had been penetrated, but the first core barrel was recovered empty; the core had fallen out of the liner, and thus it was impossible to identify a mudline depth. A second attempt at spudding was made from the same depth, and this time a full core (9.92 m) was recovered (Table 1). The hole was abandoned again for lack of a positive mudline identification. The hole was logged as an official hole (1027A) because the core material was curated and kept for further analysis by the shipboard geochemists. The drill string was officially pulled clear of the seafloor at 0845 hr, ending operations at the hole.

Hole 1027B

After a successful mudline core was recovered, coring in Hole 1027B continued through Core 168-1027B-62X. Basalt pebbles were first identified in Core 60X and became more predominant with each successive core. The hole was terminated at a depth of 3246.2 mbrf (577.9 meters below seafloor [mbsf]) when it was decided not to spend any more time searching for “absolute” basement. Sepiolite mud sweeps of 25 bbl each were circulated approximately every 40–60 m to aid in hole cleaning. Despite the high sand content of the upper formation, the hole remained stable to total depth (TD). There was no indication of fill after connections were made and no increase in pump pressure or drilling torque as the hole proceeded. Once coring operations were concluded, 25 bbl of 15.8-ppg cement was placed in the hole, and the remainder was displaced with heavy mud.

Four Adara temperature measurements were taken in Hole 1027B. The Davis/Villinger Temperature Probe (DVTP) was deployed 18 times. Tool 1 stopped recording during recovery (after Core 40X). Data were ultimately recovered, but it was not a good measurement.

Hole 1027C

The ship was DP offset 50 m on a course of 200°, and a jet-in test was conducted to a depth of 40.0 mbsf. A total of 1 hr, 52 min was required for the test, using a maximum of 50 spm and 10,000 lb weight. After we recovered the drill string, a reentry cone with 16-in casing was made up and deployed. The cone landed at the seafloor after jetting the casing shoe for 2 hr, 39 min at a maximum 52 spm and using 20,000 lb weight. The 16-in casing shoe was placed at 2704.9 m, or 37.6 mbsf. The 16-in Dril-Quip running tool was released, and the drill string was tripped back to the ship. A 14¾-in tricone bit and drilling bottom-hole assembly (BHA) was then made up and tripped to bottom. The cone was reentered at 0150 hr on 8 July 96. A 14¾-in hole was control-drilled to a depth of 3252.1 m (584.8 mbsf), or 9.3 m into basement (575.5 mbsf). A wiper trip was made to the 16-in casing shoe and back with minor overpull and drill pipe drag in spots. An apparent ledge was identified approximately 1 m into basement, and the bit was worked through this area several times. A tight hole and light fill characterized the lower 15 m. Without setting back the top drive, a short (six-stand) wiper trip was made, and the hole was circulated clean then displaced with sepiolite mud. The drill string was recovered, and 41 joints of 10¾-in casing were made up and deployed using the Dril-Quip running tool. After returning to the seafloor with the casing and searching for several hours, it became apparent that the reentry cone had sunk significantly below the mudline. The cone/16-in casing had apparently become undermined during the drilling of the 14¾-in hole. It is theorized that a combination of circulation and vibration liquefied the sandy sediments in the upper por-

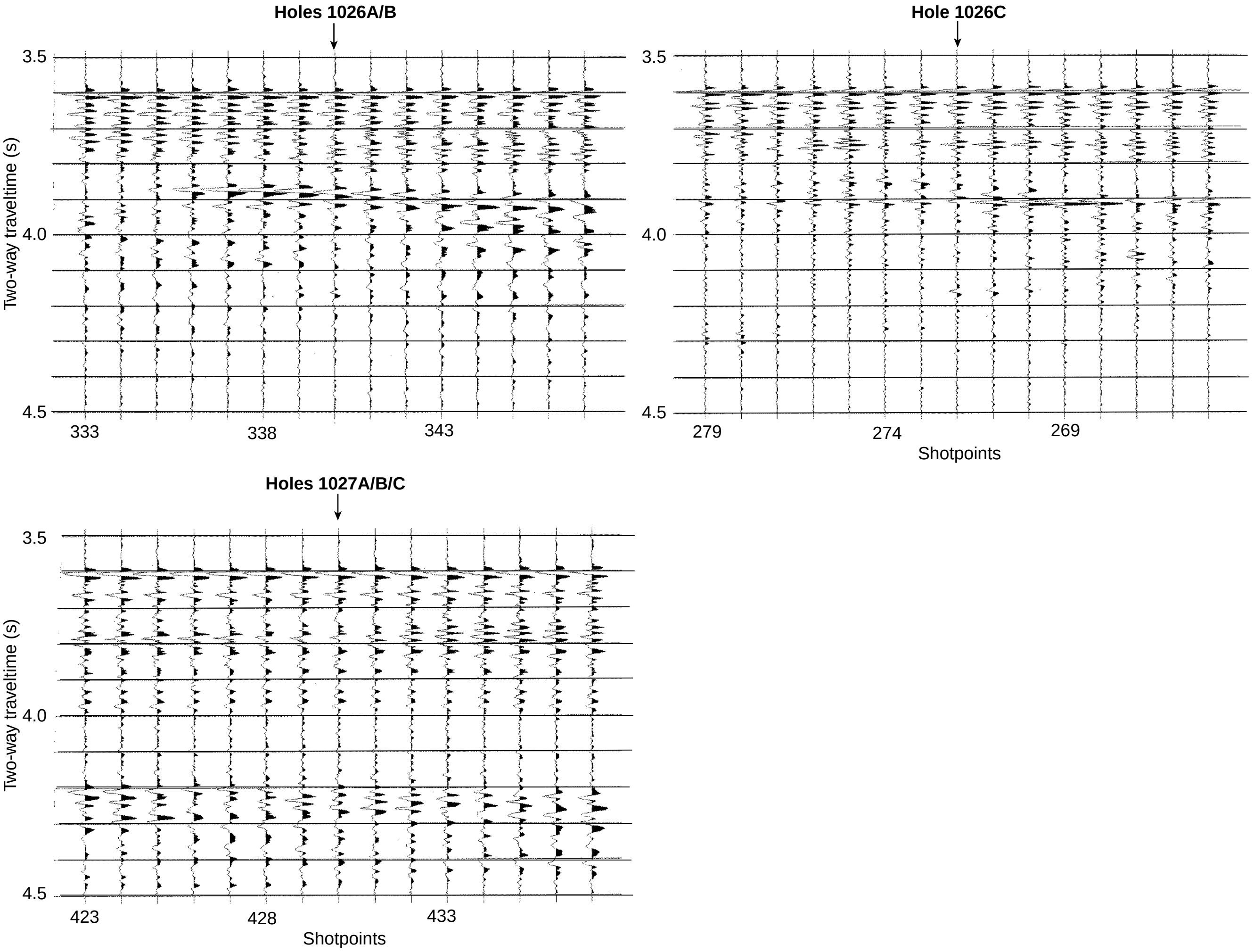

Figure 3. Trace-by-trace seismic reflection data collected in the immediate vicinity of Holes 1026A, 1026B, and 1026C drilled into the buried basement ridge and Holes 1027A through 1027C drilled into the basement valley (see Fig. 4 for locations of drill sites relative to seismic reflection profiles). Shots are spaced 25 m apart.

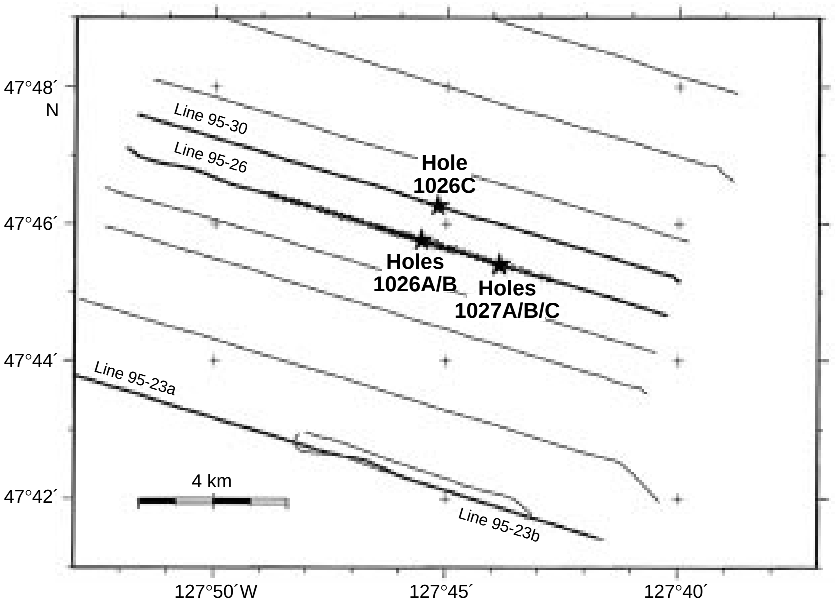

Figure 4. Hole positions along the Rough Basement Transect, along with seismic profile locations. Circles indicate locations of heat-flow measurements.

Table 1. Coring summary for Sites 1026 and 1027.

Core	Date (1996)	Time (UTC)	Depth (mbsf)	Length cored (m)	Length recovered (m)	Recovery (%)
168-1026A-						
1H	30 June	2035	0.0–5.4	5.4	5.41	100.0
2H	30 June	2130	5.4–14.9	9.5	9.87	104.0
3H	30 June	2220	14.9–24.4	9.5	9.91	104.0
4H	30 June	2325	24.4–33.9	9.5	9.78	103.0
5H	1 July	0020	33.9–43.4	9.5	9.93	104.0
6H	1 July	0125	43.4–52.9	9.5	9.51	100.0
7H	1 July	0220	52.9–62.4	9.5	9.72	102.0
8H	1 July	0320	62.4–71.9	9.5	10.27	108.1
9H	1 July	0410	71.9–81.4	9.5	9.93	104.0
10H	1 July	0510	81.4–90.9	9.5	10.12	106.5
11H	1 July	0605	90.9–100.4	9.5	10.08	106.1
12H	1 July	0705	100.4–101.4	1.0	1.04	104.0
Coring totals:				101.4	105.57	104.1
168-1026B-						
1R	18 July	0415	256.0–261.7	5.7	0.27	4.7
2R	18 July	0600	261.7–267.4	5.7	0.16	2.8
3R	18 July	0810	267.4–277.0	9.6	0.61	6.4
4R	18 July	1030	277.0–286.6	9.6	0.34	3.5
5R	18 July	1420	286.6–295.2	8.6	0.57	6.6
Coring totals:				39.2	1.95	5.0
168-1026C-						
1R	3 Aug	0730	84.6–94.2	9.6	0.78	8.1
2R	3 Aug	0915	94.2–103.8	9.6	0.21	2.2
3R	3 Aug	1005	103.8–113.5	9.7	0.52	5.4
4R	3 Aug	1110	113.5–123.1	9.6	1.44	15.0
5R	3 Aug	1255	123.1–132.7	9.6	1.96	20.4
6R	3 Aug	1345	132.7–142.3	9.6	0.58	6.0
7R	3 Aug	1430	142.3–152.0	9.7	1.68	17.3
8R	3 Aug	1605	152.0–161.6	9.6	1.24	12.9
9R	3 Aug	1700	161.6–171.2	9.6	2.66	27.7
10R	3 Aug	1740	171.2–180.8	9.6	8.49	88.4
11R	3 Aug	1935	180.8–190.5	9.7	1.06	10.9
12R	3 Aug	2040	190.5–200.1	9.6	2.51	26.1
13R	3 Aug	2145	200.1–209.7	9.6	8.13	84.7
14R	3 Aug	2345	209.7–219.3	9.6	8.04	83.7
15R	4 Aug	0035	219.3–228.9	9.6	9.79	102.0
16R	4 Aug	0250	228.9–238.5	9.6	0.38	4.0
17R	4 Aug	0730	238.5–248.2	9.7	0.30	3.1
Coring totals:				163.6	49.77	30.4
168-1027A-						
1W	1 July	1520	0.0–9.5	9.5	9.92	104.0
Coring totals:				9.5	9.92	104.0
168-1027B-						
1H	1 July	1615	0.0–4.2	4.2	4.23	101.0
2H	1 July	1700	4.2–13.7	9.5	0.00	0.0
3H	1 July	1750	13.7–23.2	9.5	9.29	97.8
4H	1 July	1850	23.2–32.7	9.5	10.05	105.8
5H	1 July	1950	32.7–42.2	9.5	9.36	98.5
6H	1 July	2055	42.2–51.7	9.5	9.62	101.0
7H	1 July	2145	51.7–61.2	9.5	8.56	90.1
8H	1 July	2300	61.2–70.7	9.5	9.80	103.0
9H	1 July	2355	70.7–80.2	9.5	9.41	99.0
10H	2 July	0055	80.2–87.7	7.5	7.50	100.0
11X	2 July	0255	87.7–97.5	9.8	0.10	1.0
12X	2 July	0355	97.5–107.1	9.6	0.00	0.0
13X	2 July	0450	107.1–116.7	9.6	0.37	3.9
14X	2 July	0655	116.7–126.3	9.6	0.10	1.0
15X	2 July	0745	126.3–135.9	9.6	0.00	0.0
16X	2 July	0840	135.9–145.5	9.6	0.00	0.0
17X	2 July	1035	145.5–155.1	9.6	5.48	57.1
18X	2 July	1135	155.1–164.7	9.6	0.22	2.3
19X	2 July	1235	164.7–174.3	9.6	2.01	20.9
20X	2 July	1445	174.3–183.9	9.6	0.56	5.8
21X	2 July	1625	183.9–193.5	9.6	0.31	3.2
22X	2 July	1815	193.5–203.2	9.7	6.79	70.0
23X	2 July	2240	203.2–212.8	9.6	1.71	17.8
24X	3 July	0030	212.8–222.4	9.6	0.29	3.0
25X	3 July	0230	222.4–232.0	9.6	2.91	30.3
26X	3 July	0525	232.0–241.6	9.6	5.44	56.6
27X	3 July	0705	241.6–251.3	9.7	2.38	24.5
28X	3 July	0825	251.3–260.9	9.6	8.10	84.4
29X	3 July	1055	260.9–270.5	9.6	9.86	103.0
30X	3 July	1230	270.5–280.1	9.6	9.49	98.8
31X	3 July	1355	280.1–289.8	9.7	9.76	100.0
32X	3 July	1620	289.8–299.4	9.6	9.82	102.0
33X	3 July	1745	299.4–309.1	9.7	9.87	102.0
34X	3 July	1915	309.1–318.7	9.6	9.90	103.0
35X	3 July	2200	318.7–328.4	9.7	4.51	46.5
36X	3 July	2345	328.4–338.0	9.6	9.83	102.0
37X	4 July	0130	338.0–347.7	9.7	10.00	103.1
38X	4 July	0415	347.7–357.3	9.6	9.91	103.0
39X	4 July	0615	357.3–367.0	9.7	9.85	101.0
40X	4 July	0805	367.0–376.6	9.6	9.79	102.0
41X	4 July	1040	376.6–386.2	9.6	4.88	50.8
42X	4 July	1215	386.2–395.8	9.6	8.69	90.5
43X	4 July	1515	395.8–405.4	9.6	9.83	102.0
44X	4 July	1655	405.4–415.0	9.6	9.88	103.0
45X	4 July	1835	415.0–424.6	9.6	9.96	104.0
46X	4 July	2145	424.6–434.2	9.6	7.32	76.2
47X	4 July	2330	434.2–443.9	9.7	9.56	98.5
48X	5 July	0125	443.9–453.5	9.6	9.85	102.0
49X	5 July	0410	453.5–463.0	9.5	9.86	104.0
50X	5 July	0705	463.0–472.6	9.6	9.87	103.0
51X	5 July	0735	472.6–482.2	9.6	8.74	91.0
52X	5 July	1020	482.2–491.7	9.5	9.87	104.0
53X	5 July	1225	491.7–501.3	9.6	9.87	103.0
54X	5 July	1435	501.3–511.0	9.7	9.83	101.0
55X	5 July	1805	511.0–520.6	9.6	9.83	102.0
56X	5 July	2020	520.6–530.3	9.7	9.98	103.0
57X	5 July	2315	530.3–539.9	9.6	9.86	103.0
58X	6 July	0100	539.9–549.5	9.6	9.37	97.6
59X	6 July	0405	549.5–559.1	9.6	9.88	103.0
60X	6 July	0645	559.1–568.3	9.2	9.86	107.0
61X	6 July	0925	568.3–572.8	4.5	0.51	11.3
62X	6 July	1210	572.8–577.9	5.1	0.43	8.4
Coring totals:				577.9	414.91	71.8
168-1027C-						
1R	16 July	1420	584.8–594.4	9.6	7.01	73.0
2R	16 July	1600	594.4–604.1	9.7	9.56	98.5
3R	16 July	1950	604.1–613.7	9.6	2.38	24.8
4R	17 July	0125	613.7–623.3	9.6	3.50	36.4
5R	17 July	0705	623.3–632.4	9.1	6.68	73.4
Coring totals:				47.6	29.13	61.2

Notes: UTC = Universal Time Coordinated. For each site, an expanded coring summary table that includes lengths and depths of sections and sampling comments is included on CD-ROM (back pocket).

tion of the hole, allowing the cone to sink 8.3 m below the mudline. Without seeing the cone, the hole was reentered using sonar, and the 10¾-in casing string was deployed until it landed firmly at a depth of 3252.05 m, or essentially hole TD. The string was picked up to no avail three times in an attempt to verify that the casing hanger had engaged. The casing shoe was set down one last time while spotting 56 bbl of neat cement around the casing shoe. When the drill string was raised for the final time, to everyone's surprise and relief the reentry cone and 16-in casing string came up with it. The reentry cone mudskirt was placed 2 m below the original mudline at a depth of 2669.3 mbrf. This positioned the 16- and 10¾-in casing shoes at 2704.9 mbrf (38.6 mbsf) and 3245.7 mbrf (578.4 mbsf), respectively. The 10¾-in shoe was cemented 2.9 m into basement, and the entire rathole below the shoe was also filled with cement. Drill string tension was maintained for 12 hr to support the weight of the cone and casing strings while the cement hardened to an acceptable state. The 10¾-in Dril-Quip running tool disengaged without incident. The cone was left stable, and the surface sediments appeared to have backfilled into the cavity to the bottom of the reentry cone mudskirt. Once the drill string was recovered to a safe depth, the positioning beacon was commanded off, and the vessel began moving in DP mode back to Site 1026 (PP-5A).

Site 1026

Hole 1026B

The ship arrived back on the PP-5A location (Site 1026) before the drill string was completely recovered. The positioning beacon was commanded back on. The Dril-Quip 10¾-in running tool was detorqued, and the drilling line was slipped and cut before preparations began for deployment of the third reentry cone of the leg. After making up three joints of 16-in casing, the reentry cone and casing were deployed to the seafloor. Weather conditions were beginning to deteriorate at this point, so one stand of drill collars above the running tool was left out to facilitate getting the reentry cone through the surge zone of the moon pool as quickly as possible. The cone/casing assembly was deployed to the seafloor. The jetting process required 4 hr, 9 min, with a maximum circulation rate of 51 spm and weight of 25,000 lb. The cone base plate landed solidly at the appropriate mudline depth (2669.1 m), and the 16-in Dril-Quip running tool was released routinely. After recovering the drill string, the 16-in Dril-Quip running tool was detorqued at the rig floor, and the dart was loaded in the cementing swivel in preparation for later cementing operations. A 14¾-in drilling assembly was made up and run to bottom. In spite of heavy weather conditions, the reentry was made in just a few minutes, and the bit was run to the bottom of the jetted 16-in casing. A total of 7.5 hr was required to drill the 14¾-in hole to a firm basement depth of 2916.2 mbrf (247.1 mbsf). Another 3.25 hr of basement drilling brought the hole to a total depth of 2925.1 mbrf (256.0 mbsf). The hole was flushed with 40 bbl of sepiolite, and a wiper trip was made up into the 16-in casing shoe. To allow time for the hole to stabilize and/or cuttings to settle, the subsea camera was deployed to inspect the condition of the reentry cone. The inspection indicated that the cone was in good condition and resting at the seafloor as designed. After recovering the camera, we ran the pipe back to TD, where 20 m of loose fill was identified on bottom. The fill was circulated out to within 1 m of total depth without requiring rotation of the drill string. Another 40-bbl sepiolite mud sweep was pumped, followed by a seawater spacer and enough sepiolite to displace the hole. The drill string was brought back to the surface, and preparations began for making up 18 joints of 10¾-in casing. This process was slowed somewhat by significant vessel motion but was still completed safely and in a timely fashion. The 10¾-in casing string was deployed to the seafloor, and the reentry was made in 45 min. The casing string was run to bottom without any resistance, and latch-in was verified with 10,000 lb overpull. The sepiolite in the hole was displaced out, and 49 bbl of 15.8-ppg class G neat cement was pumped downhole. The subsea release (SSR) plug was released at 2800 psi, and the cementing dart was landed at 1000 psi. Attempts to release the Dril-Quip running tool were unsuccessful, however; the casing hanger and casing string appeared to be rotating with the running tool. At 1700 hr we decided to wait and let the cement harden rather than risk compromising the cement bond and seal with the formation. After waiting 4 hr, the shipboard cement samples were checked, and it was decided that another 2–4 hr should be allowed before attempting to put torque into the running tool. At 0300 hr on 15 July 96, another attempt was made at releasing the running tool. This time the running tool released properly, and the drill string was recovered aboard ship. Once secured, the vessel got under way in DP mode back to reentry Site 1027 (PP-4A).

Return to Hole 1027C

While the ship was moving to Hole 1027C, an attempt to detorque the 10¾-in Dril-Quip running tool was made at the rig floor. This was only partially successful because of the large amount of fine sand that had infiltrated the mechanism.

The drill string with a rotary core barrel (RCB) BHA was run in hole with a center bit installed for drilling out the rubber cementing dart, casing shoe, and wiper plug. Reentry was made swiftly (<15 min), and the bit was run to bottom. The cement was tagged at 3234.7 mbrf (567.4 mbsf), and it took 5 hr to completely drill out to the original TD of 3252.1 mbrf (584.8 mbsf). Continuous RCB coring continued from that depth through interbedded basalt flow units, mudstones, and highly altered basal sediments. Some overpull and torque were experienced during coring, but in general hole stability was good. No drilling mud was used while coring below the 10¾-in casing shoe. The hole was eventually terminated in altered pillow basalt. The subsea TV camera was deployed on the vibration-isolated television (VIT) frame to inspect the reentry cone for sediment and cuttings. The cone was found clean, and thus no jetting was required on the way out of the hole. A short wiper trip back to bottom indicated that the hole had 2.0 m of fill. This was circulated out, and the drill bit was pulled clear of the reentry cone. Once secured, the ship was moved in DP mode back to Hole 1026B.

Return to Hole 1026B

While deploying the VIT frame at Hole 1026B, the subsea TV system failed, requiring 45 min to repair. The problem was traced to power-supply filters installed in surface equipment in the dynamic positioning control room. With the TV problem corrected, the reentry took place in short order (<15 min). The bit was run to bottom, tagging the cement at 2910.0 mbrf (240.9 mbsf). It took 5.5 hr to drill out the cement and shoe hardware, including the recovery of the center bit. Continuous RCB coring proceeded to a depth of 2964.3 mbrf (295.2 mbsf). Coring was plagued with major hole problems. High torque, overpull, and high pump pressure were common. Recovery was extremely poor in the highly fractured basalt. Recovery consisted primarily of rubble with few cored pieces. Several mud sweeps totaling 160 bbl were circulated while attempting to clean and stabilize the hole. The more the hole was fought, the more unstable it became. Concerns about permanently sticking the drill string eventually led to the termination of coring. The last tag with drill pipe, using no rotation or circulation, indicated a final hole TD of 2939.0 mbrf (269.9 mbsf), or 25.3 m shallower than the maximum depth achieved during coring. The drill string was recovered, and packer operations commenced. All pressure piping and manifolds were tested for leakage, and a wiper plug was pumped downhole to ensure that any loose rust would not infiltrate the packer setting go-devil.

After a pipe trip and reentry, the TAM International packer was run to the bottom of the 10¾-in casing string. Before setting the packer, the wireline was run to bottom with the DVTP to get a bottom-hole temperature and to check the hole TD. The depth check indicated that the hole had continued to deteriorate; the fill level was now up to 2929.0 mbrf, or only 4 m below the depth of the rathole. A temperature measurement at hole TD indicated that the formation around the hole seemed to be accepting fluid at a slow rate. The TAM packer was set once inside casing at 2878.1 mbrf. Two slug tests and two injection tests were conducted. Early results indicated that the formation was slightly underpressured. Upon completion of packer experiments, the drill string was pulled clear of the reentry cone. The pipe was secured, and the ship moved in DP mode back to Hole 1027C for additional packer work.

Return to Hole 1027C

After moving back to Hole 1027C (PP-4A) in DP mode, the hole was reentered, and the pipe was run to one stand above the 10¾-in casing shoe. At that point the wireline sinker bars were deployed with the DVTP tool. A depth check indicated that the hole depth had remained stable and that no further fill had entered. A bottom-hole temperature measurement was also taken at that time. The TAM packer was set twice. The first set was inside casing at 3228.0 mbrf. Three slug tests and two injection tests were conducted on the first set. The second packer set was in open hole at 3258.0 mbrf (590.7 mbsf). Two slug tests and three injection tests were conducted on the second packer set. Early results indicated that the formation might again be slightly underpressured. The testing went exceptionally well, and the data appeared to be of good quality. After completion of packer experiments, the drill string was recovered and preparations were begun in calm seas for the first Circulation Obviation Retrofit Kit (CORK) deployment of the leg. Deployment of the CORK, data logger, thermistor cable, and osmotic sampler systems went well with few problems. The CORK running tool was difficult to align with the CORK body because of their massive sizes. Once this was done and the mating surfaces were coated with pipe dope, the tool slid on easily. The thermistor string was lengthened by 15 m to take advantage of the extra hole depth. One grip used in the thermistor cable deployment slipped. Care was taken that the cable was dry and that the grips were made up sufficiently tight. While recovering the drill string, the positioning beacon was released/recovered and the ship began moving in DP mode back to Hole 1026B (PP-5A) for final CORKing operations at that site.

Return to Hole 1026B

Before the drill string was fully recovered, the DP move to Hole 1026B was completed. The CORK running tool was set aside, and preparations were begun to deploy a drill-in liner assembly made up of a modified mechanical bit release (MBR) and seven joints of junk 5-in drill pipe. The pin connection was cut off of the MBR bit disconnect. The box end of the top joint of 5-in drill pipe was then slipped on and welded. Stabilizer pads were welded onto the MBR body and turned to the drift diameter of the 10¾-in casing. This assembly was run in the hole, and the cone was reentered. The level of fill in the hole was tagged with the pin end of the drill-in liner at a depth of 2929.0 m (259.9 mbsf). This was 35.3 m above the original hole TD and only 12.8 m into basement (2916.2 mbrf). It was hoped that by drilling/washing in the drill string liner a conduit would be provided further into basement for the thermistor string. Because of the poor hole conditions, it was considered unlikely that anyone would ever wish to deepen the hole in the future. After multiple attempts, the liner was eventually worked down to a depth of 2955.0 mbrf (285.9 mbsf) by using very slow rotation (5 rpm) and very low circulation (20 spm). Drilling torque was 75–100 A. Heavy mud was spotted in the drill string to keep the flow moving in a downward direction during connections. We tried to get the liner in place with the least disturbance or vertical displacement of the fill up the annulus outside the liner. It was feared that, if highly fluidized, cuttings might flow back into the liner from the bottom or, if displaced high enough, would spill over the top of the liner. The rotary shifting tool and sinker bars were installed during the last connection, making the release operation relatively straightforward. Once the MBR was released, the annulus was circulated clean and the heavy mud was displaced out of the annulus with seawater. The shifting tool was recovered, and the sinker bars were run back to bottom to check the depth of open hole. On the first tag, 4.0 m of fill was found inside the drill pipe liner at a depth of 2951.0 m. After waiting an hour for cuttings to settle out further, the fill was again checked. This time the fill had reached a depth of 2949.0 mbrf, or 7 m up inside the liner. The final hole depth available for thermistor deployment was left at 31.8 m into basement. Nearly 20 m of open hole was regained by this effort. The top of the liner was placed at 2887.0 mbrf, or 30.6 m above the 10¾-in casing shoe. By the time the drill string was recovered, weather conditions were marginal for a CORK deployment, and the forecast indicated that weather and sea-state conditions would likely continue to deteriorate over the next 12–18 hr. As a result, the CORK deployment was deferred until later in the leg.

Hole 1026C

After the completion of CORKing operations at Sites 1024 and 1025, the ship was secured and headed to Site 1026 to complete the fourth and last CORK installation and to core the lower part of the sediment. During the 5-hr transit back, the ship was slowed to 6 kt for testing a new seismic streamer. Once the test was completed, the ship resumed full speed. Hole 1026C was located approximately 1000 m north from Hole 1026B (at 17°E) but was considered geologically to be part of the same sequence of Site 1026 (PP-5A) holes. A beacon was dropped, and an RCB BHA was made up and tripped to bottom. The RCB system was used because there was greater interest in recovering indurated sediment and basement samples than the softer overlying sediments. Because the upper 101.4 m of sediment had already been piston cored at Hole 1026A, the top 84.6 m was drilled with a center bit. Continuous RCB coring began at that point and continued to a depth of 248.2 mbsf. Recovery was poor until nearly 210 mbsf, where the sediments finally became indurated enough for the RCB system to be effective. The last three sediment cores achieved 90% recovery. Two subsequent basement cores in basalt rubble again failed to recover any “cored” material, only providing pieces of rubble “rollers” that tended to jam the core catchers. Some torquing was evident in basement but was not severe. One meter of fill was detected after making the connection before the last core. Once coring operations were terminated, the pipe was worked back to bottom and a 30-bbl sepiolite mud pill was circulated to try and clean the hole as much as possible. A wireline run was made to release the bit, and the hole was plugged with 29.7 bbl of 15.8-ppg class G cement spotted in basement. The cement was required to re-isolate basement hydrologically, to avoid possible perturbations at the nearest CORK installation at Site 1026B. The bit was then pulled clear of the mudline, and the beacon was recovered ending operations at Hole 1026C.

Return to Hole 1026B

The ship was offset 1000 m back to Hole 1026B and reentered within 0.25 hr after the rig floor was ready. The pipe was lowered to a depth of 2874.6 m, and after the top drive and a 20-ft knobby joint were picked up, the DVTP was run in on the wireline. A temperature profile of the borehole fluids was recovered as a bonus while running to bottom for a final thermistor-string depth check. Fill was tagged at a depth of 2947.0 m. This was considered to be essentially the same as before because it was within 1 m of the last measured depth (i.e., within the variations of a 2-m tide). The top drive was set back, and the driller began to trip the drill string back to the ship. Approximately halfway into the pipe trip, the evaluation of the temperature data from the last DVTP deployment was completed. The record indicated an influx of warm formation fluids into the hole. This was seen as an excellent opportunity to attempt recovery of pristine basement fluids. Unfortunately the water-sampling temperature probe (WSTP) tools would not fit through the bore of the CORK assembly; therefore the pipe trip was reversed, and the driller began to run back to bottom. After deploying the subsea TV camera, another quick reentry was made, and the pipe was run to a depth of 2720.8 m. The top drive was again picked up, and the WSTP was run in the hole with an Adara temperature measurement shoe made up to the bottom for redundancy. It was determined that the fluid path most likely was up the annulus between the makeshift drill pipe liner installed earlier in the leg and the 10¾-in casing. Thus the water sampler probe was positioned 8 m above the top of the liner. After allowing time for the sampler valve to open and close, a more detailed temperature profile was taken from the liner to the mudline. Measurements were taken with the tool held stationary for 3 min every 10 m to 20.9 mbsf. Then the measurements were taken every 2.0 m to 9.1 m above the mudline. When the tool was recovered the drillers stood by until the data quality could be determined. The tools were deployed a second time because the volume of fluid recovered was inadequate and the memories on both the Adara and WSTP tools ran out before the mudline was reached. The second deployment recovered a large volume of high-concentration formation fluid and complete temperature data. The exercise was exceptionally successful; all concerned agreed that the time was well spent and that the data and samples recovered were extremely valuable. By the time the drill string was recovered, weather conditions had begun to deteriorate, and the prognosis was for continued 25–30 kt winds over the next 12–24 hr. Because the seas had already begun to build, it was deemed inadvisable to begin CORK operations. Once again, deployment of the CORK was deferred at Hole 1026B. The ship was secured and then departed for Site 1028 (proposed site HT-5A).

Return to Hole 1026B

After the completion of Hole 1028A, the ship transited for a few hours back to Hole 1026B in calm seas. As on an earlier transit, speed was reduced to 6 kt for a brief period (2 hr) for a second test of the developmental seismic streamer. Once on site, the positioning beacon was commanded on, and preparations began quickly for deploying the CORK assembly. The entire CORK deployment operation, less the return pipe trip, was completed in only 14 hr. This included completing the trip to the seafloor (2669.1 mbrf) with the CORK assembly, handling the osmotic sampler, deploying 277.5 m of thermistor cable, completing the final attachment and electronic check of the data logger, deploying and latching the thermistor assembly (confirmed with 5000 lb of wireline overpull), landing and latching the CORK assembly (confirmed with 10,000 lb of drill pipe), recovering the CORK setting go-devil, deploying the CORK submersible/remotely operated vehicle (ROV) platform, deploying the VIT frame, releasing the CORK running tool, and recovering the VIT frame. The only negative result of the final CORK operation was that the lower portion of the CORK setting go-devil backed off during recovery and was lost on the seafloor. While storing the CORK tools and securing the rig floor for transit, the four lower guide horn cables (three were broken) were removed from the moon pool area so new cables could be fabricated before arrival in Victoria. The upper guide horn was installed, and the ship got under way to Site 1029, the first of several alternate sites to be cored with the remaining operational time.

LITHOSTRATIGRAPHY

Stratigraphic Units

The sedimentary succession along the Rough Basement Transect includes four lithostratigraphic units and subunits (Fig. 5). Subunit IA is Quaternary in age and composed of hemipelagic mud (clayey silt to silty clay), thin-bedded turbidites (silt to sandy silt), thin- to thick-bedded sand turbidites, and debris-flow deposits. The base of Subunit IA coincides with the deepest discrete sand bed. This boundary occurs at approximately 153 mbsf in Hole 1026C and 184 mbsf in Hole 1027B (Table 2). Hemipelagic mud deposits within Subunit IA are generally homogeneous, but there are local clay-rich color bands, silt laminae, zones of bioturbation, and increases in biogenic constituents, especially calcareous nannofossils. Turbidite characteristics include sharp to erosional bases, normal size-grading, plane-parallel laminae, and gradational tops. Some beds also display ripple cross-laminae, convolute laminae, or wavy laminae. Turbidite thickness usually increases as grain size coarsens. Beds of silt and sandy silt typically measure less than 10 cm, whereas sand beds reach maximum thicknesses of 1–7 m (Fig. 6). In some cases, these thicknesses probably have been distorted by the flow of unconsolidated sand within core liners. Coring disruption also destroyed internal sedimentary structures within the sand beds. Most of the relatively thin beds, however, contain well-defined base-missing Bouma sequences.

There are two types of inferred debris-flow deposits within Subunit IA (Fig. 5). The first is composed of very poorly sorted muddy sand in which high proportions of primary, fine-grained matrix undoubtedly assisted in the support of coarser sand grains during transport. Hybrid deposits of this type fall within the spectrum of sediment gravity flow mechanisms midway between the pure end-members of debris flow (total grain support by matrix strength plus buoyancy)

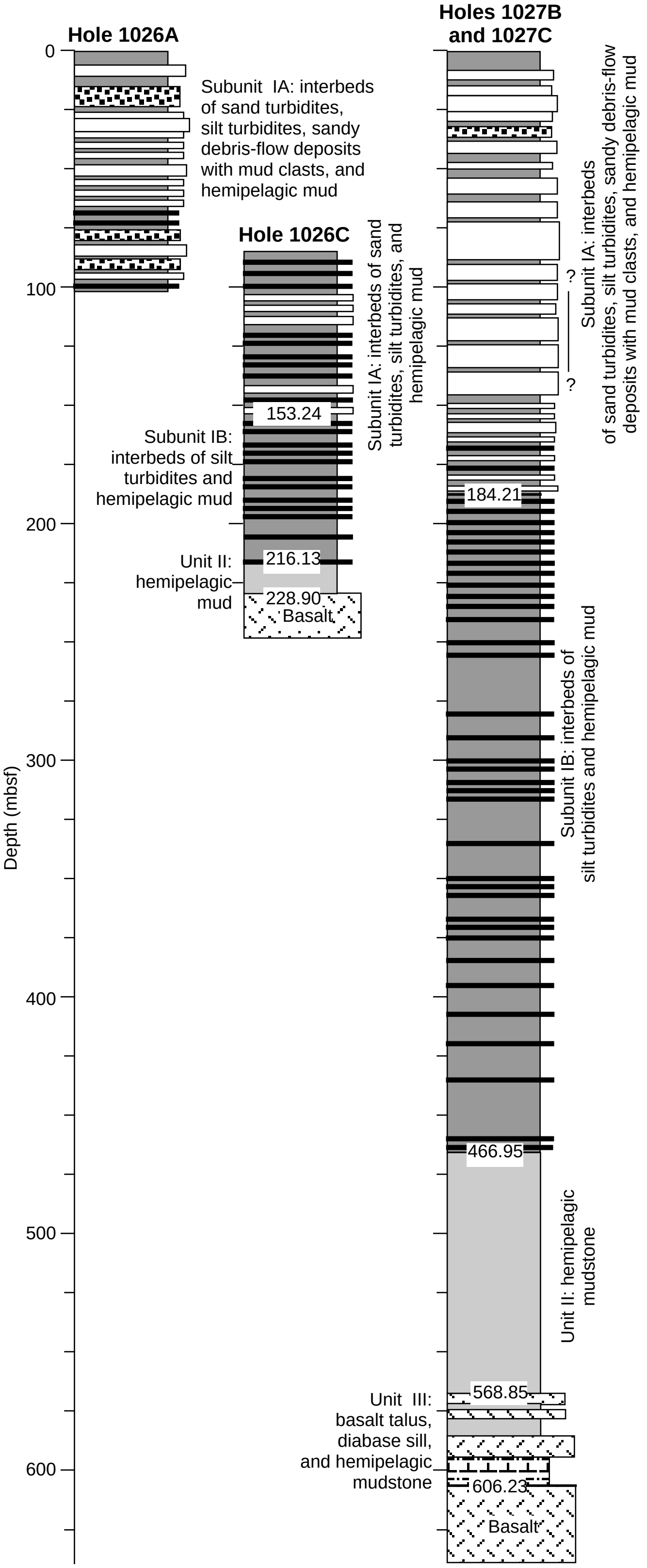

Figure 5. Stratigraphic summary for the Rough Basement Transect. Bed thicknesses are not shown to scale. White = sand turbidites; black = silt turbidites; and stippled = debris flow deposits.

Table 2. Summary of lithostratigraphic units within the Rough Basement Transect area.

Unit	Age	Lithologic character	Hole	Interval	Thickness (m)
IA	Quaternary	Sand turbidites, silt turbidites, hemipelagic mud, and debris-flow deposits	1026A 1026C 1027B	1H-1, 0 cm, to 12H-CC, 26 cm 1R-1, 0 cm, to 8R-CC, 14 cm 1H-1, 0 cm, to 21X-CC, 31 cm	Unknown 153.24 184.21
IB	Quaternary Quaternary to Pliocene	Silt turbidites, hemipelagic mud, and carbonate-rich mud	1026C 1027B	9R-1, 0 cm, to 14R-5, 43 cm 22X-1, 0 cm, to 50X-3, 95 cm	62.89 282.74
II	Quaternary Pliocene	Hemipelagic mud and carbonate-rich mud	1026C 1027B	14R-5, 43 cm, to 16R-1, 0 cm 50X-3, 95 cm, to 60X-CC, 29 cm	12.77 101.90
III	Pliocene	Basalt, basalt breccia, diabase sill, hemipelagic mudstone, carbonate-rich claystone, and hydrothermal alteration	1027B 1027C	60X-CC, 29 cm, to 62X-CC, 42 cm 1R-1, 0 cm, to 3R-2, 113 cm	Composite of 37.38

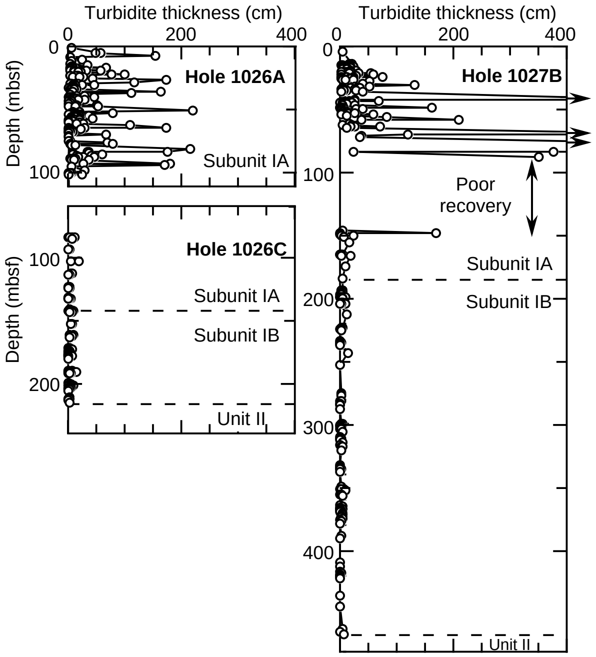

Figure 6. Depth distribution and thickness of sand turbidites, silt turbidites, and debris-flow deposits for holes of the Rough Basement Transect. Arrows signify thicknesses greater than 400 cm.

and turbidity current (total grain support by fluid turbulence). The second type of debris-flow deposit is made up of contorted mixtures of either muddy sand with mud chips or clayey silt with mud chips. Some such examples of fragmentation could be artifacts of coring, but APC-induced disruption usually produces down-bowing of stratigraphic layering, and the severity of disruption increases from core center to core edge. Upper and lower boundaries of the inferred debris-flow deposits, in contrast, are typically gradational in deformation style but geometrically concordant to nearby bedding planes. Clasts of cohesive mud, moreover, vary considerably in their degrees of induration, shape, and size; most appear to have been rounded by gravity-driven transport. Clast sizes range from a few millimeters to 5–10 cm, and the clasts are fully engulfed by very poorly sorted and internally structureless matrix material.

Despite their close proximity, the stratigraphic successions of Subunit IA differ significantly from Site 1026 to Site 1027 (Fig. 6). Gaps in core recovery prevent documentation of whatever large-scale cycles in turbidite thickness might exist at Site 1027. Both successions contain several small-scale upward-thickening cycles and intervals with clusters of thicker turbidites, but we were unable to recognize marker beds or make definitive intersite correlations among the turbidite clusters. Hole 1027B appears to contain more thick-bedded turbidites. Anemic recovery between 92 and 122 mbsf almost certainly was caused by failure of the core catcher to retain unconsolidated sand. This depth zone displays a chaotic to transparent echo character on seismic reflection profiles, but a comparable seismic interval does not exist at Site 1026. The total thickness of Subunit IA expands by approximately 30 m from Site 1026 to Site 1027. Conversely, the total number of gravity-flow deposits within the uppermost 85 m of each succession decreases from 192 at Site 1026 to 122 at Site 1027 (Table 3 on CD-ROM, back pocket). Evidently, intrabasinal depositional patterns responded to basement topography and evolving seafloor gradients in a complicated way (see “Site Geophysics” section, this chapter).

Subunit IB is Quaternary in age at Site 1026 and Quaternary to late Pliocene in age at Site 1027. These deposits are characterized by beds of silt and sandy silt intercalated with hemipelagic mud deposits (silty clay to clayey silt). Most of the silt beds are 1–5 cm in thickness, with sharp bases, plane-parallel laminae, normal size grading, and gradational tops. Many of the subtle details of these deposits were destroyed by fragmentation of the core into drilling biscuits and slurry. Intervals of slurry were difficult to discriminate from silty beds with lower degrees of induration. The hemipelagic mud deposits are superficially similar to those of Subunit IA, but they contain more highly variable admixtures of siliciclastic and biogenic constituents. Erratic increases in the content of calcareous nannofossils generally result in a subtle lightening of color. The base of Subunit IB coincides with the deepest discrete silt bed (Fig. 6), which occurs at depths of 216.13 mbsf (Hole 1026C) and 466.95 mbsf (Hole 1027B). Strata assigned to Subunit IB probably were deposited by thin, fine-grained, dilute turbidity currents interspersed with steady suspension fallout. Some remobilization of silt and mud by sluggish bottom currents also could have occurred.

Hemipelagic mud and mudstone deposits of Unit II are early Quaternary in age at Site 1026 and late Pliocene in age at Site 1027. Pyrite nodules become increasingly common with depth in this unit. Other characteristic features include silt and sandy-silt laminae, darker-colored clay-rich bands, intervals that were mottled by bioturbation, and *Zoophycos* trace fossils. The degree of induration increases gradually within Unit II, and an arbitrary designational change from mud to lithified mudstone occurs at a depth of approximately 425 mbsf. The thickness of Unit II ranges from 101.90 m in Hole 1027B to only 12.77 m in Hole 1026C.

The first occurrence of basalt rubble defines the depositional boundary between Unit II and Unit III at Site 1027 (Fig. 5; Table 2). When recoveries from Holes 1027B and 1027C are combined, Unit III includes fragments of basalt (probable talus deposits), homogeneous hemipelagic mudstone, interbeds of carbonate-rich claystone, a 7-m-thick interval of diabase (probable sill), and a variegated carbonate-rich claystone that locally approaches nannofossil chalk in its purity. Mottling by bioturbation is common. *Zoophycos* trails have been recrystallized to calcite, and there are several small faults with slickenlines that indicate normal senses of dip-slip offset. The carbonate-rich deposits display vivid color variations that probably were imparted on the rocks by hydrothermal alteration.

A lithostratigraphic equivalent unit of Unit III was not recovered from Hole 1026C. Instead, age control from nannofossils indicates that a significant disconformity exists at that sediment/basement contact (see "Biostratigraphy" section, this chapter). We define the contact with igneous basement as the deepest recovery of sedimentary rock; this boundary occurs at depths of approximately 228.9 and 606.2 mbsf in Holes 1026C and 1027C, respectively. The deepest strata from Hole 1026C (Core 168-1026C-15X) contain color bands and *Zoophycos* traces that are inclined at apparent dip angles of 15°–20°, and there are several offsets along small normal faults. These features indicate that early stages of sedimentation occurred on a steeply inclined seafloor.

Sedimentary Petrology

Carbonate Content

Figure 7 illustrates variations in calcium carbonate content for samples from Sites 1026 and 1027, as measured by coulometric analyses (see Table 18 on CD-ROM, back pocket). Subunit IA is characterized by low weight percentages of calcium carbonate; the average values are 3.0 and 2.8 wt% for Sites 1026 and 1027, respectively. One sample from Hole 1026C, located just above the base of Subunit IA, contains 18.8 wt% carbonate. Values from Subunit IB are distinctly more variable (Fig. 7). Samples from Hole 1026C contain an average of 6.4 wt% carbonate and a maximum of 56.6 wt%. In Hole 1027B, the mean value for Subunit IB is 4.5 wt%, and the maximum is 51.4 wt%. Most increases above 5 wt% are within lighter colored, nannofossil-rich mudstones. Lutites from Unit II also contain between 1 and 4 wt% calcium carbonate, in general, but there are two significant departures from this background level, with values of 27.6 and 64.4 wt% (Fig. 7). Nannofossil-rich mudstones and claystones from Unit III contain as much as 83 wt% calcium carbonate and average 21.9 wt%.

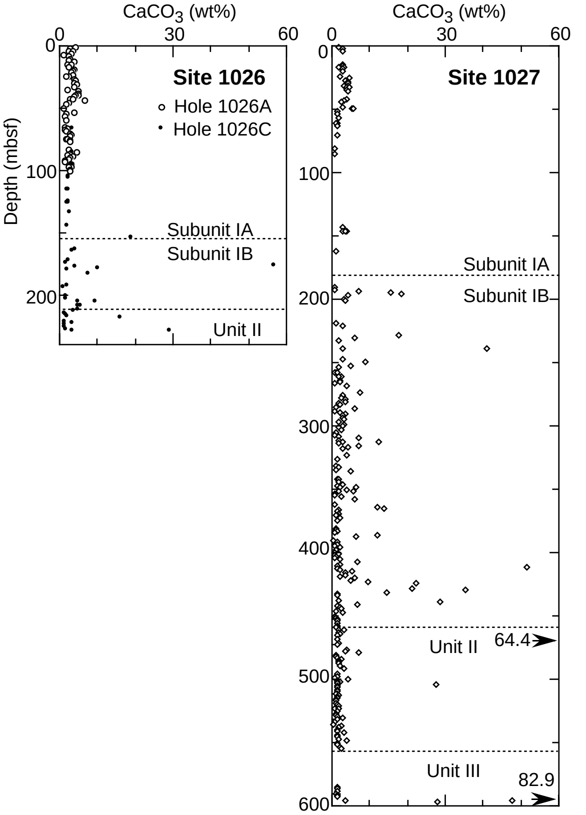

Figure 7. Contents of calcium carbonate (in weight percentage) for holes along the Rough Basement Transect, as measured by coulometric analyses.

Bulk Mineralogy

The bulk mineralogy of Subunit IA is similar to what was documented in Unit I at the Hydrothermal Transition sites (Tables 4, 5 on CD-ROM, back pocket). Most deposits contain abundant quartz, feldspar (plagioclase + K-feldspar), and phyllosilicates (muscovite + chlorite + illite + smectite), plus minor pyrite and amphibole. Trace minerals include pyroxenes, biotite, iron oxides, zircon, and opaque minerals (see smear-slide data on CD-ROM, back pocket). Detrital assemblages display pronounced scatter in the upper intervals of each hole because samples were taken from interbeds of sand, muddy sand, and hemipelagic mud. A negative correlation between total feldspar and total phyllosilicates is controlled largely by grain size (Fig. 8). Departures from this trend are associated with muddy sand deposits in Subunit IA and carbonate-rich muds. The relative abundance of total feldspar in thick sand layers in the upper 100 m of Subunit IA tends to be greater (as much as 68 wt%) than the feldspar content of sands from the Hydrothermal Transition sites (Fig. 9). The relative abundance of quartz also increases somewhat (to 35–45 wt%) in sand intervals.

Clayey silt to silty clay deposits have similar mineralogic compositions within both Subunit IA and IB (Fig. 9). Scatter in the contents of total feldspar and phyllosilicates probably is related to textural variations (i.e., silt-to-clay ratio), but there are no systematic changes in major mineral phases as a function of depth. Mudstones from Unit II, on the other hand, do show significant changes in mineralogy with depth. The relative abundance of phyllosilicates increases from 40 wt% near the top of Unit II to more than 50 wt% near its base, whereas the average feldspar content decreases from 30 to 15 wt% (Fig. 9). This relative increase of total phyllosilicates appears to be caused by enrichment of smectite; mica (illite + muscovite) and chlorite show little variation with depth (Fig. 10).

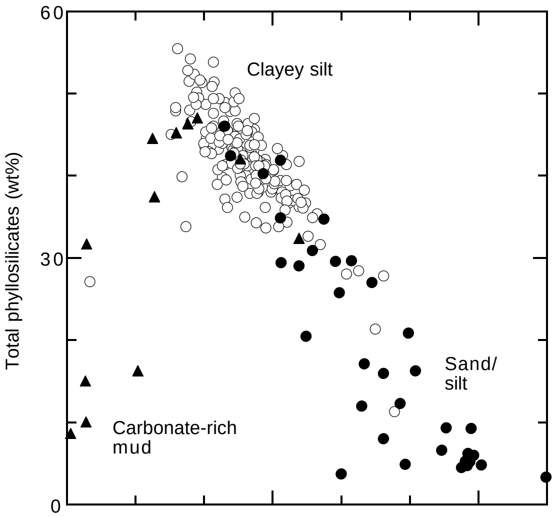

Figure 8. Relative weight percentage of total phyllosilicate minerals (smectite + chlorite + illite + muscovite) vs. total feldspar (plagioclase + K-feldspar), based on X-ray diffraction analyses of bulk powders. Note obvious size-dependent differences between hemipelagic mud and mudstone samples (open circles) and turbidite sand/silt samples (solid circles). Carbonate-rich samples (solid triangles) and debris-flow deposits show significant departures from this size-dependent mixing trend.

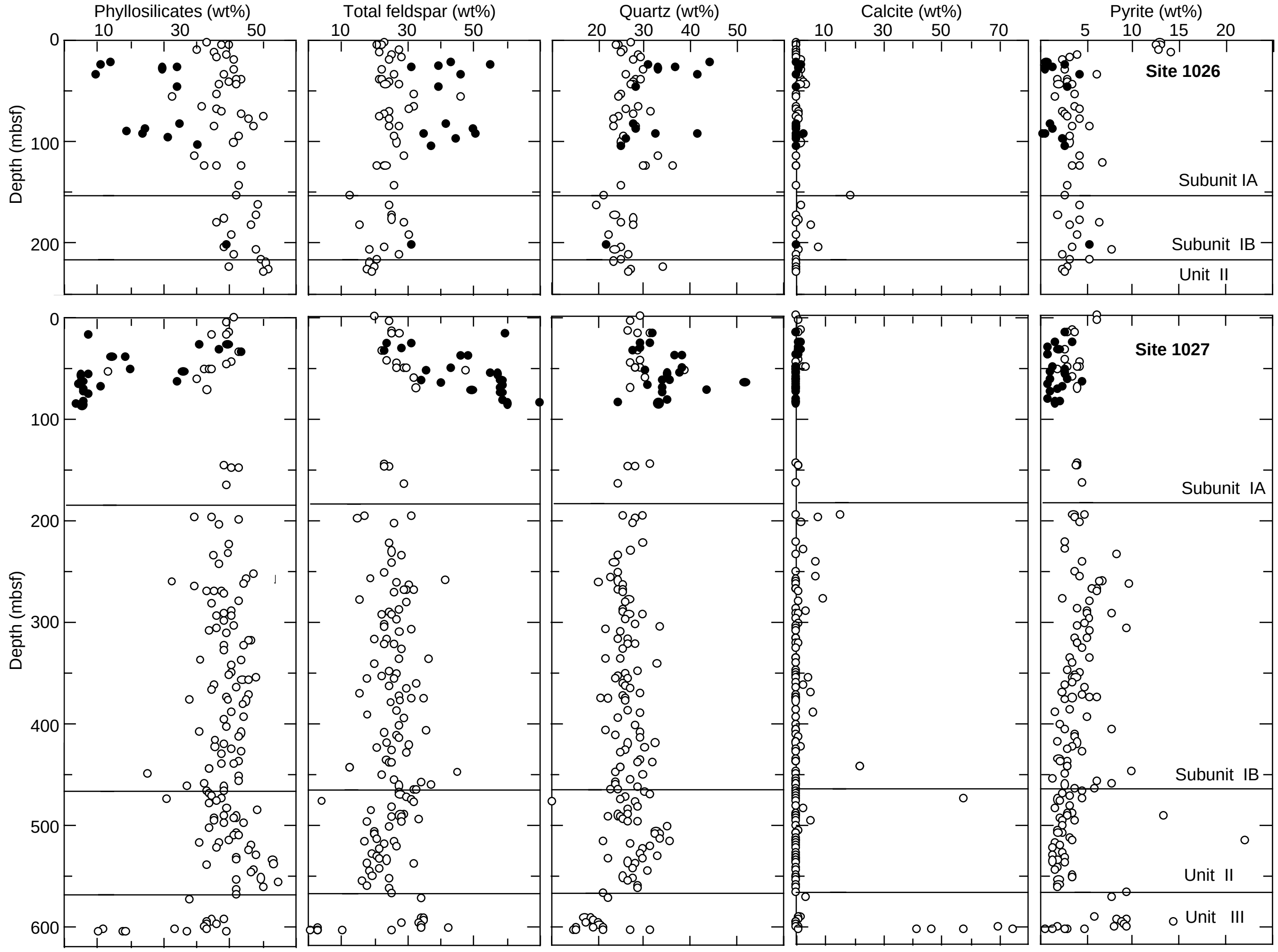

Figure 9. Depth distribution of major mineral phases (relative weight percentages) in Holes 1026B, 1026C, 1027B, and 1027C, based on X-ray diffraction analyses of bulk powders. Open circles = samples of hemipelagic mud and mudstone. Solid circles = samples of turbidite sand, silt, and debris-flow matrix.

Mineral assemblages of Unit III vary above and below the diabase sill at 584.8 mbsf. Assemblages above the diabase contain higher percentages of disseminated pyrite. Strata below the sill display distinctive color variations, from dark green to yellowish brown. Calcite and phyllosilicates are the major mineral phases of these variegated rocks, and smear slides indicate that the calcite is mostly biogenic (nannofossils). X-ray diffraction (XRD) analyses failed to identify the mineral(s) responsible for the color variations, which leads us to suspect the presence of amorphous Fe or Mn oxides.

Clay Mineralogy

Sixteen samples were selected from Holes 1027B and 1027C for more detailed analyses of clay minerals by X-ray diffraction analysis of the oriented <2-µm size fraction. Smectite, illite (mica), and chlorite occur in all 16 samples. Smectite produces a broad peak between 12.6 and 15 Å in air-dried specimens, and this peak shifts to 17.3 Å after glycolation (Fig. 11). On bulk-powder diffractograms, the (060) peak of smectite is located at about 1.50 Å, which is consistent with a dioctahedral variety of smectite. Chlorite produces peaks at about 14.2 Å (001) and at 7.12 Å (002). The (002) reflection is higher in intensity than the (001) reflection, which indicates that the chlorite is iron rich. The basal (001) reflection of illite occurs at about 10 Å, and its asymmetrical appearance indicates the presence of minor amounts of mixed-layer illite/smectite. The degree of peak asymmetry increases slightly with depth. For samples above 500 mbsf, the (002) chlorite peak is consistently the most intense. Below 500 mbsf, the smectite peak becomes the most intense (Fig. 11). This apparent increase in the relative abundance of smectite is consistent with results from bulk-powder analyses (Fig. 10). Smectite may have increased through neoformational replacement of feldspar, implying sediment/fluid reaction below 500 mbsf. Alternatively, the documented changes in clay mineralogy may have been caused by a shift in detrital provenance.

Sediment Alteration

Although subtle, several effects of diagenetic alteration are evident at the Rough Basement sites. There is evidence of recrystallization of calcareous nannofossils, for example, in sediments assigned to Subunit IB and Unit II. According to smear-slide and thin-section observations, calcite recrystallization first occurs at about 300 mbsf. Several important changes in pore-water chemistry occur at approximately the same depth (see “Fluid Geochemistry” section, this chapter), but the associated reactions have not produced detectable changes in the bulk-sediment mineralogy. Within Unit III, slickenlines along shear surfaces in Cores 168-1027C-2R and 3R may be sites of secondary calcite precipitation. Color variations in carbonate-rich

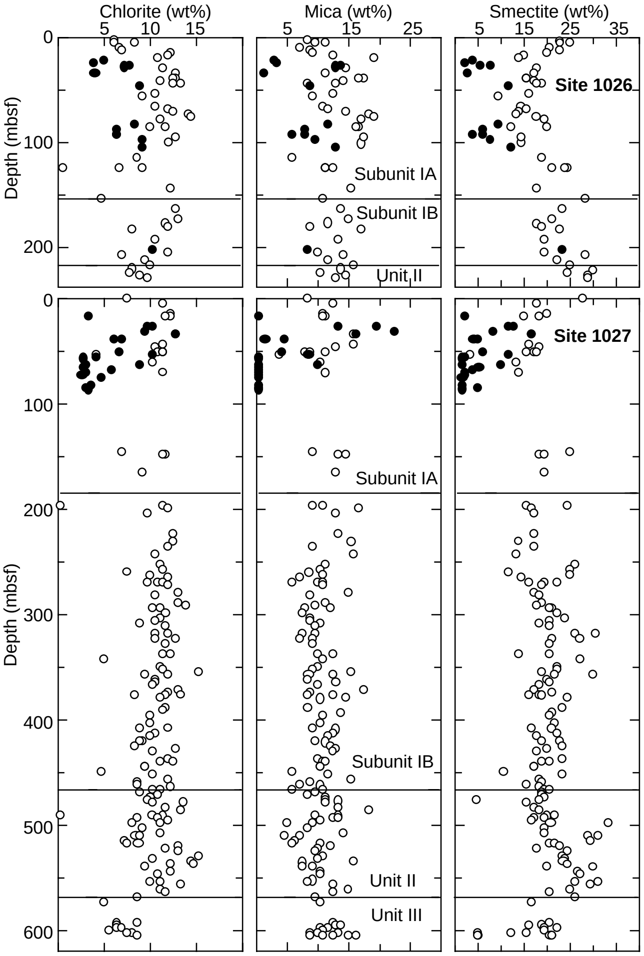

Figure 10. Depth distribution of relative clay mineral abundances (relative weight percentages) in Holes 1026B, 1026C, 1027B, and 1027C, based on X-ray diffraction analyses of randomly oriented bulk powders. Open circles = samples of hemipelagic mud. Solid circles = samples of turbidite sand and silty sand.

mudstones from Unit III also can be attributed to alteration. Pyrite nodules are common below 400 mbsf at Site 1027, and their increased abundance is also shown in the XRD results. A thin section of one nodule (Sample 168-1027B-46X-2, 30–31 cm) displays framboidal pyrite surrounding large (approximately 1–2 mm), zoned, euhedral plagioclase crystals; the plagioclase is probably volcanic in origin. The pyrite nodule is zoned, with euhedral crystals along the outer edges and larger framboidal aggregates toward the center; spaces within the pyrite concretion have been filled by fibrous quartz-chalcedony. Another pyrite nodule (Sample 168-1027B-56X-2, 101–102 cm) includes detrital grains of quartz and plagioclase and a homogeneous pyrite cement. The euhedral nature of the crystals indicates that the pyrite formed early in the compaction history of the sediment.

BASEMENT LITHOLOGY, PETROLOGY, GEOCHEMISTRY, AND ALTERATION

Lithologic Units

Basement was recovered from Holes 1026B, 1026C, 1027B, and 1027C and consisted of (1) aphyric to moderately phyric pillow basalt; (2) aphyric massive basalt; (3) basalt-hyaloclastite breccia; and (4) fine- to medium-grained diabase. At each hole, lithologic units were defined on the basis of changes in mineralogy, rock texture, and grain size (and are denoted by numbers 1–4; Fig. 12; Table 6). Unit 3 at Hole 1026B and Unit 4 at Hole 1027C was further divided into a series of subunits (denoted by unit numbers and lowercase letters [e.g., 3a, 4d, etc.]), based on the presence of chilled margins within the rock sequence. This allowed individual cooling units to be recognized and logged.

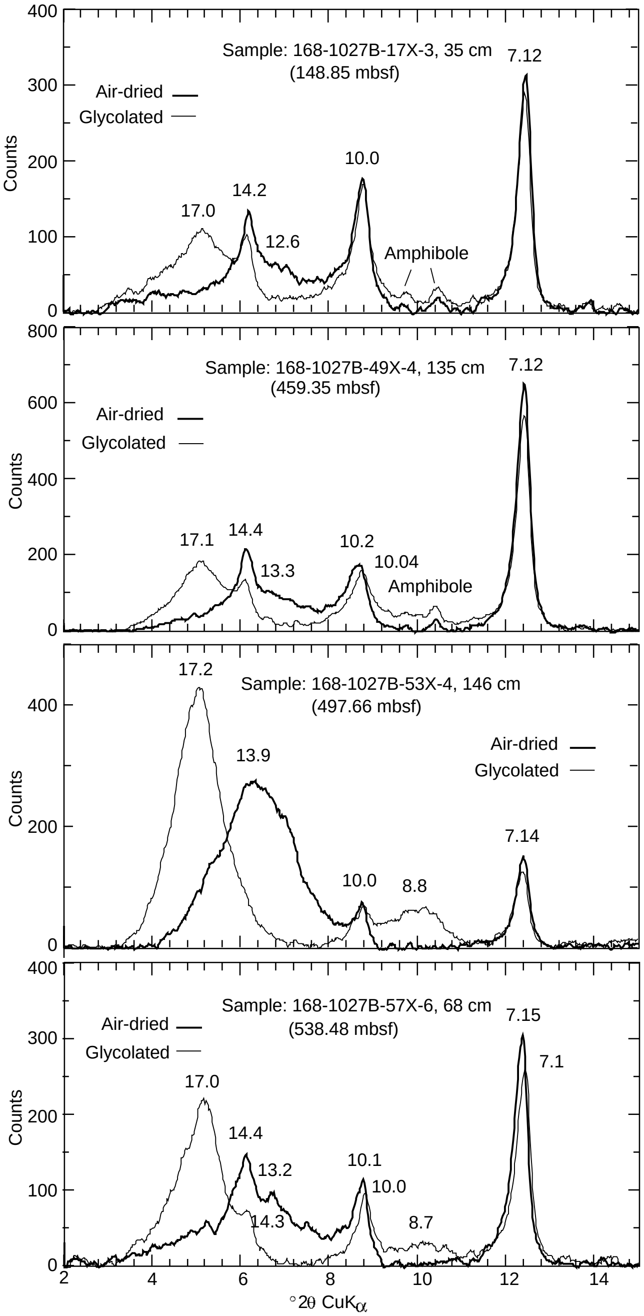

Figure 11. X-ray diffractograms of representative clay-sized separates (<2 µm size fraction), showing differences between air-dried and glycolated specimens. The numbers above each peak refer to d-spacing (measured in angstroms).

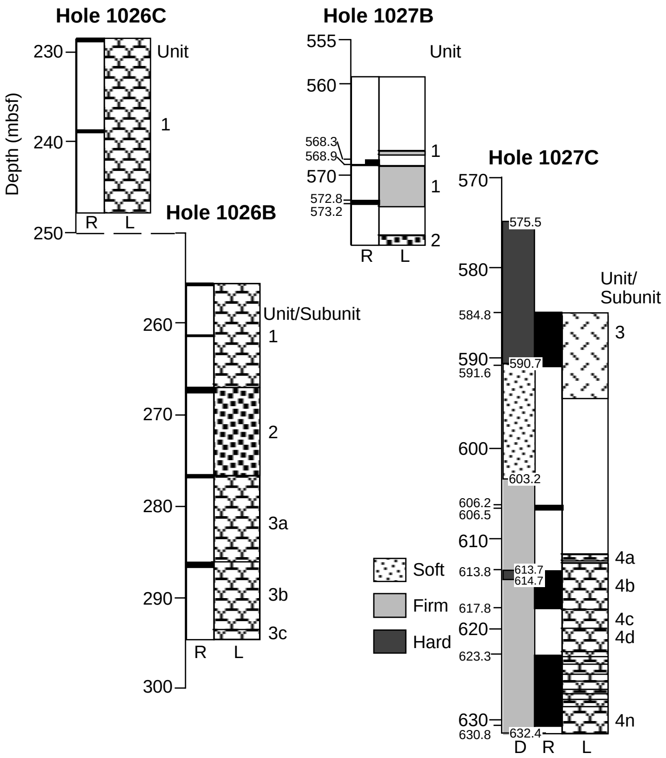

Figure 12. Lithostratigraphic logs for Holes 1026B, 1026C, 1027B, and 1027C. Column D = the drilling record for Hole 1027C; columns labeled R = actual recovery for all holes, indicated graphically by horizontal black bars; and columns labeled L = the lithologic record for all holes. Recovery (always <100%) has been expanded to fit the interval cored. The patterns used are the same as those in Figure 3 in the "Methods" chapter (this volume); no pattern has been assigned to the overlying or interbedded sediments.

Pillow Basalts

The most abundant rock type found within the Rough Basement sites was pillow basalt, which was recovered from Holes 1026B (Units 1 and 3), 1026C (Unit 1), and 1027C (Unit 4) (Fig. 12; Table 6). The pillow basalts are characterized by the presence of (1) a fine glassy, conchoidal rim on several fragments and (2) a dominantly hypohyaline to hypocrystalline texture within the fragments (Fig. 13). In general, the pillow basalts are aphyric to moderately phyric, containing minor amounts of plagioclase ± olivine ± pyroxene phenocrysts, set within a glassy to microcrystalline groundmass that contains microlites to microlaths of plagioclase ± olivine ± pyroxene ± opaques. The texture of the basalts varies within and between cores from glassy to subvariolitic (primarily sheaf-spherulitic ± plumose ± honeycomb textures) to glomeroporphyritic, seriate, and intersertal. All basalts are fresh to slightly altered and sparsely vesicular, containing round gas (≤2%) vesicles and a trace amount of round to irregular segregation vesicles.

Massive Basalts

Massive basalts were only found in samples from Holes 1027B and 1027C (Units 1 and 3) (Fig. 12; Table 6). They were classified as massive basalts because of the lack of well-developed chilled margins and their intersertal to intergranular and hypocrystalline to holocrystalline textures. Mineralogically, they are very similar to the pillow basalts, containing plagioclase + olivine ± pyroxene + opaque minerals, both as phenocryst phases and within the groundmass. In general, the massive basalts are slightly to moderately altered and sparsely to moderately vesicular, containing round gas (≤3.6%) and segregation (≤2.8%) vesicles.

Breccia

Section 168-1026B-3R-1 consists of a basalt-hyaloclastite breccia, containing angular clasts of aphyric basalt (with a variolitic to subvariolitic texture) and glassy shards, set within a consolidated clay matrix (Fig. 14A; Table 6). The majority of basaltic clasts vary from 6 to 60 mm in length, and they are variably cut by fractures and dark green-blue clay veins; smaller clasts (0.5–6 mm) are dominant in some parts of the breccia. The texture throughout the breccia varies from matrix supported (where large clasts are dominant) to clast supported (where the average clast size is <6 mm); the abundance of the clasts varies from 10% to 60% (average = 40%).

Although texturally similar to other aphyric basalt from Holes 1026 and 1027, the basaltic clasts within the breccia have been variably leached and altered to a pale brown-gray color and are preferentially altered along glassy variolitic margins to green-white clay. In all altered clasts (basalts and glassy shards), the extent of alteration decreases concentrically from the rims toward the center.

Basalt breccia also is present at the base of Section 168-1027B-62X-CC (Fig. 14B). This breccia consists of a variety of different angular to subrounded aphyric to moderately phyric olivine basaltic clasts that are set within a medium to dark gray muddy to carbonate-rich sedimentary matrix. The clasts (which are matrix supported) have been variably leached from light gray, to dark blue-gray, to brownish gray. In addition, some clasts exhibit well-developed oxidation halos that extend into the surrounding sedimentary matrix.

Diabase

A fine- to medium-grained, holocrystalline diabase was recovered from Hole 1027C between Sections 168-1027C-1R-1 and 1R-6 (Fig. 15; Table 6). This unit is characterized by a subophitic to ophitic texture, containing plagioclase (50%–54%), clinopyroxene (22%–33%), variably altered olivine (8%–15%), and minor opaques (≤5%). Although the top of the diabase was not recovered, the base is marked by an aphanitic chilled basaltic margin that consists of a holocrystalline, aphyric basalt with an intersertal texture. The diabase has been interpreted to be a sill.

Igneous Petrology

Five samples from Hole 1026B, two from Hole 1026C, five from Hole 1027B, and 20 from Hole 1027C were selected for petrographic analyses, covering the four lithologic units defined at the Rough Basement sites (i.e., aphyric basalts; sparsely to moderately phyric plagioclase ± olivine ± clinopyroxene basalts; basalt ± hyaloclastite breccia; and diabase). Table 6 summarizes the abundances and morphologies of the phenocryst and groundmass minerals present within each unit at the four holes; Table 7 lists the phenocryst and groundmass mineral modal abundances within each sample analyzed. Superimposed on the magmatic mineralogy are secondary phases produced by hydrothermal alteration; these will be discussed below in the "Basement Alteration" subsection.

Aphyric Pillow and Massive Basalt

The first igneous lithologic unit recovered from Holes 1026B, 1026C, and 1027B was aphyric basalt (i.e., Unit 1 at all three holes; Fig. 12). The presence of glassy rims on some of the fragments from Holes 1026B and 1026C indicates these are basaltic pillow fragments. In Hole 1027B, no chilled margins were found; therefore, the

Table 6. Summary of the rock types, lithologic units, and range of phenocrysts and groundmass minerals present at Holes 1026B, 1026C, 1027B, and 1027C, listing the diagnostic petrologic features of each unit.

Hole:	1026B	1026B	1026B	1026C	1027B	1027B	1027C	1027C
Rock type:	Aphyric basalt	Breccia	Aphyric to moderately phyric basalt	Aphyric basalt	Aphyric basalt	Basalt to hyaloclastite breccia	Diabase	Aphyric to moderately phyric basalt
Unit:	1	2	2a–c	1	1	2	3	4a–o
Hand specimen								
Structure:	Pillow basalts	Breccia	Pillow basalts	Pillow basalts	Massive basalt	Breccia	Sill	
Texture:	Variolitic to subvariolitic	Brecciated; poorly sorted	Variolitic to intersertal	Subvariolitic to glomeroporphyritic	Pilotaxitic to intersertal	Brecciated; poorly sorted	Subophitic to diabasic	Varitextured (variolitic to intergranular)
Grain size:	Cryptocrystalline to microcrystalline	Clay to pebbles	Cryptocrystalline to microcrystalline	Cryptocrystalline to microcrystalline	Cryptocrystalline to microcrystalline	Clay to pebbles	Fine to medium grained	Cryptocrystalline to microcrystalline
Crystallinity:	Hyaline to hypocrystalline	NA	Hypocrystalline	Hypohyaline to hypocrystalline	Hypocrystalline	NA	Holocrystalline	Hypocrystalline
Vesicles								
Gas (%):	≤2	NA	≤3.5	≤2	≤3.5	NA	≤2	≤2
Segregation (%):	Tr			Tr	≤3			≤1
Phenocrysts								
Plagioclase (%):	0 to tr	Tr	Tr	Tr	Tr to 1	Tr	—	Tr to 6
Morphology:	Euhedral	Euhedral	Euhedral	Euhedral	Subhedral to euhedral	Subhedral to euhedral	—	Euhedral to subhedral
Size range (mm):	≤1.5	≤0.2	≤2	≤1	≤2	≤1	—	0.3–3
Olivine (%):	—	Tr	Tr to 0.25	Tr	Tr	Tr to 3	—	0–4
Morphology:	—	Euhedral	Subhedral to euhedral	Euhedral	Euhedral to skeletal	Euhedral to skeletal	—	Euhedral to subhedral
Size range (mm):	—	≤0.2	≤1.5	≤1	≤1	≤1	—	0.2–3
Pyroxene (%):	0 to tr	—	Tr to 0.2	0 to tr	Tr to ≤2	Tr to 3	—	0–3
Morphology:	Euhedral	—	Euhedral to anhedral	Subhedral	Euhedral to skeletal	Euhedral to skeletal	—	Euhedral to subhedral
Size range (mm):	≤1	—	≤2	0.5–0.7	≤1	≤1	—	0.4–3
Groundmass								
Plagioclase (%):	≤9	—	≤4	11–15	30–32	≤15	50–54	4–42
Morphology:	Euhedral	—	Subhedral	Euhedral to subhedral	Subhedral to euhedral	Euhedral	Subhedral to euhedral	Euhedral to subhedral
Size range (mm):	≤0.4	—	≤0.3	0.1 to 0.6	0.1–0.8	≤0.2	≤2	0.1–0.5
Olivine (%):	0–3	—	0–1.5	0–1.8	0–7*	0.3–1.8	8–15	0–7
Morphology:	Euhedral to anhedral	—	Euhedral to subhedral	Euhedral to subhedral	Subhedral to anhedral	Subhedral to skeletal	Euhedral to anhedral	Euhedral to subhedral
Size range (mm):	≤0.2	—	≤0.5	0.1–0.3	≤0.1	≤0.1	≤0.6	≤0.3
Pyroxene (%):	≤3	—	≤3	≤6.5	—	0.3–1.8	22–38	Tr to 36
Morphology:	Subhedral to anhedral	—	Anhedral to skeletal	Euhedral to anhedral	—	Subhedral to skeletal	Subhedral to anhedral	Subhedral to anhedral
Size range (mm):	0.03–0.2	—	≤0.2	0.05–0.3	—	≤0.1	≤3	0.01–0.3
Opaque minerals (%):	Tr	—	≤0.6	Tr	Tr	Tr	3–4	Tr to 5
Morphology:	Subhedral to granular	—	Anhedral to skeletal	Granular to skeletal	Subhedral to granular	Granular	Granular to elongate	Euhedral to skeletal
Size range (mm):	≤0.01	—	0.05–0.2	≤0.02	≤0.04	≤0.01	0.1–0.3	0.005–0.1
Spinel (%):	—	—	—	—	Tr	Tr	—	Tr
Morphology:	—	—	—	—	Euhedral	Euhedral to subhedral	—	Euhedral to rounded
Size range (mm):	—	—	—	—	0.005–0.01	≤0.01	—	0.06–0.2
Mesostasis (%):	≤83	—	≤88	61–77	54–63	69–75	—	17–87
Texture:	Variolitic to sheaf-spherulitic	—	Sheaf-spherulitic	Sheaf-spherulitic	Sheaf-spherulitic to intersertal	Subvariolitic	—	Sheaf-spherulitic

Notes: NA = not applicable, — = not observed, and Tr = trace amount. * = the abundance, morphology, and grain size have been combined for olivine and pyroxene, as these phases could not be distinguished optically because of alteration effects.

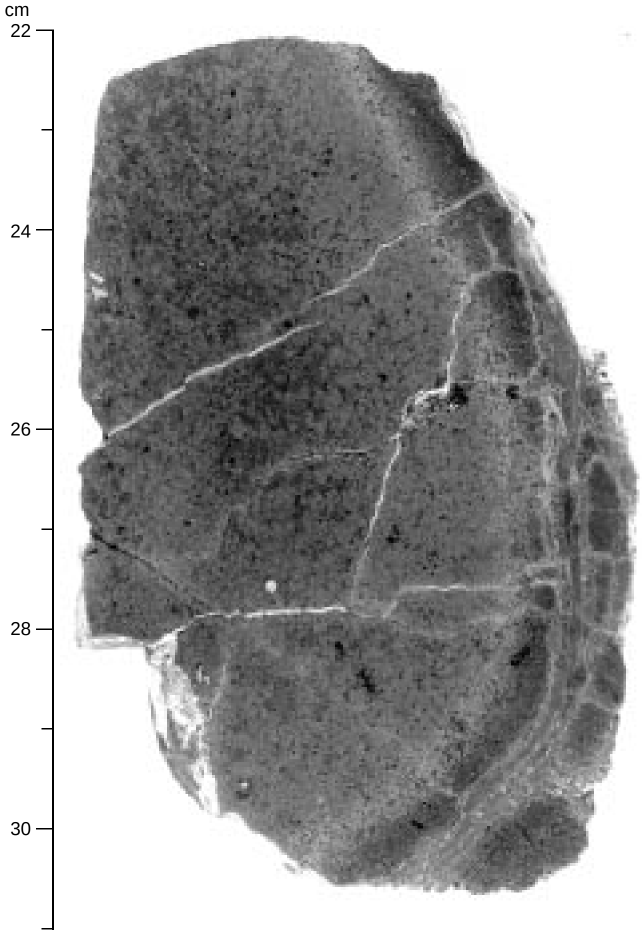

Figure 13. Close-up photograph of a pillow fragment (Sample 168-1027C-4R-3 [Piece 4, 22–31 cm]) exhibiting a well-developed glassy margin, grading into variolitic and subvariolitic zones.

unit was described as massive basalt. The aphyric basalts from all three holes have the same grain size range (aphanitic), are sparsely to moderately vesicular, and are mineralogically similar in terms of the types and morphology of magmatic phases present. However, differences occur in the relative abundance of these phases within the groundmass, as well as in the whole-rock texture.

A trace amount of phenocrysts is present in the aphyric basalts from all three holes (Table 6). In samples from Hole 1026B (Fig. 16A), plagioclase is commonly the only phenocrystic phase, present as 0.3- to 0.7-mm euhedral laths and stubby crystals. They occur as solitary grains or within monomineralic glomeroporphyritic clots and exhibit simple to oscillatory zoning. Within the aphyric basalts from Hole 1026C, ≈1% plagioclase (0.4–1.5 mm; euhedral–subhedral laths) and a trace amount of pyroxene phenocrysts (0.5–0.8 mm; euhedral–subhedral) are present (Fig. 16B). The plagioclase occurs in monomineralic, bimineralic, and polymineralic glomeroporphyritic clots and exhibits simple to oscillatory zoning; the pyroxene phenocrysts occur in a subophitic to ophitic arrangement within the glomeroporphyritic clots.

In samples from Hole 1027B, plagioclase, olivine, and/or pyroxene are present as phenocryst phases (Fig. 16C). Here, the plagioclase forms euhedral to subhedral 0.5- to 1.6-mm laths, which exhibit a faint parallel orientation throughout all of the sections analyzed from this hole. Some plagioclase phenocrysts exhibit an irregular outline; this may be caused by (1) skeletal growth around the euhedral crystal; (2) minor secondary alteration of some crystals; and/or (3) partial resorption by the surrounding groundmass. The olivine and/or pyroxene present within the aphyric basalts from Hole 1027B form 0.5- to 0.8-mm euhedral to subhedral crystals, which have been completely replaced by secondary granular to fibrous saponite and calcite. Because of the completeness of the alteration, it was generally impossible to determine the precise mineralogy of the original phase.

In general, the groundmass mineralogy of the aphyric basalts from all three holes is dominated by cryptocrystalline mesostasis (51%–83%), which has been variably altered (from 0% to ≤17%) to secondary saponite, celadonite, iddingsite, and carbonate (Fig. 16A–C). Although the same mineral phases can be recognized within the groundmass in rocks from all holes, the relative abundance and grain size range of each phase differs (Tables 6, 7). Plagioclase from Hole 1026B occurs as ≤0.4-mm euhedral laths, with a characteristic abundance of <9%. This increases to <15% in samples from Hole 1026C, where the plagioclase forms 0.1- to 0.6-mm euhedral–subhedral laths, whereas the groundmass from Hole 1027B contains 30%–32% euhedral–subhedral plagioclase laths (≤0.8–0.1 mm). In all cases, plagioclase occurs as microlaths, microlites, and quench crystals (exhibiting hollow and swallowtail forms), indicative of rapid growth and/or nucleation, and is present as solitary grains as well as within microglomeroporphyritic clots.

The primary difference in the mafic groundmass phases among the three holes is that all of the subhedral to anhedral olivine and pyroxene from Hole 1027B has been replaced by secondary saponite and calcite (≤0.1 mm; original abundance: 5%–7%), whereas in samples from Holes 1026B and 1026C, only the olivine (≤0.3-mm euhedral to anhedral grains; 1.5%–3% original abundance) has been replaced. Anhedral crystals of pyroxene (≤0.06 mm; ≤6%) occur throughout the groundmass from Holes 1026B and 1026C, with larger subhedral crystals (≤0.2 mm) present singly and within microglomeroporphyritic clots.

Trace amounts of opaque sulfides (subhedral to granular pyrite and pyrrhotite; ≤0.04 mm) are disseminated throughout the groundmass within all aphyric basalts. Larger, discrete grains (≤0.1 mm) of pyrite and pyrrhotite are only discernible within unoxidized samples from Hole 1026B, whereas trace amounts of euhedral to subhedral magnetite (≤0.05 mm) are present within the aphyric basalts from Holes 1026C and 1027B.

All of the aphyric basalts are vesicular, containing round to irregular gas vesicles as well as round segregation vesicles. Vesicularity within the pillow basalts from Hole 1026B is low (≤0.5% combined total), consisting of 0.05- to 0.1-mm gas vesicles and ≤0.2-mm segregation vesicles; the gas vesicles have subsequently been infilled by secondary clays. Vesicularity increases in aphyric basalts from Hole 1026C to ≤1.6%, represented by 0.05- to 0.4-mm round gas vesicles (lined or completely filled by fibrous to granular secondary clays) and a trace amount of round segregation vesicles (0.1–0.15 mm in diameter and filled with mesostasis and opaque rods). The aphyric massive basalts from Hole 1027B are sparsely to moderately vesicular (0.5%–6.5%) and contain larger individual gas (≤0.5 mm) and segregation (≤1.3–0.8 mm) vesicles.

Finally, clear textural variations occur between the aphyric basalts from Holes 1026B, 1026C, and 1027B. The aphyric basalt from Holes 1026B and 1026C is varitextured, consisting of glassy to variolitic and subvariolitic zones that extend away from the chilled margins (Fig. 16B). The subvariolitic zones generally exhibit a sheaf-spherulitic to faint plumose texture and contain microglomeroporphyritic clots of plagioclase and pyroxene ± olivine. The basalts from Hole 1027B are dominated by an intersertal texture that is weakly to moderately pilotaxitic (Fig. 16C). Between the plagioclase microcrysts, the interstitial mesostasis exhibits a variety of subvariolitic textures, including (1) sheaf-spherulitic, (2) plumose, (3) honeycomb, and (4) branching structures. The textural variations that can be observed between the aphyric basalts from Holes 1026B, 1026C, and 1027B can be directly related to the structure and crystallinity of the basalts; aphyric pillow basalts from Hole 1026B and 1026C are

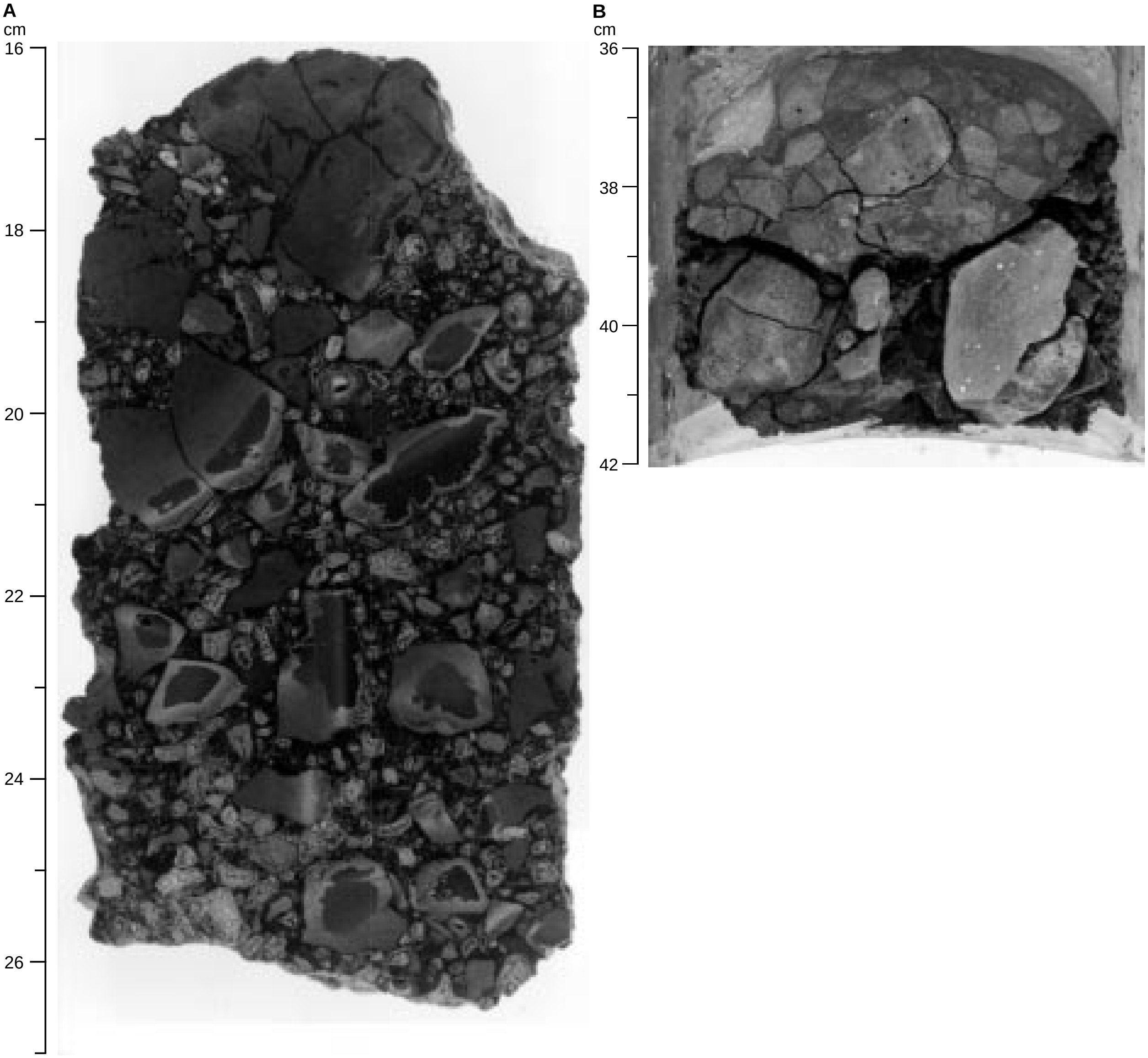

Figure 14. **A.** Close-up photograph of the basalt-hyaloclastite breccia (Sample 168-1026B-3R-1, [Piece 3, 16–27 cm]) exhibiting variably altered basalt and glassy clasts supported within a saponitic clay matrix. **B.** Close-up photograph of basalt breccia from Sample 168-1027B-62X-CC, 36–42 cm, consisting of angular to subrounded basalt clasts, which are matrix supported within a carbonate-rich sediment.

less crystalline (and hence more subvariolitic) than the massive aphyric basalts from Hole 1027B (which are characteristically intersertal).

Sparsely to Moderately Phyric Basalts

Unit 3 from Hole 1026B and Unit 4 from Hole 1027C are made up of aphanitic sparsely to moderately phyric plagioclase ± olivine ± pyroxene basalts (Fig. 12). Each unit has been divided into a number of subunits (e.g., Unit 3a–c and Unit 4a–o), based on the presence of chilled margins (Table 6), and it is suggested that each subunit represents an individual cooling unit, the thickness of which varies from 20 cm to more than 2 m. (Because recovery was less than 100%, these figures represent minimum estimates for unit thickness.) Texturally, the sparsely to moderately phyric basalts from Holes 1026B and 1027C are dominated by intersertal to intergranular characteristics, with patches of subvariolitic mesostasis (Fig. 17A–C). Subvariolitic zones are dominated by a sheaf-spherulitic texture, with minor occurrences of plumose and honeycomb textures. In addition, some rocks also contain areas with glassy to variolitic and glomeroporphyritic textures.

All sparsely to moderately phyric basalts are sparsely to moderately vesicular (≤2.5%; average = 0.5%), containing 0.05- to 0.8-mm (average = 0.3 mm) round gas vesicles. The majority of gas vesicles in samples from Holes 1026B and 1027C have been lined or filled by secondary saponite ± celadonite ± iddingsite/FeO(OH) ± hematite ± pyrite ± carbonate. Segregation vesicles (0.2–0.6 mm; average = 0.4 mm) are also present in trace amounts within the aphyric to moderately phyric basalts from Hole 1027C and are externally lined by tangential plagioclase microlites. All segregation vesicles are completely to partially filled by mesostasis material. Those that are only partially filled by mesostasis have subsequently been lined or filled by secondary saponite, celadonite, and/or hematite.

Varying amounts of plagioclase, olivine, and pyroxene phenocrysts are present within all of the basalts from Units 3 (Hole 1026B) and 4 (Hole 1027C), with the most common modal abundance rock

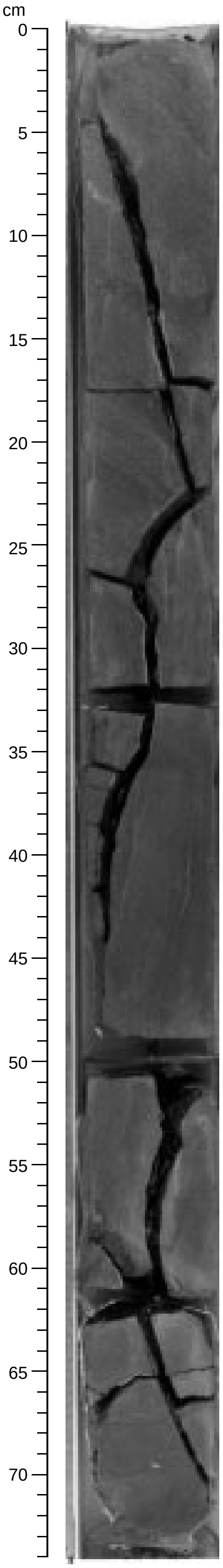

Figure 15. Close-up photograph of the diabasic sill grading down to the aphanitic chilled basaltic margin at the base (interval 168-1027C-1R-6, 0–74 cm). The core is cut by an anastomosing fracture lined by secondary carbonate and clay.

types being moderately phyric plagioclase-olivine-pyroxene basalt and sparsely phyric plagioclase-olivine basalt (Fig. 17A–C). A change in phenocryst type and abundance was detected within and among the subunits; Sections 168-1027C-3R-2 through 4R-2 (Subunits 4a–c) contain plagioclase (1.2%–5.8%), olivine (1.0%–3.6% original abundance), and pyroxene (1.6%–3.0%) phenocrysts, whereas Sections 168-1027C-4R-2 through 5R-5 (Units 4c–o) contain plagioclase (1.0%–3.0%), olivine (1.0%–2.4% original abundance), and a trace amount of pyroxene phenocrysts; this petrologic distinction is mirrored in the geochemical results.

Phenocrysts of plagioclase (0.3–3 mm; average = 0.8 mm) form euhedral to subhedral elongate and stubby laths, with an average abundance of 3% (total range = 1%–6%). In addition to the euhedral laths, some skeletal and quench crystals are also present within several subunits. The plagioclase phenocrysts occur singly, in monomineralic and polymineralic glomeroporphyritic clots (plagioclase ± pyroxene ± olivine), as well as within well-developed bow-tie structures, associated with pyroxene. Simple to oscillatory zoning is common, as are sparse to dense abundances of glass inclusions within the cores of some plagioclase phenocrysts.

Virtually all olivine phenocrysts (0.1–2.8 mm; average = 0.6 mm) have been completely to partially replaced by a variety of secondary hydrothermal alteration phases. In samples from Hole 1026B and Sections 168-1027C-3R-2, 4R-1, 4R-2, and 4R-3, the olivine is replaced by celadonite ± iddingsite ± saponite, whereas in Sections 168-1027C-5R-1 through 5R-5, the olivine is replaced by saponite ± talc ± carbonate ± iddingsite/FeO(OH) ± zeolites. All pseudomorphs have retained the original euhedral to subhedral shape of the olivine crystals, whereas any remaining fresh olivine is characterized by a relict morphology. Point counts indicate that between 1% and 4%, olivine was originally present within the rocks; present abundances vary from 0% to 1%.

Pyroxene (≤2.4 mm; average = 0.5 mm) is generally the least abundant of the phenocryst phases, with an abundance of ≤3% (average = 1.5%). The majority of crystals have a subhedral morphology and occur singly, intergrown with plagioclase, or within polymineralic glomeroporphyritic clots with plagioclase and olivine.

The groundmass mineralogy, which consists of the same minerals as the phenocrysts, is associated with primary magmatic spinel, opaques oxides, opaque sulfides, and mesostasis material. Plagioclase microlaths, microlites, and microquench crystals (0.1–0.5 mm; average = 0.2 mm) are the most common groundmass crystalline phase, equivalent to 4%–42% (average = 18%) of the total rock abundance. They occur as solitary crystals and stellate clusters within the mesostasis, loosely combining to form a pilotaxitic to intersertal texture; all other phases occur interstitially (Fig. 17A–C).

Groundmass olivine (original abundance 0%–7%) has been subjected to the same degree of alteration as the olivine phenocrysts, replaced by a variety of secondary hydrothermal phases (e.g., saponite ± iddingsite/FeO(OH) ± talc ± carbonate ± celadonite). The partially to completely altered olivine crystals (≤0.5 mm) are characterized by a granular to microcrystalline to feathery morphology and occur as solitary grains throughout the groundmass, as well as at the center of polymineralic glomeroporphyritic clots. Subhedral to anhedral pyroxene microcrysts (0.01–0.3 mm; average = 0.1 mm) also occur within the centers and rims of these clots. In addition, discrete crystals, along with microcrystalline to cryptocrystalline feathery sheaves of pyroxene, occur through the mesostasis, present as a trace amount to as much as 9%. In Sections 168-1027C-4R-1 and 4R-2, microcrystalline pyroxene grains constitute between 24% and 36% of the groundmass.

Euhedral to skeletal granules of opaque oxides (0.005–0.1 mm; average = 0.025 mm) and opaque sulfides (0.005–0.05 mm; average = 0.02 mm) are present within most sparsely to moderately phyric basalts, disseminated throughout the mesostasis, and as inclusions within some phenocrysts. The opaque oxides (optically isotropic and identified as magnetite and/or maghemite, based on paleomagnetic

Table 7. Modal mineral abundances for all thin-section analyses conducted on samples from Holes 1026B, 1026C, 1027B, and 1027C.

		Phenocrysts			Groundmass				Vesicles		Secondary
Sample	Structure	Olivine[a] (%)	Clinopyroxene (%)	Plagioclase (%)	Olivine[a] (%)	Clinopyroxene (%)	Plagioclase (%)	Mesostasis[b] (%)	Gas (%)	Segregation (%)	alteration (%)
1026B-1R-1 (Piece 7, 29–33 cm)	Pillow basalt	—	—	0.4	2.4	3.2	8.8	83.4	Tr	Tr	9.6
1026B-4R-1 ((Piece 7, 36–44 cm)	Pillow basalt	—	—	0.6	4.0	—	12.4	13.0	1.6	—	16.2
1026B-5R-1 (Piece 1, 46–49 cm)	Pillow basalt	0.4	0.2	3.0	1.5	3.0	4.0	86.5	2.4	—	2.7
1026C-16R-1 (Piece 10, 40–45 cm)	Pillow basalt	—	0.2	1.4	1.8	6.4	11.6	77.0	1.6	Tr	9.3
1026C-17R-1 (Piece 8, 31–38 cm)	Pillow basalt	—	0.2	0.8	1.6	6.0	14.6	75.2	1.6	—	17.4
1027B-60X-CC (Piece 5, 33–36 cm)	Massive basalt	2.6*	—	Tr	—	—	30.4	63.0	1.4	1.6	12.2
1027B-61X-CC, 13–15 cm	Massive basalt	3.0*	—	Tr	7.0*	—	30.4	54.0	3.6	2.8	12.4
1027B-61X-CC, 25–28 cm	Massive basalt	5.0*	—	Tr	—	—	32.6	59.2	0.8	0.8	9.0
1027B-62X-CC, 7–10 cm	Massive basalt	1.2*	—	Tr	4.8*	—	30.4	57.8	3.4	—	9.4
1027B-62X-CC, 39–42 cm	Basalt breccia	3.0*	—	Tr	3.5*	—	14.8	75.2	1.4	—	6.4
1027C-1R-1 (Piece 1, 10–16 cm)	Diabase	—	—	—	14.6	21.8	50.4	—	0.2	—	22.0
1027C-1R-1 (Piece 1B, 39–42 cm)	Diabase	—	—	—	8.8	32.8	54.2	—	—	—	20.0
1027C-1R-2 (Piece 1A, 35–42 cm)	Diabase	—	—	—	8.4	25.6	53.2	—	Tr	—	10.6
1027C-1R-4 (Piece 1C, 65–68 cm)	Diabase	—	—	—	9.2	27.4	51.8	—	0.4	—	11.6
1027C-1R-6 (Piece 2, 67–70 cm)	Diabase	1.2	—	1.2	4.6	—	46.2	38.8	1.8	Tr	8.6
1027C-3R-2 (Piece 5, 125–126 cm)	Pillow basalt	3.6	1.6	5.8	7.4	—	14.0	65.1	1.0	0.2	4.6
1027C-4R-1 (Piece 11, 63–67 cm)	Pillow basalt	2.8	1.4	5.8	—	8.6	14.8	63.8	0.6	0.6	12.0
1027C-4R-1 (Piece 17, 110–113 cm)	Pillow basalt	1.0	1.0	1.6	3.0	24.0	42.0	21.0	1.6	—	12.8
1027C-4R-1 (Piece 20, 131–136 cm)	Pillow basalt	2.2	3.0	5.0	2.8	28.2	30.0	24.8	0.2	Tr	5.0
1027C-4R-2 (Piece 2, 9–15 cm)	Pillow basalt	2.2	1.6	4.2	0.8	36.2	31.8	17.2	0.6	Tr	5.6
1027C-4R-2 (Piece 9C, 85–89 cm)	Pillow basalt	1.0	—	1.4	1.8	—	6.8	82.0	Tr	Tr	9.8
1027C-4R-3 (Piece 2, 9–14 cm)	Pillow basalt	1.8	Tr	1.4	2.0	0.4	11.4	77.6	0.5	Tr	11.0
1027C-5R-1 (Piece 2, 6–10 cm)	Pillow basalt	2.4	—	3.0	0.4	2.2	3.8	87.4	0.8	—	2.8
1027C-5R-1 (Piece 8, 92–96 cm)	Pillow basalt	1.2	—	3.0	2.8	6.4	16.2	68.6	0.8	—	23.4
1027C-5R-2 (Piece 1A, 1–9 cm)	Pillow basalt	1.0	—	2.0	2.6	—	7.8	71.5	Tr	—	6.7
1027C-5R-2 (Piece 2, 49–51 cm)	Pillow basalt	1.0	0.4	3.2	1.0	2.3	15.2	74.4	0.8	—	9.0
1027C-5R-3 (Piece 8, 105–109 cm)	Pillow basalt	—	—	3.6	3.0	Tr	15.4	77.5	0.2	—	3.6
1027C-5R-4 (Piece 5, 68–70 cm)	Pillow basalt	1.6	—	1.0	2.4	2.8	22.8	69.0	0.4	Tr	11.4
1027C-5R-5 (Piece 3, 32–43 cm)	Pillow basalt	1.0	—	2.2	1.0	31.5	42.2	21.0	Tr	Tr	5.8
1027C-5R-5 (Piece 11, 121–123 cm)	Pillow basalt	1.0	—	1.2	0.8	1.0	18.0	78.0	Tr	Tr	4.2

Notes: — = not observed, and tr = trace amount. * = abundances represent the combined total for completely altered olivine and/or pyroxene.

[a] Olivine abundances represent the original abundance before alteration.

[b] Mesostasis abundances include any glass present in the thin section.

results) form microcrystalline to cryptocrystalline needles, cubes, and granular bundles and have a trace to 5% abundance within rocks from both holes. The type of primary magmatic opaque sulfide, however, differs between Hole 1026B and Hole 1027C. The sparsely to moderately phyric basalts from Hole 1026B contain ≤0.2% granular pyrrhotite grains (≤0.05 mm), distributed throughout the mesostasis, whereas within the mesostasis from Hole 1027C, anhedral to globular pyrite (≤0.1 mm) is the only primary magmatic sulfide phase present in trace amounts. These perfectly spherical pyrite globules may represent immiscible droplets that were present in the magma.

The mesostasis represents between 17% and 87% of the total rock volume of all sparsely to moderately phyric basalts from Holes 1026B and 1027C (Fig. 17A–C). It consists of a cryptocrystalline, brown to brown-gray mass that is characterized by a dominantly sheaf-spherulitic texture; minor patches with plumose and honeycomb textures can also be recognized. Overall, the mesostasis is fresh, with slight to moderate alteration (3%–17%) affecting some sections. In such instances, the mesostasis has undergone patchy replacement by saponite and/or celadonite.

Basalt ± Hyaloclastite Breccia

Breccia was recovered within intervals 168-1026B-3R-1, 0–79 cm, and 168-1027B-62X-CC, 35–42 cm, and represents Unit 2 in both holes (Figs. 12, 14; Table 6). The breccia from Hole 1026B consists of angular to subangular basalt and hyaloclastite clasts, along with microlites of plagioclase set within a matrix rich in granular saponite and zeolite (Fig. 18). The clasts are variably replaced by pale brown granular saponite ± carbonate and exhibit concentric alteration from the rims into the cores; these alteration rims are generally ≤0.4 mm thick. In all cases, the glassy shards and chilled glassy margins along the rims of basalt clasts have been more susceptible to alteration than the aphanitic basalt. In some fragments of unaltered to partially altered basalt and glass, variolitic to subvariolitic textures can be recognized. One basaltic clast contains an altered euhedral olivine microphenocryst, whereas others contain a trace amount of plagioclase microlites; all other basaltic clasts are cryptocrystalline. (The pertinent alteration features of this breccia are discussed below in more detail within the "Basement Alteration" subsection.)

The breccia in Section 168-1027B-62X-CC consists of angular to subangular, aphyric basaltic clasts set within a muddy sedimentary matrix. The clasts vary in color (probably as a result of hydrothermal alteration) and texture (e.g., variolitic, subvariolitic, and pilotaxitic) and possibly represent broken clasts from different levels within a cooling unit. All clasts are aphanitic and aphyric to sparsely phyric.

A detailed analysis of one sparsely vesicular clast reveals that petrologically it is very similar to other aphyric basalts found within Holes 1026 and 1027 (Fig. 19). The basalt contains a trace amount of euhedral to subhedral plagioclase phenocrysts (≤1.2 mm) and completely altered euhedral to skeletal olivine (and/or pyroxene) phenocrysts (≤0.8 mm). Both the plagioclase and olivine phenocrysts occur as solitary crystals, as well as within monomineralic (plagioclase only) and bimineralic glomeroporphyritic clots. The groundmass consists of microphenocrysts, microlaths, and microlites of plagioclase (≤0.2 mm; 15%), subhedral to skeletal olivine (± pyroxene; ≤0.2 mm) altered to secondary carbonate and clay (0.3% present; original abundance 3.5%), euhedral to subhedral magnetite (≤0.01 mm; ≤2%), and trace amounts of pyrite (≤0.01 mm). The surrounding mesostasis (equivalent to 75% of the total rock volume) consists of dark cryptocrystalline to lighter microcrystalline material, exhibiting a faint pilotaxitic texture. Slight alteration (≤7%) has affected patches of the mesostasis, altering it to yellow-brown saponitic clay.

Diabase

The only diabase found within the Rough Basement sites was from Hole 1027C (Unit 3; Fig. 15; Table 6). The unit consists of a plagioclase-pyroxene-olivine diabase characterized by a holocrystal-

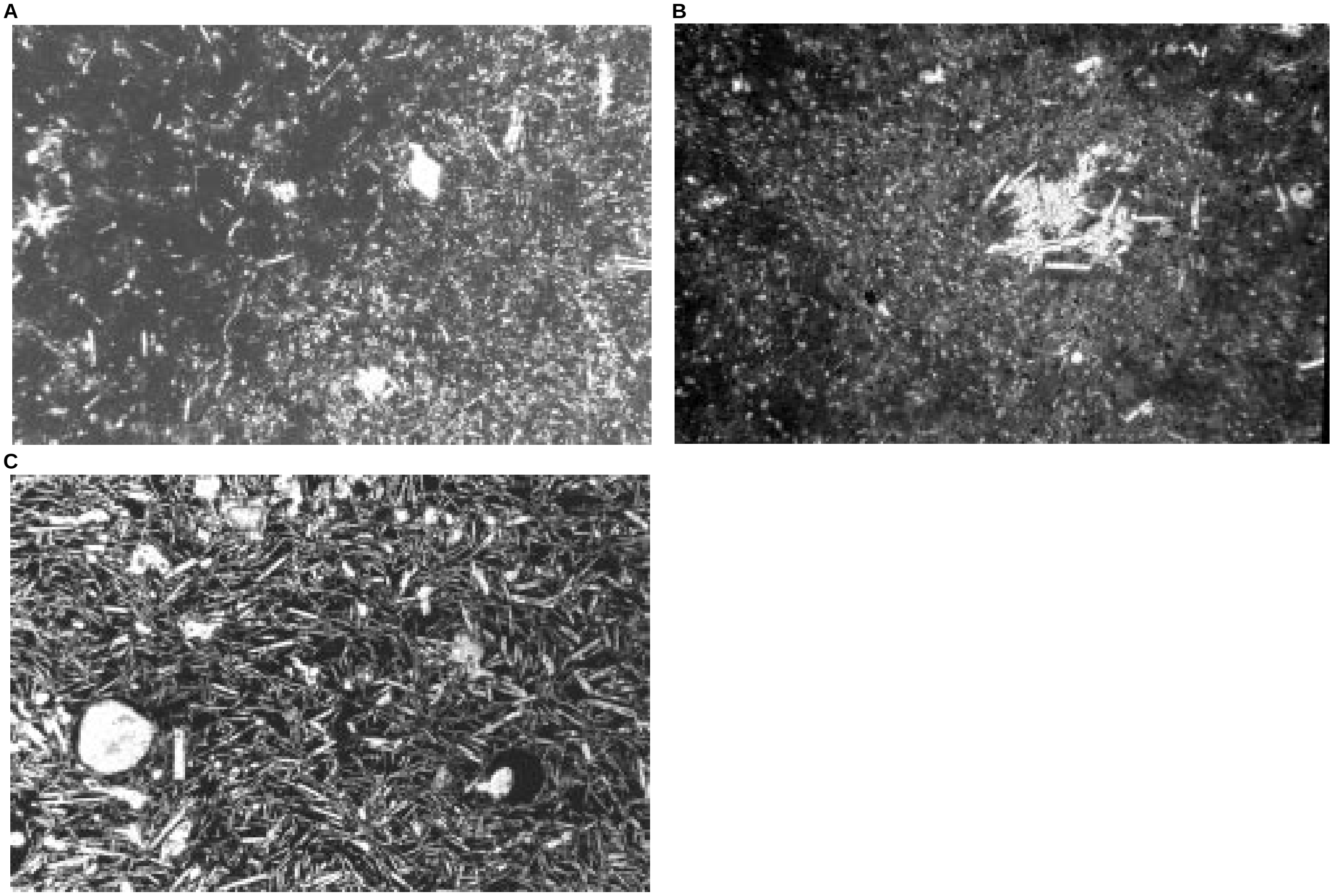

Figure 16. Photomicrographs in plane-polarized light illustrating typical mineral assemblages, abundances, and groundmass textures within the aphyric basalts from (**A**) Hole 1026B (Sample 168-1026B-4R-1, 35–44 cm), (**B**) Hole 1026C (Sample 168-1026C-16R-1, 40–45 cm), and (**C**) Hole 1027B (Sample 168-1027B-60X-CC, 35–38 cm). Note the change in average grain size from Hole 1026B to Hole 1027C. Fields of view = 5.1 mm.

line, intergranular, subophitic to ophitic texture (Fig. 20A). The grain size varies from fine to medium grained throughout the section, grading into a very fine-grained, holocrystalline, aphyric basalt at the base. Although no similar aphanitic unit was recovered at the top of this unit, there is a slight textural change in the diabase, which becomes sparsely vesicular and contains ≤0.2% round gas vesicles (0.6–0.7 mm diameter) at the top of the section.

Within the diabase, there is no systematic variation in the modal mineral abundances of the main rock-forming minerals. Plagioclase occurs as 0.2- to 2.2-mm subhedral laths (characterized by a seriate texture) and is equivalent to 50%–54% of the total rock volume. Some plagioclase crystals exhibit clear, normal, simple zoning, whereas others portray a more complex oscillatory zoning pattern. The next most abundant phase is pyroxene (22%–33%), forming subhedral to anhedral grains (≤3 mm; average = 0.8 mm). Throughout the diabase, pyroxene is characterized by a strongly ophitic to subophitic texture. Although the majority of pyroxene is fresh, some grains exhibit minor alteration (~3%) to pale brown saponite.

Olivine occurs interstitially between the plagioclase laths, as well as enclosed poikilitically within pyroxene. The majority of olivine has either been completely or partially hydrothermally altered to pale brown saponite and/or fibrous carbonate; only 3%–7% fresh olivine remains (point counts indicate that the diabase originally contained between 8% and 15% olivine). In general, all olivine crystals are subhedral to rounded, varying in size from 0.1 to 0.6 mm (average = 0.3 mm). Magnetite and ilmenite also occur interstitially and are present as discrete intergrown granular to rounded and skeletal to elongate grains (0.1–0.3 mm). In addition to the opaque oxides, a trace amount of primary magmatic pyrite (±chalcopyrite) is present interstitially, forming small (≤0.05 mm), globular grains that are either solitary (representing immiscible droplets) or intergrown with magnetite. In total, the opaque oxides and sulfides represent 3%–4% of the total rock volume. Overall, the extent of alteration is slight to moderate (6%–22%) within the diabase.

Aphyric Basaltic Chilled Margin

The holocrystalline, aphyric to sparsely phyric basalt at the base of the diabase (interval 168-1027C-1R-6, 50–72 cm) is characterized by an intersertal, sparsely vesicular texture that terminates in a glassy to variolitic chilled margin (Figs. 15, 20B). It contains ≤2% phenocrysts, of which ~1% is represented by euhedral to subhedral laths and skeletal grains of plagioclase (0.4–1.2 mm; average = 0.8 mm), whereas the other 1% consists of euhedral to subhedral olivine pseudomorphs (≤0.5 mm) that have been completely replaced by fibrous to massive brown saponite.

The groundmass mineralogy consists of plagioclase and olivine (the latter being completely replaced by saponite), associated with opaque oxides, opaque sulfides, and trace amounts of granular to fibrous pyroxene, set within a cryptocrystalline mesostasis. Euhedral to subhedral plagioclase microlaths, microlites, and quench crystals (swallowtails and hollow crystals) have coalesced in stellate clusters, forming an intersertal network, with all other phases occurring interstitially. The relative plagioclase abundance within the aphyric basalt is 46%. All groundmass olivine (subhedral to euhedral, ≤0.2 mm) has

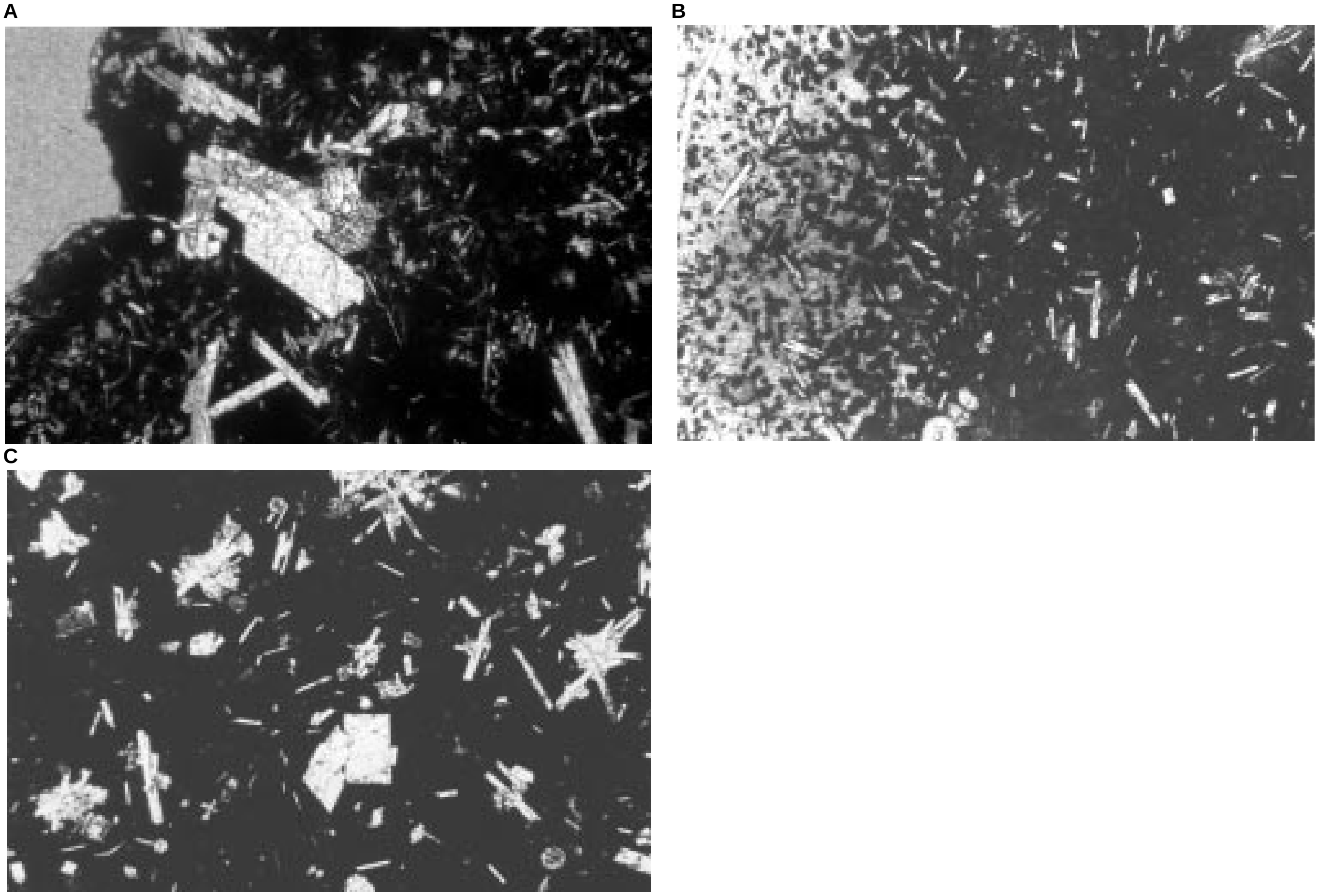

Figure 17. Photomicrographs in plane-polarized light illustrating typical mineral assemblages, abundances, and whole rock/groundmass textures within the sparsely to moderately phyric basalts from Hole 1026B and Hole 1027C. **A.** Sample 168-1026B-5R-1, 46–49 cm. **B.** Sample 168-1027C-4R-2, 85–89 cm. **C.** Sample 168-1027C-5R-4, 68–70 cm. Note the increase in grain size of the groundmass from Hole 1026B to 1027C. Fields of view = 5.1 mm.

Figure 18. Photomicrograph in plane-polarized light of basalt-hyaloclastite breccia (Sample 168-1026B-3R-1, 0–79 cm), illustrating the general textural relationship of the rock including the various states of alteration of the glass shards compared with the basalt fragments (dark gray). Field of view = 5.1 mm.

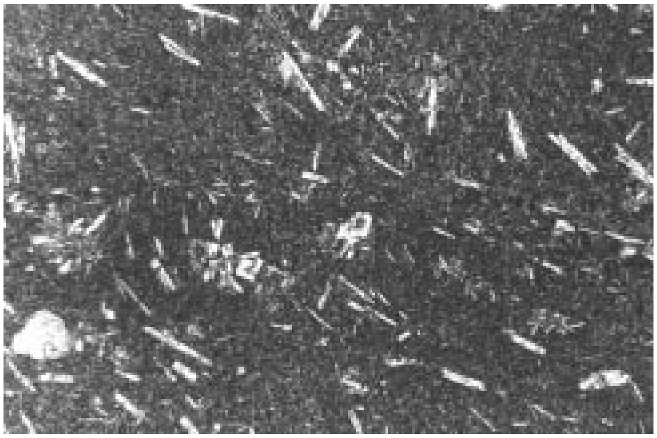

Figure 19. Photomicrograph in plane-polarized light of a basalt clast (Sample 168-1027B-62X-CC, 35–42 cm) removed from the breccia from Hole 1027B. Note the textural and petrologic similarities between this basalt and the aphyric basalts from Holes 1026 and 1027. Field of view = 5.1 mm.

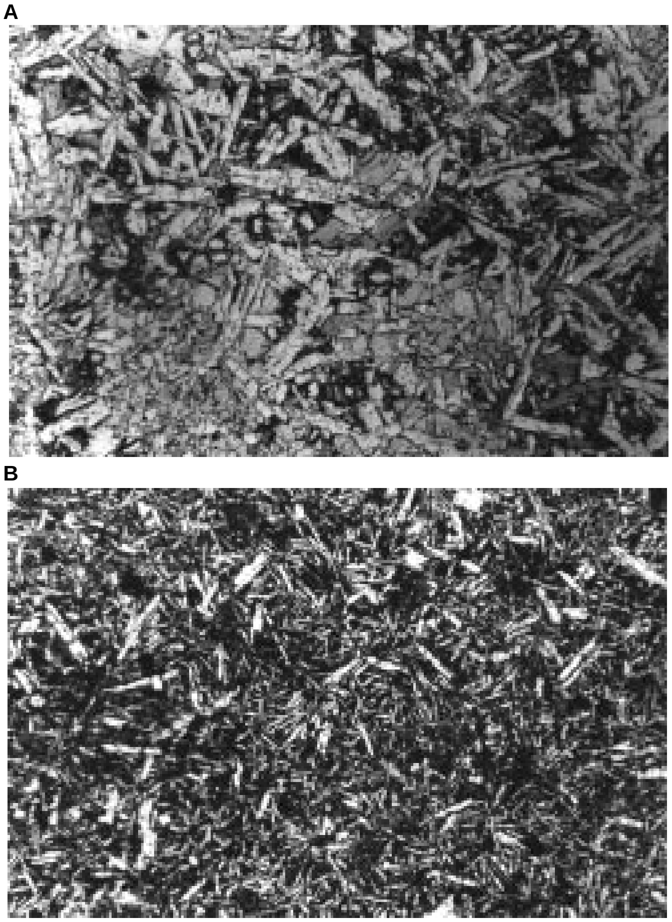

Figure 20. **A.** Photomicrograph in plane-polarized light of the diabase sill from Hole 1027C, illustrating the diabasic texture and mineralogy (Sample 168-1027C-1R-1, 38–42 cm). **B.** Photomicrograph in plane-polarized light of the aphyric chilled basalt margin at the base of the diabase, exhibiting an intersertal texture (Sample 168-1027C-1R-6, 67–70 cm). Fields of view = 5.1 mm.

been replaced by saponite; point counting indicates an original abundance of ~0.5%. Unlike the diabase where pyroxene was the second most abundant mineral phase, microcrystalline pyroxene represents only a trace amount of the basaltic margin (present as ≤0.05-mm granular grains that have been partially altered to saponite), whereas the vast majority of pyroxene occurs as fine fibers within the mesostasis.

The main opaque phase within the groundmass is magnetite (≤4%), although a trace amount of primary magmatic pyrite is present. The magnetite occurs as euhedral to granular and skeletal grains (≤0.02 mm) that form within the mesostasis and granular pyroxene crystals; all pyrite is granular to globular (≤0.005 mm) and limited to the mesostasis.

The mesostasis occurs in interstitial pockets, consisting of skeletal cryptocrystalline grains ± fibrous pyroxene, with a general sheaf-spherulitic texture. This texture changes to a subvariolitic to variolitic texture toward the glassy chilled margin at the base. Throughout, the basalt contains ≤2% irregular to round gas (0.4–2 mm) and segregation (≤0.8 mm) vesicles, with the actual abundance increasing slightly toward the chilled margin. The gas vesicles are either empty or infilled by fibrous carbonate, whereas the segregation vesicles are filled by either microcrystalline pyroxene and opaque minerals or cryptocrystalline mesostasis. Surrounding all segregation vesicles is a band of tangential plagioclase microlites. Alteration within the basalt is slight (<9%).

Glomeroporphyritic Clots

Monomineralic to polymineralic glomeroporphyritic clots are found in a number of aphyric and sparsely to moderately phyric pillow basalts from Holes 1026 and 1027; no clots were found in the massive basalts. The clots are composed of some or all of the same mineral phases present as phenocrysts or within the groundmass of the whole rock; the occurrences and the glomeroporphyritic assemblages present within each sample are listed in Table 8.

Three different morphologic types of glomeroporphyritic clots can be identified within the pillow basalts (“Clot type” in Table 8). The most frequent type (Type 1) consists of monomineralic to polymineralic aggregates of phenocrysts and/or groundmass crystals that have intergrown to form a solid mass with no interstitial mesostasis (Fig. 21A). Although the morphology of the crystals can vary from euhedral to anhedral, the crystals at the outer edges of the clots are distinct and have not undergone any resorption by the surrounding mesostasis. Previous work has shown that these types of clots form by the aggregation of crystals that circulate freely within the magma (Flood et al., 1977; Scarfe and Fujii, 1987). Clustering of this type enhances crystal growth, with all new crystals growing on the faces of others; this prevents mesostasis from being trapped between the crystals. This type of glomeroporphyritic clot is present in all pillow basalts from Holes 1026B, 1026C, 1027B, and 1027C that contain glomeroporphyritic clots.

Two other types of glomeroporphyritic clots were found in pillow basalts from Hole 1026C. The second consists of intergrown aggregates of phenocrysts and/or groundmass crystals (either monomineralic, bimineralic, or polymineralic) and is similar to “Type 1” except for two fundamental differences (Fig. 21B). First, interstitial mesostasis is present between the intergrown crystals, and it is either optically similar to the mesostasis in the rest of the sample or darker in color and massive rather than cryptocrystalline in texture. Second, the external edge of the clot has been partially resorbed by the surrounding mesostasis; this has resulted in a rounded to embayed outline, which is commonly rimmed by a band of pale mesostasis (≤0.5 mm) immediately adjacent to the glomeroporphyritic clot. This type of clot is believed to represent aggregates of crystals that have grown or accumulated against a solid surface (e.g., a chamber wall) and have trapped mesostasis between the grains interstitially (Flood et al., 1977; Scarfe and Fujii, 1987). Circulating currents (induced by convective flow, magma transport, and/or the input of a new batch of magma into the system) could result in crystal clots being ripped up and incorporated into the main body of the magma. Such reworking is likely to incorporate crystals that are chemically different from the main magmatic body (i.e., incorporating more primitive and/or earlier fractionation phases). As a result, these glomeroporphyritic clots may be in a state of disequilibrium with respect to the surrounding melt and are, therefore, susceptible to resorption. Their presence is indicative of either (1) an actively convecting magma body; (2) the vigorous transportation of a crystallizing magma body; and/or (3) the forceful recharge of a crystallizing magma body.

The third type of glomeroporphyritic clot is also only found within pillow basalts from Hole 1026C (Sample 168-1026C-17R-1 [Piece 8, 31–38 cm]). It consists of an aggregate of small granular pyroxene crystals that form pseudomorphs of either olivine and/or pyroxene phenocrysts (based on the morphology of the pseudomorph) (Fig. 21C). Enclosed within this aggregate are plagioclase microlaths, which may have been trapped by the original phenocryst or may have been incorporated later. The replacement of one phase by another is indicative of a disequilibrium reaction caused by changes in the magmatic temperature, pressure, and/or composition of the system (Flood et al., 1977).

Table 8. Occurrence, mineralogy, and type of glomeroporphyritic clots present within aphyric to moderately phyric basalts from Holes 1026 and 1027.

Sample	Basalt type	Phenocrysts	Glomeroporphyritic phases	Clot type
168-1026B-1R-1 (Piece 7, 29–33 cm)	Aphyric	Plagioclase-pyroxene-olivine	Plagioclase-pyroxene	1
168-1026B-4R-1 (Piece 7, 36–44 cm)	Aphyric	Plagioclase	Plagioclase	1
168-1026B-5R-1 (Piece 1, 46–49 cm)	Moderately phyric	Plagioclase-pyroxene-olivine	Plagioclase-pyroxene	1
168-1026C-16R-1 (Piece 10, 40–45 cm)	Sparsely phyric	Plagioclase-pyroxene	Plagioclase-pyroxene	2
			Plagioclase*	1
			Plagioclase-pyroxene*	1, 2
			Plagioclase-pyroxene-olivine*	2
168-1026C-17R-1 (Piece 8, 31–38 cm)	Aphyric	Plagioclase-pyroxene	Plagioclase	1
			Plagioclase-pyroxene	3
			Plagioclase-pyroxene*	3
168-1027B-62X-CC 39–42 cm†	Aphyric	Plagioclase-olivine/pyroxene?	Plagioclase-olivine/pyroxene	1
168-1027C-4R-1 (Piece 20, 131–136 cm)	Moderately phyric	Plagioclase-pyroxene	Plagioclase	1
168-1027C-4R-3 (Piece 2, 9–14 cm)	Aphyric	Plagioclase-pyroxene-olivine	Plagioclase-pyroxene-olivine	1
168-1027C-5R-1 (Piece 2, 6–10 cm)	Moderately phyric	Plagioclase-olivine	Plagioclase-pyroxene	1
			Plagioclase-pyroxene-olivine	1
168-1027C-5R-1 (Piece 8, 92–96 cm)	Moderately phyric	Plagioclase-olivine	Plagioclase-olivine	1

Notes: All samples are pillow basalts. Clot types are described in full within the text. Types: 1 = aggregate of crystals with no interstitial mesostasis; 2 = partially resorbed aggregate of crystals with interstitial mesostasis; 3 = aggregate of crystals pseudomorphing from a previous phenocryst phase. * = composed from groundmass phases. † = basalt sample is a clast from the breccia.

Thus, the presence of different types of glomeroporphyritic clots within the pillow basalts from Holes 1026 and 1027 is indicative of a dynamic magmatic system characterized by convective currents, fractional crystallization, and/or periodic recharge. Further information may be gained by microprobe analyses of the phases within the glomeroporphyritic clots and the surrounding rock.

Igneous Geochemistry

Introduction

Fifteen representative samples of fresh to moderately altered basalts and diabases from Sites 1026 and 1027 were analyzed for major elements. Bulk-rock geochemical analyses were conducted on at least two samples per hole, and the results are found in Table 9. Rock types range from aphyric basalt (Holes 1026B, 1026C, and 1027B) to diabase and sparsely to moderately phyric basalt (Hole 1027C). The majority of analyzed samples are aphyric; thus, phenocryst abundance has a marginal effect on bulk-rock composition. For almost every sample, a thin section was made from the same piece as the chemical analysis and can be correlated. For samples with clay-rich alteration halos and relatively preserved cores (e.g., 168-1026B-4R-1, 35–44 cm), modal analyses obtained from the thin section and the analyzed piece may not entirely correspond because of the inherent variable volumes of fresh and altered rocks involved. Pieces containing thin fresh glassy margins or consisting of broken fragments with fractures and clay veins will be analyzed, and the results will be reported in the Leg 168 *Scientific Results* volume.

Substantial problems in the calibration of Si resulted in SiO_2 contents being systematically higher (by about 0.8%) than the nominal value of 50.02% for the AII-92-29-1 basalt standard (see “Methods” chapter, this volume). These high values in SiO_2 are also apparent for the studied samples, producing totals of oxides that are systematically higher than 100% (on average around 101%). We chose to report the analyses without any correction factor.

Results

Variation diagrams (Fig. 22) show major elements plotted against magnesium number (Mg#). A first-order observation is that basalt compositions within each unit or even within several units of the same hole are quite homogeneous. However, distinct variations of rock composition do exist between the holes (Table 9). To decipher these variations, a chemical comparison among samples from each hole is shown in Table 10.

The diabase (Unit 3) from Hole 1027C has a different composition than the underlying pillows of Unit 4 by having higher Al_2O_3 and Na_2O, lower Fe_2O_3, and intermediate CaO and TiO_2 concentrations. The chemical characteristics of the diabase are very similar to those of massive basalt fragments from Hole 1027B (Table 10; Fig. 22). In addition, on the basis of their chemical compositions, pillow basalts from Hole 1027C can be separated in two groups of subunits (with the boundary occurring close to the top of Core 168-1027C-5R). The upper basalt group from Hole 1027C includes Subunits 4a–d and has relatively low Mg#, Al_2O_3, and CaO and high Fe_2O_3 and TiO_2; these characteristics are very similar to those of the Hole 1026B pillow lavas (Table 10; Fig. 22). The lower basalt group from Hole 1027C includes Subunits 4e–o and has the highest observed values of MgO and CaO and the lowest TiO_2, Na_2O, and P_2O_5 values, relative to other basalts from the Rough Basement sites (Fig. 22).

Taken altogether, the basalt chemistry is consistent with crystal fractionation trends with increasing TiO_2 (from 1% to 1.8%) and Fe_2O_3 (from 7.5% to 12.3%), with decreasing Mg#. Local variation from the main fractionation trend may be caused by local concentrations of crystals, as is observed in aphyric basalts from Sections 1027B-60X-CC and 61X-CC. These basalts have 30%–33% plagioclase microlites, which can account for the high Al content in the rock (Al_2O_3 = 17.1–18.1 wt%).

Alteration Effects

The primary composition of basalts from Sites 1026 and 1027 was modified by precipitation of clay minerals in interstices and vesicles or as a replacement of groundmass and minerals. The water content of basaltic rocks from Sites 1026 and 1027 is variable (0.8%–1.6%), and on average higher than for the Hydrothermal Transition transect sites (H_2O = 0.2%–1.1%). Some estimation of modifications to the magmatic composition by alteration processes caused by the introduction of clays was done during Leg 148 (Alt, Kinoshita, Stokking, et. al., 1993). In Hole 896A basalts, it was noted that high K_2O and low S in some samples was caused by low-temperature alteration processes. In our study, samples have a uniform K_2O content with the exception of Unit 4 from Hole 1027C. This variation in bulk K_2O may be caused by a variable amount of celadonite (a K-bearing clay) in the basalt. This unit has, locally, the highest modal celadonite content of the basalts from the Rough Basement sites (see “Basement Alteration” subsection, below). Most samples from Sites 1026 and 1027 are devoid of sulfur (≤0.06 wt%), which may have been caused by low-temperature alteration. Two samples from Hole 1026B show a relatively high CO_2 content (0.81–0.94 wt%) caused by carbonate, and samples from Hole 1027C have extremely variable CO_2 contents (0.02–1.1 wt%) linked to variations in the abundance of carbonate in vesicles and veins (Table 10).

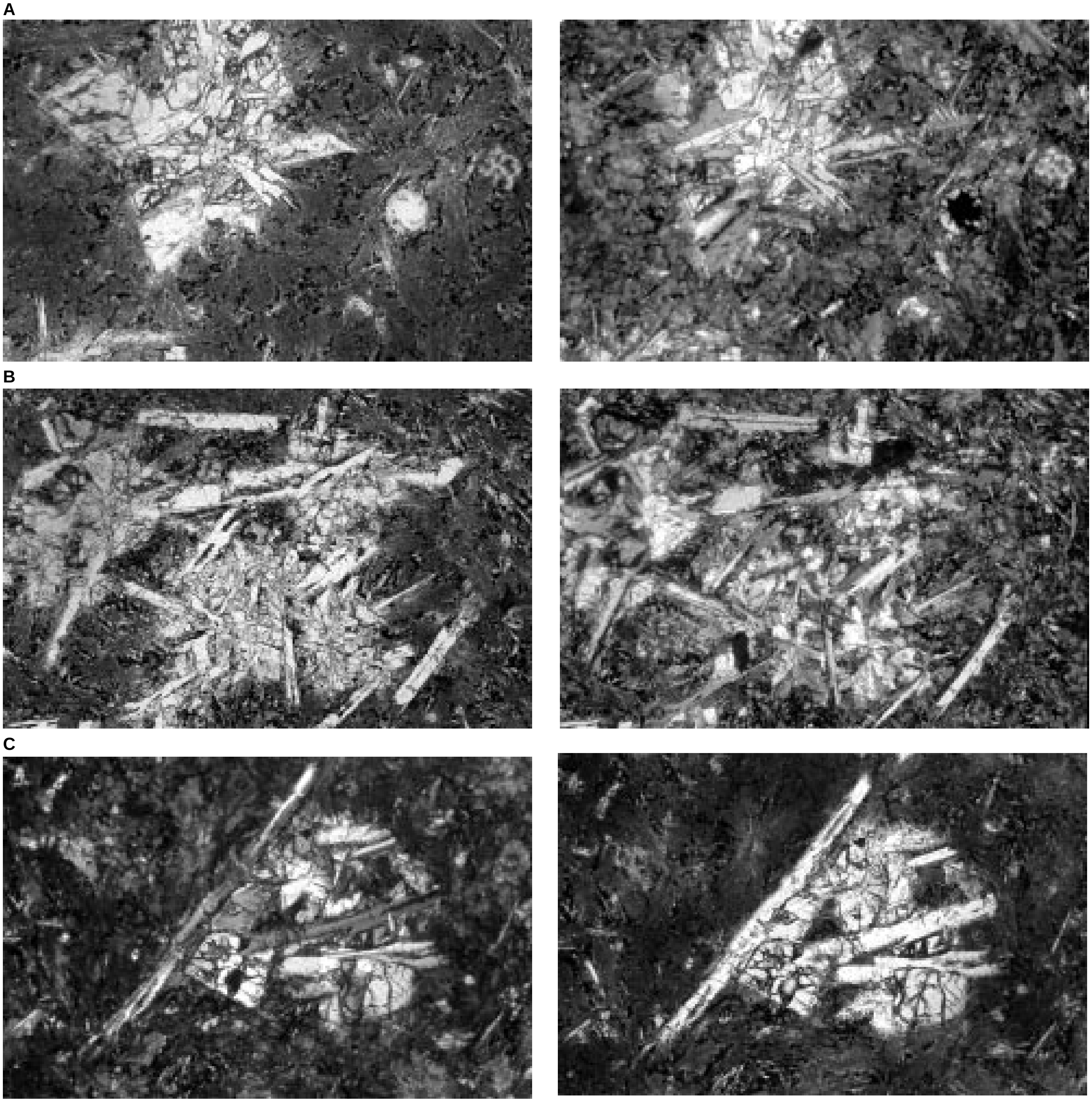

Figure 21. Photomicrographs in plane-polarized (left) and cross-polarized (right) light of the different types of glomeroporphyritic clots found within aphyric to moderately phyric pillow basalts from Holes 1026 and 1027. All photomicrographs are from Sample 168-1026C-16R-1 [Piece 10, 40–45 cm]. Field of view = 5.1 mm. **A.** Type 1: aggregate of crystals with no interstitial mesostasis. **B.** Type 2: partially resorbed aggregate of crystals with interstitial mesostasis. **C.** Type 3: aggregate of crystals pseudomorphing a previous phenocryst phase.

Summary

Petrographic observations and major element chemical analyses allow three distinct groups of rock units to be distinguished. These include (1) distinctly primitive pillow basalts from the lower subunits (4e–o) of Hole 1027C, characterized by low TiO_2, Na_2O, and P_2O_5, and high MgO and CaO; (2) slightly more fractionated pillow basalts from the upper subunits (4a–d) of the pillow lava sequence from Hole 1027C, as well as the pillow basalts from Holes 1026B and 1026C; and (3) the diabase (Unit 1) from Hole 1027C and the massive aphyric basalt from Hole 1027B, which share distinctive chemical compositions relative to the other lithologic groups.

Basement Alteration

Secondary alteration affects all igneous rocks recovered from Sites 1026 and 1027 by variable amounts. Secondary minerals are found in four distinct modes of occurrence: (1) in vesicles, cavity linings, or fillings; (2) in coatings, fracture fillings, and veins; (3) as a replacement of phenocrysts and microphenocrysts; and (4) in patches

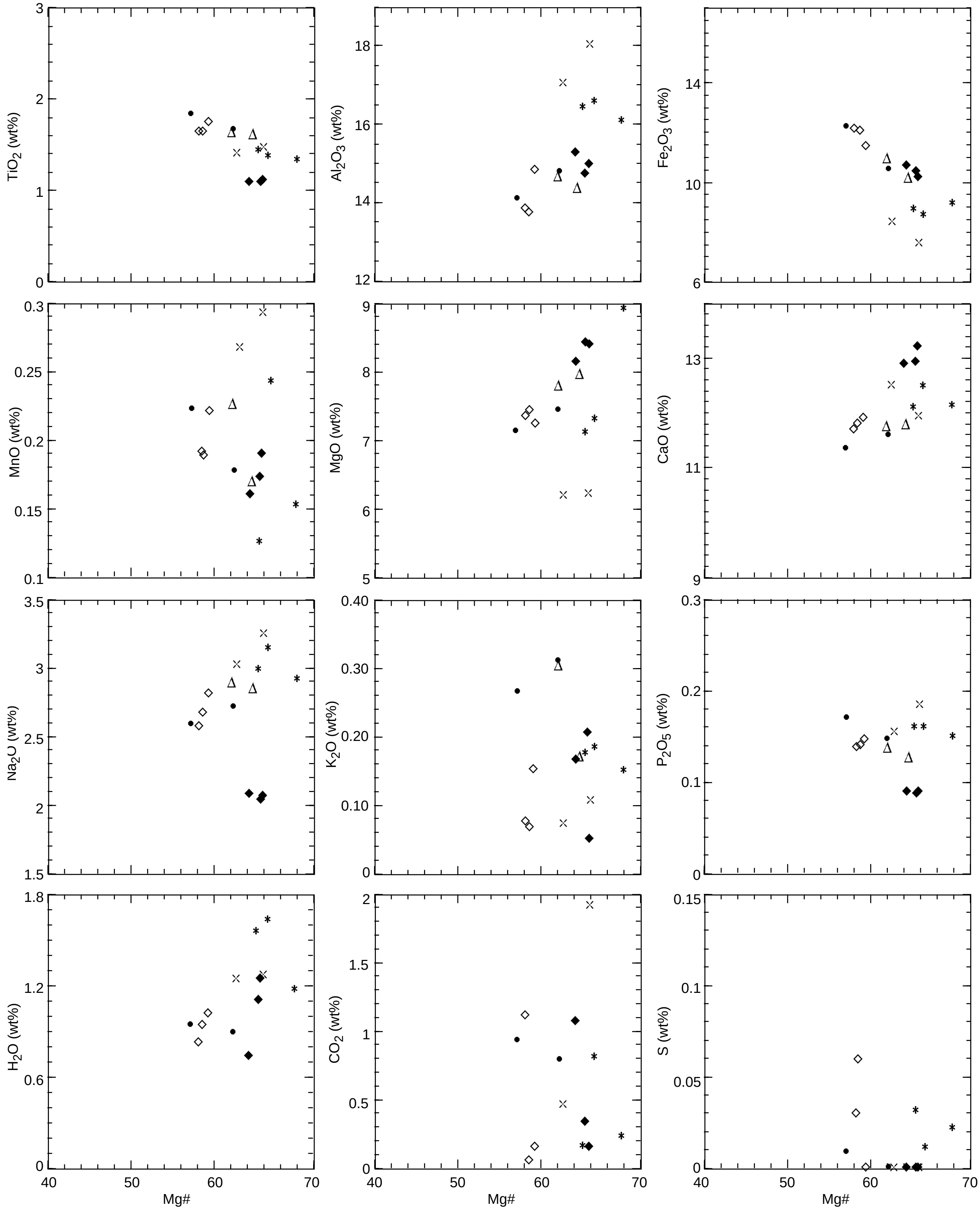

Figure 22. Results of X-ray fluorescence analyses of basaltic rocks from the Rough Basement sites. Each figure represents the weight percent of an oxide, or an elemental ratio, plotted against the Mg# [where Mg# = 100 × MgO/(FeO+MgO), and FeO = 0.9 × (Fe_2O_3*)]. Solid circles = Hole 1026B; open triangles = Hole 1026C; × symbols = Hole 1027B; asterisks = Core 168-1027C-1R; open diamonds = Cores 168-1027C-3R and 4R; and solid diamonds = Core 168-1027C-5R.

Table 9. Geochemical analyses (wt%) of basalts from Sites 1026 and 1027.

Hole:	1026B	1026B	1026C	1026C	1027B	1027B	1027C	1027C	1027C	1027C	1027C	1027C	1027C	1027C	1027C
Core:	1R-1	4R-1	16R-1	17R-1	60X-CC	61X-CC	1R-1	1R-2	1R-6	3R-2	4R-1	4R-2	5R-2	5R-4	5R-5
Interval (cm):	29–33	35–44	40–45	31–38	34–39	22–25	38–42	35–42	55–62	119–121	131–136	9–15	51–55	68–71	121–124
Piece:	7	7	10	8	NA	NA	1B	1A	2	NA	20	2	2	5	11
Depth (mbsf):	256.29	277.35	229.30	238.81	568.90	568.52	585.18	586.28	591.45	606.29	615.01	615.29	625.16	628.03	629.94
Lithology:	A	A	A	A	A	A	D	D	D	M	M	M	M	S	S
Alteration (%):	10	16	9	17	12	9†	20	11	8.6 †	4.6 †	5	6	9	11	4
SiO_2	51.08	51.79	51.12	51.09	51.31	51.43	51.27	50.09	50.49	50.36	50.72	50.74	50.71	51.03	50.95
TiO_2	1.85	1.69	1.64	1.62	1.42	1.48	1.39	1.32	1.36	1.76	1.65	1.65	1.08	1.12	1.09
Al_2O_3	14.08	14.85	14.69	14.34	17.16	18.13	16.34	16.05	16.53	14.87	13.84	13.75	14.77	15.01	15.29
Fe_2O_3*	12.26	10.48	10.93	10.16	8.46	7.54	8.75	9.03	8.58	11.41	12.06	12.02	10.39	10.24	10.59
MnO	0.22	0.18	0.23	0.17	0.27	0.29	0.12	0.15	0.24	0.22	0.19	0.19	0.17	0.19	0.16
MgO	7.17	7.47	7.81	8.00	6.23	6.26	7.08	8.89	7.29	7.25	7.38	7.47	8.43	8.42	8.18
CaO	11.41	11.62	11.77	11.82	12.53	11.98	12.09	12.12	12.46	11.94	11.68	11.84	12.96	13.22	12.93
Na_2O	2.60	2.73	2.89	2.84	3.05	3.27	2.98	2.89	3.12	2.80	2.57	2.68	2.04	2.06	2.08
K_2O	0.27	0.31	0.30	0.17	0.07	0.11	0.17	0.15	0.18	0.15	0.08	0.07	0.21	0.05	0.17
P_2O_5	0.17	0.15	0.14	0.13	0.16	0.19	0.16	0.15	0.16	0.15	0.14	0.14	0.09	0.09	0.09
Total	101.11	101.27	101.52	100.34	100.65	100.68	100.35	100.84	100.41	100.91	100.30	100.55	100.86	101.43	101.52
LOI	0.46	0.93	0.53	0.60	1.27	1.82	1.36	1.62	1.96	0.99	0.53	0.46	0.99	1.16	1.03
H_2O	0.96	0.90	ND	ND	1.27	1.29	1.55	1.16	1.61	1.03	0.83	0.95	1.11	1.26	0.75
CO_2	0.94	0.81	ND	ND	0.48	1.94	0.15	0.22	0.80	0.16	1.13	0.06	0.33	0.17	1.09
S	0.01	0.00	ND	ND	0.00	0.00	0.03	0.02	0.01	0.00	0.03	0.06	0.00	0.00	0.00
Mg#	56.29	61.06	61.14	63.42	61.84	64.63	64.07	68.43	65.17	58.31	57.38	57.75	64.12	64.41	62.96
K/Ti	0.20	0.26	0.26	0.14	0.07	0.10	0.17	0.16	0.18	0.12	0.06	0.06	0.27	0.06	0.21
K/P	2.97	4.01	4.22	2.50	0.90	1.10	2.05	1.92	2.17	2.00	1.04	0.94	4.44	1.04	3.48

Note: Rock types: A = aphyric basalt, S = sparsely phyric basalt, M = moderately phyric basalt, and D= diabase. NA = not applicable. † = percent of alteration was determined from an adjacent piece. Fe_2O_3* is the total amount of iron expressed as Fe_2O_3. Mg# = 100×Mg/(Mg+Fe^{2+}), where Fe^{2+} = 0.9 × Fe total. LOI = loss on ignition. ND = not determined.

within mesostasis. In the following sections, the alteration minerals will be described, as will specific alteration characteristics of the rocks such as the alteration intensity, halos, veins, breccias, and the spatial variability of hydrothermal alteration between various units at Sites 1026 and 1027.

Secondary Minerals

The following secondary minerals were identified by means of hand-specimen observation, optical characteristics in thin section, and powder XRD: clay minerals, iddingsite, carbonates, zeolites, talc, and sulfides (Table 11). Table 12 summarizes the results of shipboard XRD studies.

Clay Minerals

Clay minerals are the most abundant secondary products and are ubiquitous in being present in all four modes (i.e., in vesicles, in veins, as a mineral replacement, and in the mesostasis). Clay minerals were determined optically following the criteria of Honnorez et al. (1983) and Laverne et al. (1996). X-ray diffractograms of numerous clay minerals, including those of air-dried and glycolated powder mounts, confirm the presence of one main type: trioctahedral smectite (saponite, d_{060} = 1.53 Å).

Saponite is the most common clay, and it has been identified in all samples (Table 11). It occurs as cryptocrystalline granular or fibrous aggregates and varies in color from olive green to green, greenish blue, and pale blue in hand specimens and from pale brown (most commonly) to yellowish, brownish green and olive green in thin section. In weakly altered samples, saponite lines vesicles in layers as thin as 10 µm, whereas in more heavily altered samples, it may completely fill vesicles. Saponite is the most commonly observed mineral to alter olivine phenocrysts or microphenocrysts, either singly or with other minerals. Saponite is common both as a vein mineral (alone or with other minerals) and as a replacement of mesostasis. It also forms the matrix of the basalt-hyaloclastite breccia.

Celadonite forms cryptocrystalline granular or fibrous aggregates and is bright green both in hand specimen and in thin section. It forms vesicle linings or complete fillings, veins, and massive botryoidal patches in mesostasis and, as a replacement of olivine, is commonly intergrown with other minerals (e.g., saponite and iddingsite). Celadonite is more restricted in occurrence than saponite (Table 11) and is a characteristic mineral (along with iddingsite) of the oxidative style of alteration (Laverne et al., 1996; Teagle et al., 1996; see discussion below).

Iddingsite

Iddingsite is a mixture of clay mineral(s) and Fe oxyhydroxide and has a characteristic red-orange or reddish brown color both in hand specimen and thin section. It occurs as irregular patches, replacing mesostasis and mafic minerals, as well as lining/filling vesicles and veins. In almost all situations, iddingsite is closely associated with celadonite (Table 11).

Calcium Carbonate

Two polymorphs of calcium carbonate were recognized using optical petrography and XRD: calcite and aragonite. When neither a diffractogram nor thin section (with suitably oriented crystals) was available, this material was simply described as "carbonate." The modes of occurrence observed for carbonate include in veins, in vesicle fills, and as a replacement of olivine (associated with saponite), pyroxene, and plagioclase.

Zeolites

Trace amounts of zeolite are present in veins (with saponite and carbonate) and within the saponite-rich matrix of basalt-hyaloclastite breccia (to as much as 6%). XRD confirms the presence of phillipsite in one vein; however, other zeolites may be present in other rocks. Zeolites commonly form colorless radiating fibrous aggregates or columnar crystals in thin section.

Talc

Talc occurs as fibrous aggregates that, together with saponite ± carbonate, replace olivine phenocrysts. Its distribution is limited to the deepest cores from Site 1027 (Table 11).

Sulfide Minerals

Pyrite is nearly ubiquitous at both Rough Basement sites (Table 11). Commonly present as a trace constituent, pyrite forms fine anhedral grains in cryptocrystalline mesostasis, as well as rounded globular grains in mesostasis, in glass, and enclosed in microlites. This type of pyrite may represent a magmatic or secondary alteration phase.

Pyrite also occurs as fine grains within saponite vesicle and vein fillings, or as fine grains associated with carbonate, suggesting a secondary origin. Pyrite associated with (replacing?) magnetite in dia-

Table 10. Summary of comparative petrography and chemistry (wt%) of basaltic rocks from Holes 1026B, 1026C, 1027B, and 1027C.

Hole:	1026B	1026C	1027B	1027C	1027C	
Rock type:	Aphyric basalt	Aphyric basalt	Aphyric basalt	Diabase	Aphyric to moderately phyric basalt	
Unit:	1, 3	1	1	3	4	
Structure:	Pillow lavas	Pillow lavas	Massive lavas	Sill	Pillows	
Texture:	Varitextured	Varitextured	Pilotaxitic to intersertal	Ophitic	Varitextured with glomerocrysts	
Grain size:	Aphanitic cryptocrystalline	Aphanitic cryptocrystalline	Aphanitic cryptocrystalline to microcrystalline	Phaneritic, fine grained	Aphanitic cryptocrystalline to microcrystalline	
Crystallinity:	Hypocrystalline	Hypocrystalline	Hypocrystalline	Holocrystalline to hypocrystalline	Hypocrystalline to hypohyaline	
Vesicles:	Rare (<1%)	Rare (<1%)	Present (1%–6%; avg = 3%)	Rare (<1%)	Scarce in Subunits 4a–d (≤2%) Rare in Subunits 4e–o (<1%)	
Alteration (%):	9–16	9–17	9–12	9–20	4–11	
Comments:	Saponite + celadonite + iddingsite ± carbonate	Saponite + celadonite + iddingsite	Saponite + carbonate	Saponite + carbonate	Saponite + celadonite + iddingsite ± carbonate	
Samples analyzed:	2	2	2	3	3 Subunits 4a–d	3 Subunits 4e–o
TiO_2	1.7–1.9	1.6	1.4–1.48	1.3	1.7–1.8	1.1
Al_2O_3	14.1–14.9	14.3–14.7	17.2–18.1	16.1–16.5	13.8–14.9	14.8–15.3
Fe_2O_3	10.5–12.3	10.2–10.9	7.5–8.5	8.6–9.0	11.4–12.1	10.2–10.6
MgO	7.3	7.9	6.3	7.1–8.9	7.3–7.5	8.2–8.4
Na_2O	2.7	2.7–2.9	3.1–3.3	2.9–3.1	2.6–2.8	2.1
K_2O	0.27–0.31	0.17–0.30	0.07–0.11	0.15–0.18	0.07–0.15	0.05–0.21
P_2O_5	0.16	0.14	0.16–0.19	0.16	0.15	0.09
H_2O	0.9	ND	1.3	1.2–1.6	0.8–1.0	0.8–1.3
CO_2	0.8–0.9	ND	0.5–1.9	0.2–0.8	0.1–1.1	0.2–1.1
Mg#	56.3–61.1	61.1–63.4	61.8–64.6	64.1–68.4	57.4–58.3	63.2–64.6
K/Ti	0.20–0.26	0.14–0.26	0.07–0.10	0.16–0.18	0.06–0.12	0.06–0.27

Note: avg = average. ND = not determined.

Table 11. Summary of secondary minerals observed in thin sections of basaltic rocks from the Rough Basement Transect sites.

Sample	Structure	Fresh glass	Altered glass	Saponite	Carbonates	Celadonite	Iddingsite	Pyrite	Talc	Chlorite	Zeolites
1026B-1R-1 (Piece 7, 29–33 cm)	Pillow basalt			++		++	++	+			
1026B-3R-1 (Piece 8, 59–62 cm)	Hyaloclastite breccia	++	+++	+++	++			Tr			+++
1026B-4R-1 (Piece 7, 35–44 cm)	Pillow basalt	++	++	+++		++	+++	Tr			Tr
1026B-5R-1 (Piece 1, 46–49 cm)	Pillow basalt			++		+	Tr	Tr			
1026C-16R-1 (Piece 10, 40–45 cm)	Pillow basalt			++		++	++				
1026C-17R-1 (Piece 8, 31–38 cm)	Pillow basalt			+++		+++	++	Tr			
1027B-60X-CC (Piece 5, 33–36 cm)	Massive basalt			+++	+			Tr		Tr?	Tr?
1027B-61X-CC, 13–15 cm	Massive basalt			+++	++			Tr		Tr?	
1027B-61X-CC, 25–28 cm	Massive basalt			+++	++			Tr			
1027B-62X-CC, 7–10 cm	Massive basalt			+++	++		Tr				
1027B-62X-CC, 39–42 cm	Basalt breccia			++	++						
1027C-1R-1 (Piece 1, 10–16 cm)	Diabase			+++	++						
1027C-1R-1 (Piece 1B, 39–42 cm)	Diabase			+++	Tr			Tr			
1027C-1R-2 (Piece 1A, 35–42 cm)	Diabase			+++	Tr			Tr			
1027C-1R-4 (Piece 1C, 65–68 cm)	Diabase			+++	Tr			Tr			
1027C-1R-6 (Piece 2, 67–70 cm)	Diabase			+++	++			Tr			
1027C-3R-2 (Piece 5, 125–126 cm)	Pillow basalt			+	Tr	++					
1027C-4R-1 (Piece 11, 63–67 cm)	Pillow basalt			++	Tr	+++	++	Tr			
1027C-4R-1 (Piece 17, 110–113 cm)	Pillow basalt	+		+++		++	+				
1027C-4R-1 (Piece 20, 131–136 cm)	Pillow basalt			++	Tr						
1027C-4R-2 (Piece 2, 9–15 cm)	Pillow basalt			+++	+						
1027C-4R-2 (Piece 9C, 85–89 cm)	Pillow basalt	+		+++	++						++
1027C-4R-3 (Piece 2, 9–14 cm)	Pillow basalt			++	++	++	++	Tr	Tr		
1027C-5R-1 (Piece 2, 6–10 cm)	Pillow basalt			++		Tr	Tr				
1027C-5R-1 (Piece 8, 92–96 cm)	Pillow basalt			+++		++	++	Tr			
1027C-5R-2 (Piece 1A, 1–9 cm)	Pillow basalt	+++		+++	Tr			Tr	Tr		Tr
1027C-5R-2 (Piece 2, 49–51 cm)	Pillow basalt			++	Tr	++	+	Tr	++		
1027C-5R-3 (Piece 8, 105–109 cm)	Pillow basalt	+		++	Tr			Tr	Tr		
1027C-5R-4 (Piece 5, 68–70 cm)	Pillow basalt			+++	+			Tr	+		
1027C-5R-5 (Piece 3, 32–43 cm)	Pillow basalt			++	Tr	+	++	Tr	Tr		
1027C-5R-5 (Piece 11, 121–123 cm)	Pillow basalt			++	Tr	+	+	Tr			

Note: Tr? = possible trace amount, Tr = trace, + = <1%, ++ = 1%–5%, and +++ = >5%.

Table 12. Results of shipboard X-ray diffraction studies performed on secondary minerals from the Rough Basement Transect sites.

Sample	(060)*	(001)*	(001)-GLY*	Description	Mineral
168-1026B-4R-1 (Piece 2, 5–12 cm)	NA	NA	NA	White vein	Phillipsite
168-1026C-16R-1, 13 cm	1.536	14	ND	Red clay vein	Hematite + calcite + trioctahedral clay
168-1026C-16R-1, 46 cm	1.533	15.6	ND	Tan material	Calcite + trioctahedral clay
168-1027B-61X-CC, 23–30 cm	ND	13.5	14.3	Green vein	Smectite
168-1027B-61X-CC, 40–42 cm	NA	NA	NA	White vein	Calcite
168-1027C-1R-1 (Piece 1A, 18–20 cm)	1.533	14	ND	White vein	Calcite + trioctahedral clay
168-1027C-4R-1 (Piece 17, 109–112 cm)	1.539	13.7	ND	Green vein	Trioctahedral clay
168-1027C-4R-2 (Piece 2A, 8–22 cm)	1.535	13.3	ND	Green vein	Trioctahedral clay
168-1027C-4R-3, 46 cm	1.535	14	ND	Green vein	Trioctahedral clay
168-1027C-4R-3 (Piece 10B, 103–116 cm)	NA	NA	NA	White vein	Aragonite + trace calcite
168-1027C-5R-1 (Piece 4, 18–28 cm)	1.534	13.8	ND	Green vein	Trioctahedral clay
168-1027C-5R-1 (Piece 7, 60–64 cm)	1.540	14	ND	Green vein	Trioctahedral clay
168-1027C-5R-2 (Piece 7, 115–124 cm)	1.539	13.1	ND	Green vein	Trioctahedral clay
168-1027C-5R-3 (Piece 3, 24–52 cm)	1.540	13.6	ND	Green vein	Trioctahedral clay
168-1027C-5R-4 (Piece 9, 124–131 cm)	NA	NA	NA	White vein	Aragonite + trace calcite

Notes: * = d-spacing (Å), and GLY = glycolated sample. NA = not applicable, and ND = not determined.

base and pyrite veinlets located at the sediment/basalt contact at Site 1027 is another example of secondary sulfide.

Pyrrhotite occurs as an interstitial mineral in some basalts from Site 1026. The mineral forms anhedral grains, each comprised of several distinctly oriented domains. It occurs in the weakly altered rocks, commonly just inside the leading edge of an oxidative alteration halo, and is absent from the alteration halo itself.

A rare sulfide occurrence is noted in one thin section that contains several large (maximum 2.8 mm) olivine phenocrysts pseudomorphed by saponite and carbonate. Embedded in the clay pseudomorphs are unaltered euhedral spinels and fine flakes or curved acicular bundles of an opaque sulfide identified optically as millerite (NiS).

Alteration Intensity

The amount of alteration determined by point counting the secondary minerals in thin sections (excluding hyaloclastite breccia) varies from 2% to 23% (with most ~12%; Table 13; Fig. 23). Local extremes in alteration intensity vary from some glass rims that appear practically unaltered to centimeter-scale patches of intense alteration (40%–50%) associated with fractures, veins, or alteration halos. Secondary minerals in the basalt-hyaloclastite breccia account for 64% of the rock (Table 13).

The state of olivine is a sensitive petrographic indicator of alteration intensity, as it is typically the first and only crystalline magmatic phase to be replaced in most samples. Clinopyroxene, by contrast, is typically unaltered, whereas plagioclase is rarely altered, and then only partially to saponite (along fractures and cleavage planes or at crystal edges).

Fresh olivine is restricted to some microphenocrysts in some glass pillow rims and to relict crystals in the diabase unit at Site 1027. In glass rims, the chilled basaltic glass apparently protects olivines from hydrothermal fluid, whereas in the diabase, olivines are partially replaced by saponite. This means that hydrothermal fluids have access to olivine in the diabase; however, the incomplete replacement of olivine could indicate a low water:rock ratio, low alteration temperature, or insufficient time for the replacement to be completed.

Table 13. Modal point-count data for secondary minerals in thin sections from Sites 1026 and 1027.

Sample	Structure	Total alteration (%)	Saponite (%)	Carbonate (%)	Celadonite (%)	Iddingsite (%)	Pyrite (%)	Talc (%)	Chlorite (%)	Zeolite (%)	Palagonite (%)
1026B-1R-1 (Piece 7, 29–33 cm)	Pillow basalt	9.6	4	0	3.6	1.3	0.7	0	0	0	0
1026B-3R-1 (Piece 8, 59–62 cm)	Hyaloclastite breccia	64.3	56.1	2.4	0	0	Tr	0	0	5.8	8
1026B-4R-1 (Piece 7, 35–44 cm)	Pillow basalt	16.2	6.8	0	4	5.4	Tr	0	0	Tr	0
1026B-5R-1 (Piece 1, 46–49 cm)	Pillow basalt	2.7	2.1	0	0.6	Tr	Tr	0	0	0	0
1026C-16R-1 (Piece 10, 40–45 cm)	Pillow basalt	9.3	4.2	0	4	1.1	0	0	0	0	0
1026C-17R-1 (Piece 8, 31–38 cm)	Pillow basalt	17.4	8.6	0	7.2	1.6	Tr	0	0	0	0
1027B-60X-CC (Piece 5, 33–36 cm)	Massive basalt	12.2	11.4	0.8	0	0	Tr	0	Tr?	Tr?	0
1027B-61X-CC, 13–15 cm	Massive basalt	12.4	10	2.4	0	0	Tr	0	Tr?	0	0
1027B-61X-CC, 25–28 cm	Massive basalt	9	7.2	1.8	0	0	Tr	0	0	0	0
1027B-62X-CC, 7–10 cm	Massive basalt	9.4	7	2.4	0	Tr	0	0	0	0	0
1027B-62X-CC, 39–42 cm	Basalt breccia	6.4	5	1.4	0	0	0	0	0	0	0
1027C-1R-1 (Piece 1, 10–16 cm)	Diabase	22	18	4	0	0	0	0	0	0	0
1027C-1R-1 (Piece 1B, 39–42 cm)	Diabase	20	20	Tr	0	0	Tr	0	0	0	0
1027C-1R-2 (Piece 1A, 35–42 cm)	Diabase	10.6	10.6	Tr	0	0	Tr	0	0	0	0
1027C-1R-4 (Piece 1C, 65–68 cm)	Diabase	11.6	11.6	Tr	0	0	Tr	0	0	0	0
1027C-1R-6 (Piece 2, 67–70 cm)	Diabase	8.6	6.2	2.4	0	0	Tr	0	0	0	0
1027C-3R-2 (Piece 5, 125–126 cm)	Pillow basalt	4.6	0.6	Tr	4	0	0	0	0	0	0
1027C-4R-1 (Piece 11, 63–67 cm)	Pillow basalt	12	3.8	Tr	6.4	1.8	Tr	0	0	0	0
1027C-4R-1 (Piece 17, 110–113 cm)	Pillow basalt	12.8	4	0	6.4	2.4	0	0	0	0	0
1027C-4R-1 (Piece 20, 131–136 cm)	Pillow basalt	5	5	Tr	0	0	0	0	0	0	0
1027C-4R-2 (Piece 2, 9–15 cm)	Pillow basalt	5.6	5.4	0.2	0	0	0	0	0	0	0
1027C-4R-2 (Piece 9C, 85–89 cm)	Pillow basalt	9.8	5.6	1.4	0	0	0	0	0	2.8	0
1027C-4R-3 (Piece 2, 9–14 cm)	Pillow basalt	11	3.4	2.2	3.6	1.8	Tr	Tr	0	0	0
1027C-5R-1 (Piece 2, 6–10 cm)	Pillow basalt	2.8	2.8	0	Tr	Tr	0	0	0	0	0
1027C-5R-1 (Piece 8, 92–96 cm)	Pillow basalt	23.4	20.6	0	1.6	1.2	Tr	0	0	0	0
1027C-5R-2 (Piece 1A, 1–9 cm)	Pillow basalt	6.7	6.7	Tr	0	0	Tr	Tr	0	Tr	0
1027C-5R-2 (Piece 2, 49–51 cm)	Pillow basalt	9	3.8	Tr	4.8	0.4	Tr	0	0	0	0
1027C-5R-3 (Piece 8, 105–109 cm)	Pillow basalt	3.6	3.6	Tr	0	0	Tr	0	0	0	0
1027C-5R-4 (Piece 5, 68–70 cm)	Pillow basalt	11.4	11	0.4	0	0	Tr	0	0	0	0
1027C-5R-5 (Piece 3, 32–43 cm)	Pillow basalt	5.8	1.2	Tr	0.8	3.8	Tr	Tr	0	0	0
1027C-5R-5 (Piece 11, 121–123 cm)	Pillow basalt	4.2	3.2	Tr	0.4	0.6	Tr	0	0	0	0

Note: Tr = trace amount, and Tr? = possible trace amount.

Alteration Halos

Alteration effects are commonly linked to the presence of alteration halos, which are typically present in pillow basalt samples and absent in diabase. These halos, a few millimeters to several centimeters wide, are common in hand specimen as dark borders on rock pieces, the cores of which are gray (Fig. 24). Some halos have a brown-orange tint owing to the presence of abundant iddingsite-type material in the vesicles and groundmass. Halos are also observed flanking some veins and vein networks that cut across rock (Fig. 24). All halos are logged in the alteration log (ALTNLOG; see Appendix C on CD-ROM, back pocket).

Two examples of alteration halos are explained in more detail in Fig. 25, which illustrates their zoned nature and details the observed mineralogic changes. Zone 1 (the outer zone) contains vesicle fillings, veinlets, olivine replacements, and mesostasis alteration by red-brown iddingsite ± celadonite. The inner zone of the halo (Zone 2) is commonly enriched in celadonite, whereas iddingsite becomes less prevalent. Zone 3 is the gray (nonhalo) portion of the rock, which is characterized by the presence of secondary saponite lining or filling vesicles, together with sulfide minerals. Marked concentrations of interstitial pyrrhotite and pyrite may be noted in discontinuous 0.2-mm-wide bands located just inside the dark halos (see Fig. 22A, "Hydrothermal Transition Transect" chapter, this volume, for an example).

In some pillow basalts, sawed cores produced salt deposits on the surface as they dried. These deposits were most concentrated at the margin of gray rock interiors, just inside the alteration halos (Fig. 26), suggesting that the gray rock is markedly more porous than the alteration halos.

Vesicle Fillings

All vesicles are either lined or completely filled by secondary minerals (Figs. 27–31). Most commonly, vesicles are lined by one or more texturally and mineralogically different clays. The type and sequence of filling is interpreted as a sensitive record of successive changes in the chemical microenvironments affecting the host rock. Vesicle fillings vary systematically, depending on whether the vesicles are in the alteration halos, transitional zones, or the gray rock interiors.

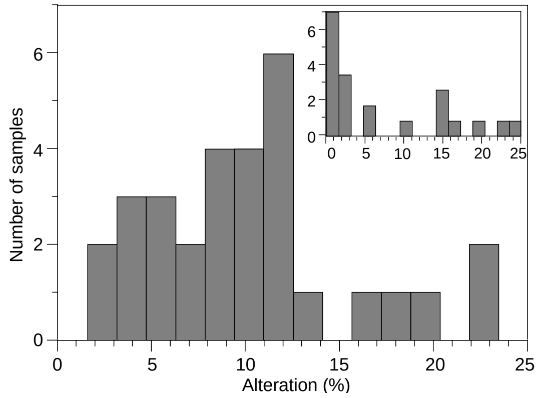

Figure 23. Histogram showing the modal proportion of secondary minerals in thin sections from basaltic rocks from the Rough Basement sites. The basalt-hyaloclastite breccia (64% secondary minerals) is excluded. The inset shows a corresponding histogram constructed for the Hydrothermal Transition sites (see "Hydrothermal Transition Transect" chapter, this volume).

Alteration halos contain vesicles that are typically completely filled by either celadonite or iddingsite, or are filled by a layer of celadonite followed by iddingsite. In the transitional zone inside alteration halos, vesicles may be filled by celadonite, then iddingsite, followed by fibrous saponite and granular, cryptocrystalline saponite with or without pyrite. Examples of these filling textures are shown in Figures 27B, 27C, and 28.

The gray rock that is unaffected by the alteration halo typically contains vesicles lined by fibrous saponite, with or without a second lining or filling by granular saponite (± pyrite). Examples are shown in Figures 27D and 29.

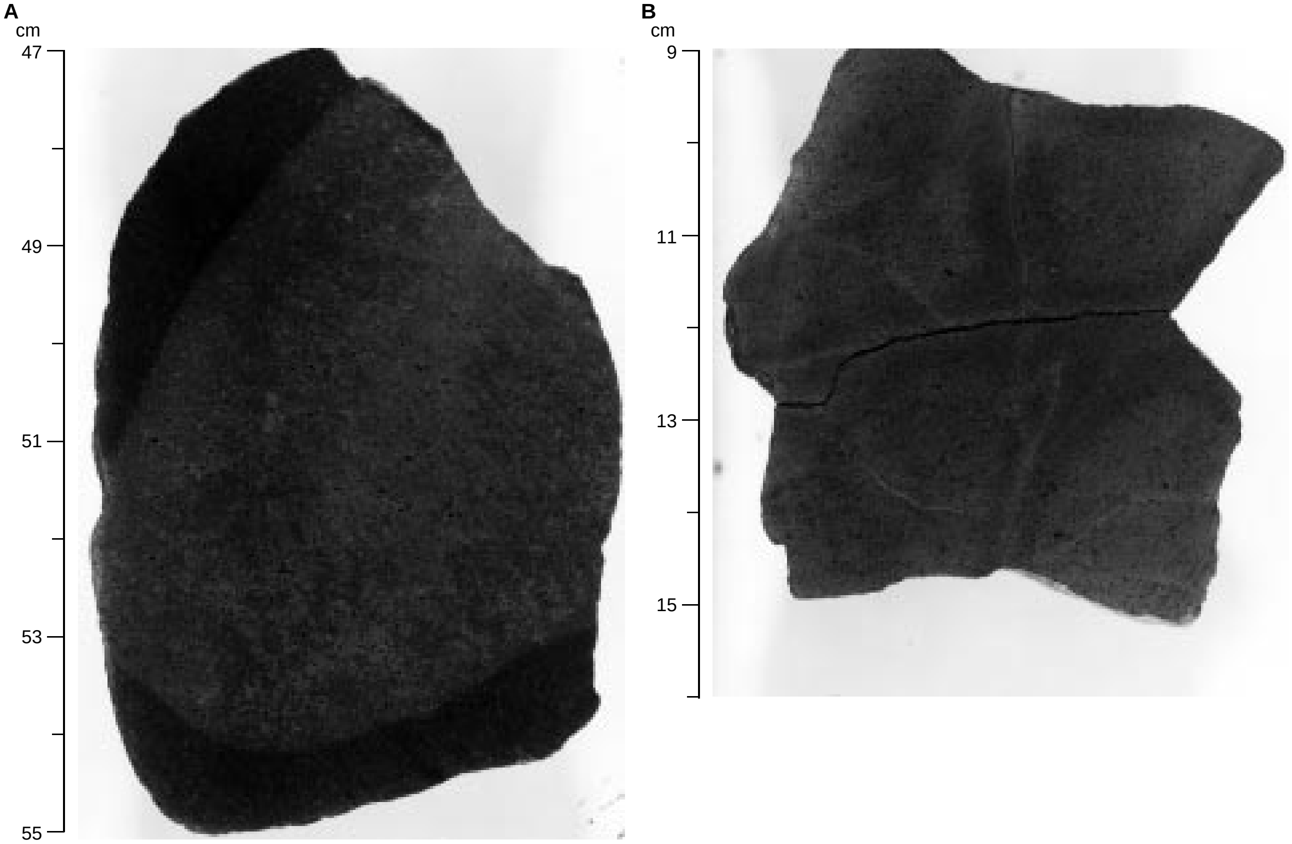

Figure 24. Close-up photographs of alteration halos. **A.** Well-developed dark alteration halo in a pillow basalt fragment (Sample 168-1027C-4R-1 [Piece 9, 47–55 cm]). **B.** Alteration halos flanking veins cutting a pillow basalt fragment (Sample 168-1027C-4R-3 [Piece 2, 9−16 cm]).

Some vesicles in rocks from Site 1027 are carbonate filled (i.e., they represent amygdules). A hand-specimen example is seen in one of the basalt fragments in a breccia (Fig. 14B). Microscopic examples are shown in Figures 27A, 30, and 31. In several examples (Fig. 31), the carbonate may have replaced earlier formed clay.

Veins

Several vein types were noted, and individual occurrences are recorded in the vein log (VEINLOG; see Appendix D on CD-ROM, back pocket). The 1.95 m of hard rock core recovered at Site 1026 yielded three veins: two clay veins and one phillipsite vein (corresponding to 1.5 veins/m). The 0.6 m of hard rock recovered from Hole 1027B contains four carbonate-bearing veins (corresponding to 6.7 veins/m). The 17.5 m of hard rock recovered from Hole 1027C contains a total of 74 veins containing clay and/or carbonate (or 4.6 veins/m). The overall vein abundance is lower than that obtained from a previous basement hole where veins were carefully logged (i.e., Hole 896A at the Costa Rica Rift, which contained 30 ± 20 veins/m). Table 14 shows a comparison between vein data from Hole 896A and Hole 1027C (the Rough Basement hole with the greatest recovery). This comparison indicates that carbonate veins dominate over clay veins along the Rough Basement Transect, in contrast to the dominance of clay veins at the Costa Rica Rift.

Most veins that were logged were not oriented, owing to their nonplanar or discontinuous irregular forms. The exception is the carbonate-bearing veins in the diabase (Unit 3) from Hole 1027C (Appendix D on CD-ROM, back pocket). Eleven veins were oriented relative to the core axis, and dips varied from 5° to 75°. Six of the eleven veins had dips ranging from 40° to 60°, and only three veins had dips of 20° or less.

Clay Veins

Clay or clay-bearing veins are ubiquitous at the Rough Basement sites (Fig. 32). They may be simple dark green veins (Fig. 33A), which probably contain saponite alone, or more complex veins containing light green clay (celadonite), orange clay (iddingsite), and/or white carbonate. Widths vary from several tens of micrometers to a maximum of 3 mm (for monomineralic clay veins) or 7 mm (for clay + carbonate veins). Clay veins are common within alteration halos or centered along the middle of a halo.

Carbonate-Bearing Veins

Veins with calcite or aragonite (as well as calcium carbonate-filled amygdules) are ubiquitous at Site 1027 (Figs. 13, 15) and nearly absent at Site 1026 (a single calcite vein, associated with iddingsite, is present in Hole 1026C core). The Site 1027 carbonate veins are either carbonate alone or polymineralic, associated with dark green clay (saponite) with or without iddingsite. Average vein widths vary from about 20 µm to 7 mm and are most frequently ≤1 mm wide. It is common for vesicles in the vicinity of carbonate-bearing veins to be filled by carbonate as well.

Carbonate veins appear, in many instances, to have black or dark gray alteration halos. In the diabase (Unit 3) of Hole 1027C, such halos are obscure, indicated only by the presence of scant pyrite and weakly developed reddish spots in a 1-mm zone on either side of the vein. In the pillow basalt units (Unit 4a–o) of Hole 1027C, carbonate veins as well as clay veins may be flanked by 4- to 15-mm-wide black alteration halos. The carbonate veins are common along the middle of clay veins, however, some carbonate veins diverge from the center of a clay vein and cut across the black alteration halo. Thus, it would appear that the halos probably formed during the clay-forming stage of vein development.

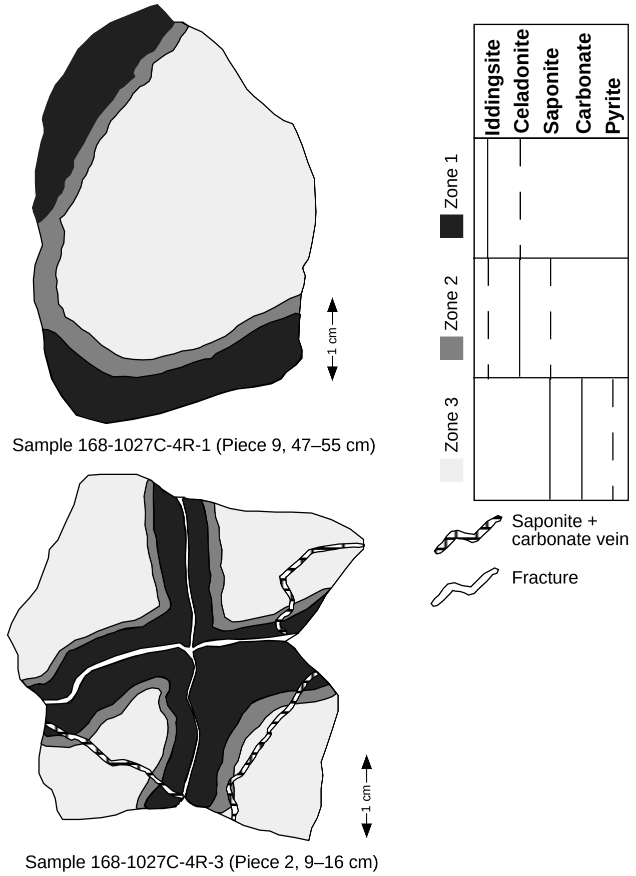

Figure 25. Sketches of alteration halos in the two samples from Hole 1027C that are shown in Figure 24. Mineral distribution within the halos and adjacent rock is shown schematically.

Most carbonate veins have a cross-fiber texture characteristic of displacement-controlled crystal growth involving continuous vein formation as microcracks open. This is true for both carbonate-only veins and carbonate-clay veins, which contain clay fibers as well as carbonate fibers (Fig. 33B).

Calcium carbonate has been identified as both calcite and aragonite, using optical criteria and spot-checking by XRD. Some veins (e.g., Sample 168-1027C-1R-1 [Piece 1A, 0–24 cm]) contain both polymorphs. Similar features were observed in carbonate veins at Site 896A, Costa Rica Rift (Alt, Kinoshita, and Stokking, et al., 1993; Tartarotti et al., 1996).

Zeolite-Bearing Veins

Zeolites are sporadic at the Rough Basement sites, as millimeter-scale veins encrusting rock pieces or cutting crystalline basalts and as tiny veinlets present within the glassy margins of pillow basalts. One encrusting vein was identified as phillipsite by XRD. Photomicrographs of zeolite veins are shown in Fig. 34.

Basalt-Hyaloclastite Breccia

Unit 2 in Hole 1026B is a basalt-hyaloclastite breccia (Figs. 14A, 35A, B). Both basaltic clasts and glass shards are partially to completely altered, primarily to green saponite and white zeolite. The glass shards and glassy rims of basalt fragments are the most altered, whereas the cores of larger shards and of the basalt fragments typically remain less altered. The rock matrix consists primarily of sapo-

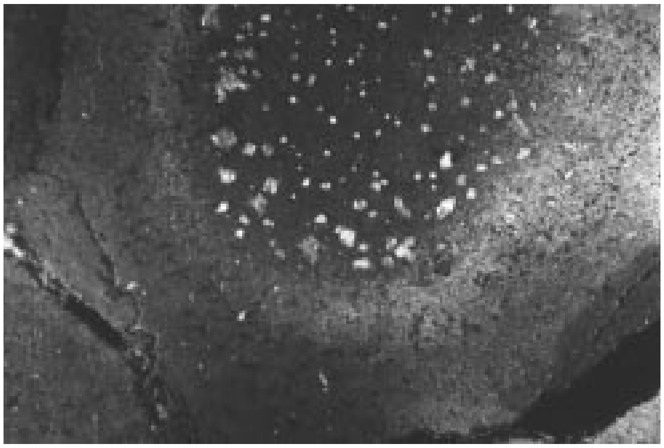

Figure 26. Close-up photograph of a sawed surface on Sample 168-1027C-5R-3 (Piece 5) showing an alteration halo and the salt deposits that formed as the rock dried in the core lab. The salts outline the gray rock interior and are absent from the alteration halo portion. Field of view = 25 mm.

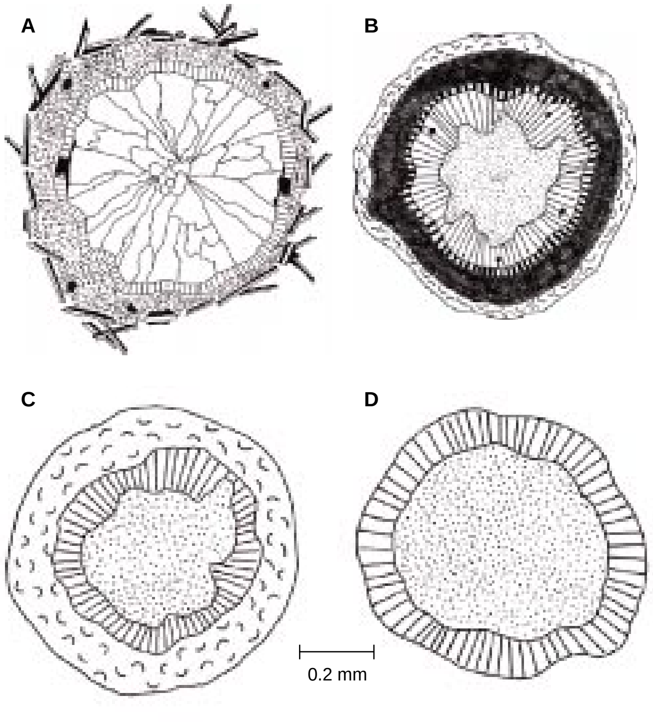

Figure 27. Sketches of vesicles from Rough Basement Transect basaltic rocks. **A.** The vesicle is partially filled by cryptocrystalline magmatic segregation material, followed by an isopachous rim of fibrous saponite, the continuity of which is broken only by two small pyrite blebs. Each pyrite mass has a very thin extension that coats the inner edge of the saponite layer. The remainder of the vesicle is filled by sparry radial calcite. **B.** Sequential vesicle linings include celadonite, followed by iddingsite, granular celadonite(?), fibrous saponite with disseminated pyrite, and, finally, granular cryptocrystalline saponite. **C.** Celadonite is followed by fibrous saponite, then granular saponite. **D.** A lining of fibrous saponite is followed by granular cryptocrystalline saponite.

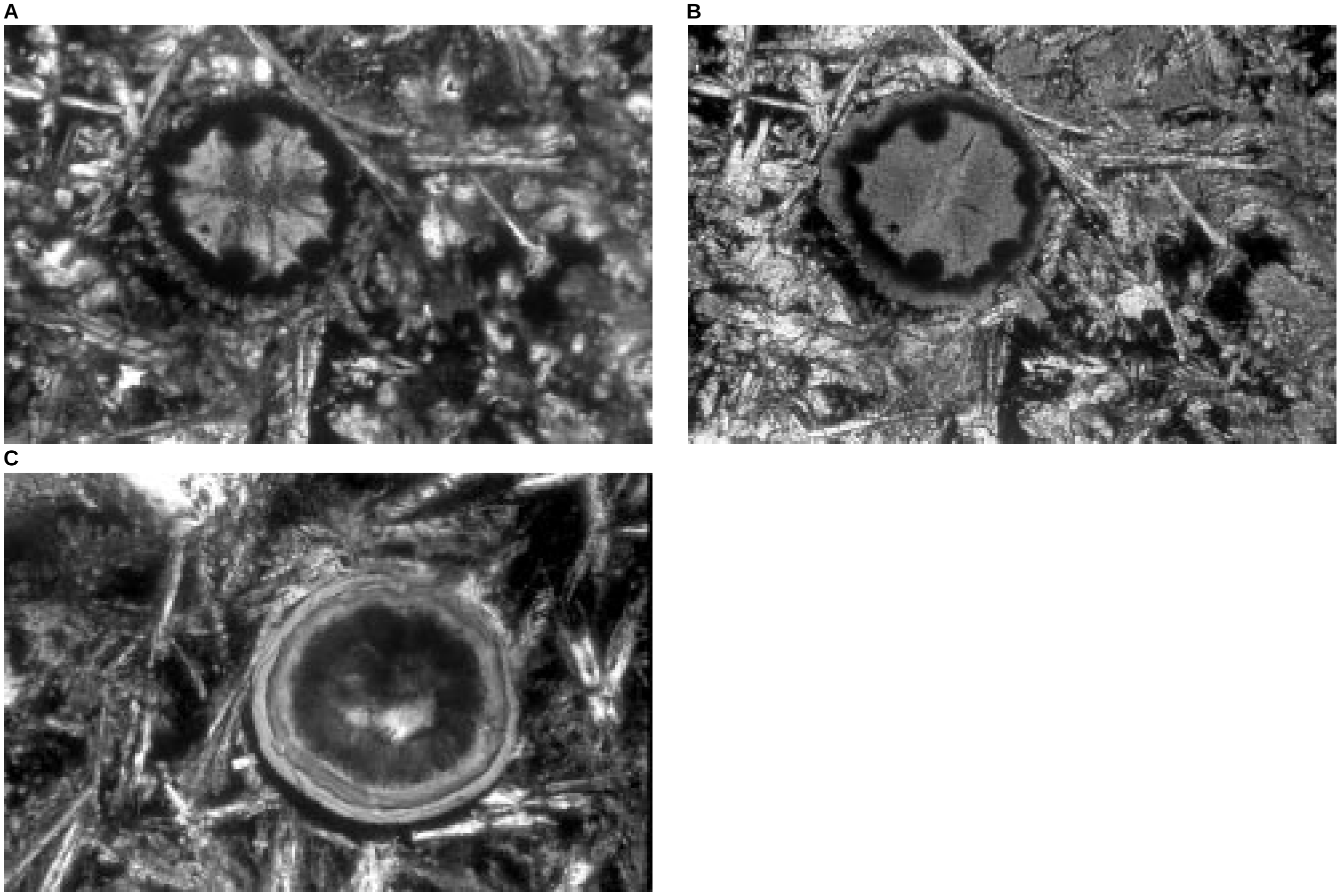

Figure 28. Photomicrographs of two celadonitic vesicle fills. **A.** An initial lining of celadonite is followed by iddingsite, then saponite, which completely fills the vesicle (Sample 168-1027C-5R-2 [Piece 2, 49−51 cm] in cross-polarized light). The vesicle is 0.26 mm across. **B.** Same field of view as in A in plane-polarized light. **C.** An initial lining of celadonite is followed by a lining of fine fibrous saponite, followed by an infilling of coarse fibrous saponite (Sample 168-1027C-5R-1 [Piece 8, 92−96 cm]) in plane-polarized light. The vesicle is 0.30 mm across.

nite, with veins and patches of zeolite constituting as much as 6% of the rock (by point counting). In thin section, glass shards commonly have saponite-replaced rims and fresh glass interiors. Separating the two is a thin layer of carbonate, identified optically as aragonite, that typically exhibits a single optical orientation (Fig. 35C, D).

Spatial Variations of Alteration Mineralogy and Style

Although all samples recovered from the Rough Basement sites exhibit alteration, there are several alteration features that vary systematically between the units and the sites. These include the distribution of oxidative and non-oxidative alteration styles and the distribution of carbonate alteration.

Oxidative alteration is defined as an overprint of secondary minerals that suggests the presence of an oxidative hydrothermal fluid. Such secondary minerals may occur either in veins, in vesicles, or as a replacement of magmatic phases. Iddingsite, which contains ferric iron in the form of poorly characterized $FeO(OH)_x$, and associated celadonite represent the chief signature of oxidative alteration. In contrast, saponite (which contains ferrous iron, predominantly) and associated sulfide minerals indicate a non-oxidative alteration style. At the Rough Basement sites, pillow basalts from Site 1026, as well as the pillow complex from Cores 168-1027C-3R through 5R, exhibit abundant oxidative alteration. In contrast, the diabase unit from Core 1027C-1R, as well as the massive basalts from Hole 1027B, does not exhibit significant oxidative alteration. Non-oxidative alteration is present in all cores.

In addition to heterogeneity in the distribution of oxidative alteration, the Rough Basement sites exhibit a systematic difference in the distribution of carbonate alteration. At Site 1027, abundant evidence exists for late-stage carbonate alteration in the form of calcite and aragonite in cross-cutting veins and filling vesicles. These features cut both the pillow complex and the diabase from Hole 1027C, as well as the massive basalts of Hole 1027B. The carbonate alteration affects lithologies that exhibit both the oxidative and non-oxidative alteration styles (Fig. 25). At Site 1026, carbonate is not a significant secondary phase. The two examples noted include the aragonite layer that forms on the inside of glass shards in the breccia of Unit 2 (Fig. 35C, D) and several small, vuggy calcite veins associated with iddingsite and hematite in Unit 1 of Hole 1026C. The differences between Site 1027 (major carbonate alteration) and Site 1026 (only minor carbonate alteration) may be a consequence of local hydrogeochemical factors influenced by differences in temperature or basement depth.

Discussion

All of the rocks recovered from the Rough Basement sites are basaltic and appear to represent normal, low-potassium tholeiites. No trace element data are available to engage in more detailed classifications. In addition, all of the samples have undergone significant hydrothermal alteration at relatively low temperature, probably less than 100°C and possibly much lower. There are however, important differences between certain units and groups of units from the Rough

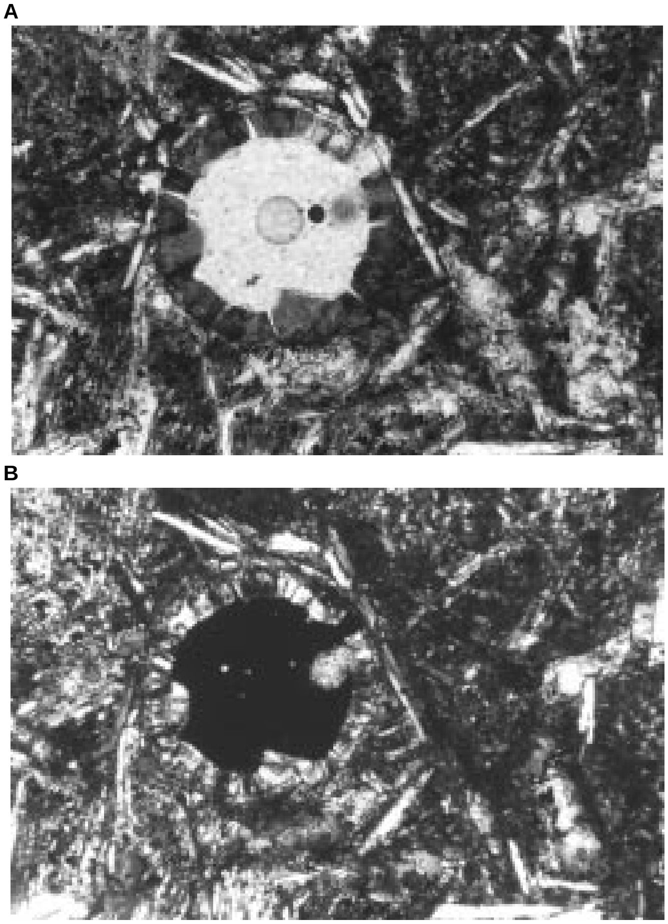

Figure 29. Photomicrographs in (**A**) plane-polarized light and (**B**) cross-polarized light of a vesicle lined by fibrous saponite (Sample 168-1027B-61X-CC, 25–28 cm). The vesicle is 0.28 mm across.

Basement sites. The major distinction is between the pillow basalts from Holes 1026B, 1026C, and 1027C and the diabase and massive basalts from Holes 1027B and 1027C. Three independent lines of evidence—geologic, geochemical, and alteration style—support the interpretation that the pillow basalt units represent basaltic basement, whereas the diabase and massive units represent off-axis volcanism.

The geologic evidence from the cored lithostratigraphy is that both the massive basalts of Hole 1027B and the diabase of Hole 1027C have pelagic sediments beneath them, which suggests either an off-axis intrusive or extrusive origin, or both. The geochemical evidence that distinguishes the pillow basalt units of Holes 1026B, 1026C, and 1027C from the diabase and massive basalts of Site 1027 is based upon major element analyses, which indicate that the variably fractionated pillow basalts define a coherent low-pressure fractionation trend, whereas the diabase and massive basalt are chemically similar to each other and lie off the pillow basalt trend (Fig. 36). The pillow trend is characterized by the following changes with decreasing Mg#: increasing TiO_2, Fe_2O_3, MnO, Na_2O, and P_2O_5 and decreasing Al_2O_3, MgO, and CaO. These trends can be explained in terms of fractionational crystallization of olivine (which reduces the Mg# and promotes iron enrichment) and plagioclase (reducing CaO and Al_2O_3), with or without clinopyroxene. Components that are incompatible with all these minerals become enriched with fractionation.

The final first-order distinction between the pillow basalts and the diabase/massive basalt is the alteration style. Low-temperature seafloor basalt alteration is often described in terms of two contrasting styles: oxidative and non-oxidative (Andrews, 1977; Laverne et al., 1996; Teagle et al., 1996). Iddingsite and celadonite, combined with the absence of sulfides, define the oxidative style, whereas saponite and sulfide minerals define the non-oxidative style. Most workers interpret the oxidative style of alteration as representing the effects of low-temperature alteration by massive volumes of relatively unaltered seawater that has access to the basalts while they are exposed at the seafloor. Some workers, however, suggest that an additional hydrothermal source of potassium and iron is necessary to form celadonite and iddingsite (e.g., Teagle et al., 1996). The non-oxidative alteration style is attributed to modified hydrothermal seawater that has lost much of its oxidizing potential. At the Rough Basement sites, oxidative alteration is present in the pillow basalts recovered from Holes 1026B, 1026C, and 1027C. These three pillow complexes, together with the interlayered basalt-hyaloclastite breccia from Hole 1026B, are therefore interpreted to have been exposed at the seafloor for a time period sufficient to allow the oxidative alteration to form. Furthermore, all three pillow complexes probably represent sites of considerable past throughput of oxidative seawaterlike fluid, such as might occur within a seafloor hydrothermal recharge area.

In contrast to the pillow basalt units, the diabase and the massive basalts from Holes 1027C and 1027B have very little to no oxidative alteration. This suggests that these units may never have been exposed at the seafloor. Formation of these units either as dikes and/or sills, or as flows over low-permeability sediments, could result in a hydrogeologic setting where voluminous fresh seawater supply was not possible.

AGE PROFILES

Calcareous Nannofossils

Nannofossils are common to abundant in hemipelagic mud layers of Sites 1026 and 1027 but very rare or absent in turbidite beds. Nannofossils are well preserved (with slight dissolution) through the sediment section at Site 1026 and in the upper part of the section (above 280 mbsf) at Site 1027. However, a strong overgrowth of nannofossils is common in the lower part of the section at Site 1027 (below 280 mbsf), and nannofossils are preserved as calcareous debris in a number of samples, probably because of hydrothermal alteration. Nannofossil age assignments are based mainly on samples in which nannofossils are well preserved.

Late Cenozoic nannofossil assemblages were found in sediments of these sites (Table 15). Age assignments were difficult because of the high latitude of the area and the turbiditic nature and hydrothermal alteration of the sediment. Nannofossil species found in this area are mainly cold-water forms (e.g., *Gephyrocapsa caribbeanica*) or cosmopolitan forms (e.g., *Emiliania huxleyi*); all of their datums are useful for this leg. A few temperate-water forms (e.g., *Reticulofenestra asanoi* and *Helicosphaera sellii*) are infrequent in hemipelagic layers, leading to difficulty in determining specific datums. Additional samples were collected to determine the datums of these species. However, the top of *R. asanoi* was not recognized at Site 1027 because nannofossils from these sediments are strongly overgrown and poorly preserved below 280 mbsf. In addition, *Calcidiscus macintyrei* occurs frequently and in a remarkable abundance in samples below the base of *G. caribbeanica*, making it difficult to distinguish the last occurrence of this species from its presence caused by reworking. In this case, the top of *C. macintyrei* was identified based on recognition of the top of *H. sellii.* The Pliocene genus *Discoaster* prefers warm waters and is absent in this area; hence it is impossible to make a biostratigraphic subdivision of sediments below Core 168-1027B-48X. The nannofossil assemblage below Core 168-1027B-52X is characterized by the dominance of small to medium-sized *Reticulofenestra* species (e.g., *Reticulofenestra minuta* and *Reticulofenestra minutula*) and by the absence of *Reticulofenestra pseudoumbili-*

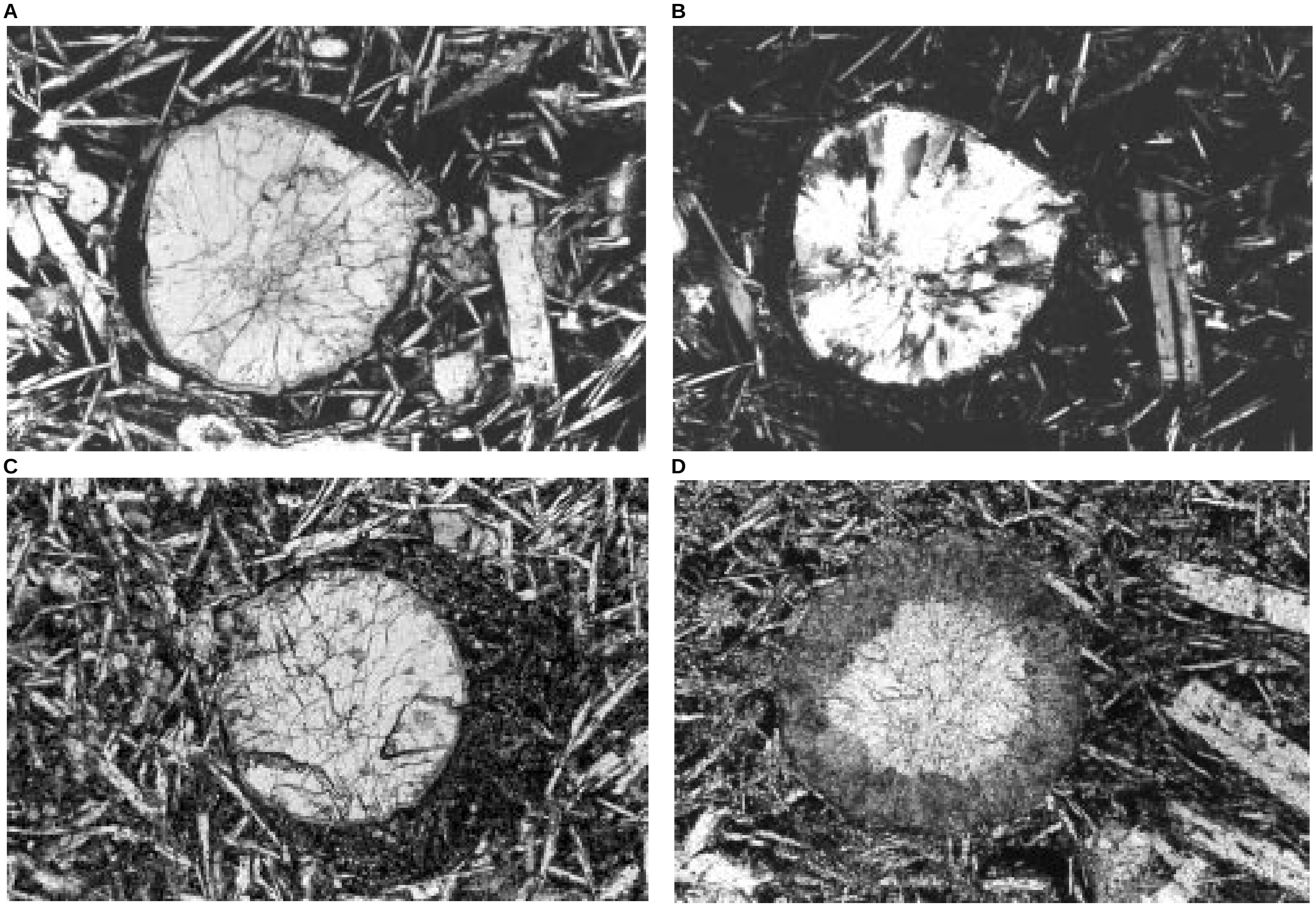

Figure 30. Photomicrographs of carbonate amygdules. **A.** Amygdule from Sample 168-1027B-60X-CC (Piece 5) (sketched in Fig. 27A) in plane-polarized light, showing partial infill by cryptocrystalline magmatic segregation material, followed by an isopachous rim of fibrous saponite plus pyrite, followed by sparry radial calcite. The vesicle is 0.6 mm across. **B.** Same field of view as in A in cross-polarized light. **C.** A segregation vesicle from Sample 168-1027B-61X-CC, 25–28 cm, in plane-polarized light. The vesicle is partially filled by a meniscus of cryptocrystalline magmatic material, which is, in turn, followed by a thin layer of fibrous saponite and a complete infill by calcite. The vesicle is 0.73 mm across. **D.** An atypical vesicle from Sample 168-1027B-62X-CC, 39–42 cm, in plane-polarized light. The vesicle is filled by two distinct layers of carbonate, the first of which is cloudy, with the final infill being clear and sparry. The vesicle is 0.33 mm across.

cus, indicating an age of late Pliocene for the sediments below this core. The absence of *R. pseudoumbilicus* within sediments of Site 1027 suggests an age of the basal sediment younger than 3.6 Ma.

Figure 37 shows age/depth plots of nannofossil and basement ages estimated from sea-surface magnetic anomalies for these two sites. At Site 1027, sedimentation seems to have started soon after basement formation, and at Site 1026 there is a hiatus for several thousand years.

Magnetostratigraphy

Because of the problems during the cruise with the new cryogenic magnetometer (see "Methods" chapter, this volume), the sediment magnetic stratigraphy for Sites 1026 and 1027 was not completed in time for this volume. However, the complete, reduced data set resides in the ODP database and is available on request.

FLUID GEOCHEMISTRY

Introduction

Ninety-nine squeezed pore-water and two borehole water samples were collected from Sites 1026 and 1027. Site 1026 is located on a buried basement ridge between two basement outcrops (Mama and Baby Bare) with a depth to basement of 247.1 and 228.9 mbsf in Holes 1026B and 1026C, respectively. Site 1027, which is 2.2 km east-southeast of Site 1026, is located over a basement trough where the basement depth is 613.8 mbsf. This trough separates two ridges: the ridge on which Mama and Baby Bare are located and an eastern ridge on which the Papa Bare basement outcrop is located. These two sites are conceptually similar to Ocean Drilling Program (ODP) Sites 677 and 678, which were drilled on 6-m.y.-old crust on the southern flank of the Costa Rica Rift. Site 678 (equivalent to Site 1026) was drilled on a basement ridge where pore waters upwell at 1–2 mm/yr through the 172-m-thick sediment section (Mottl, 1989), and Site 677 (equivalent to Site 1027) was drilled in the adjacent basement trough. Pore waters downwell through the 309-m-thick sediment section at Site 677. Temperatures at the sediment/basement interface are similar and range from 58° to 66°C at all four sites (see "Thermal Studies," section, this chapter; Fisher et al., 1990).

Chemical profiles in the pore waters generally follow similar trends at both Sites 1026 and 1027 (Table 16; Figs. 38–40). These profiles result from reactions with sediment (e.g., bacterial degradation of organic matter and diagenesis of clay), flow of altered seawater through basaltic crust, water/rock reactions in basement, and temporal variations in the composition of bottom water from glacial to interglacial periods.

In contrast to Sites 677 and 678 on the Costa Rica Rift flank, there is no substantial evidence from the pore-water profiles for fluid flow through the sediment at the Leg 168 sites. However, on return to Hole

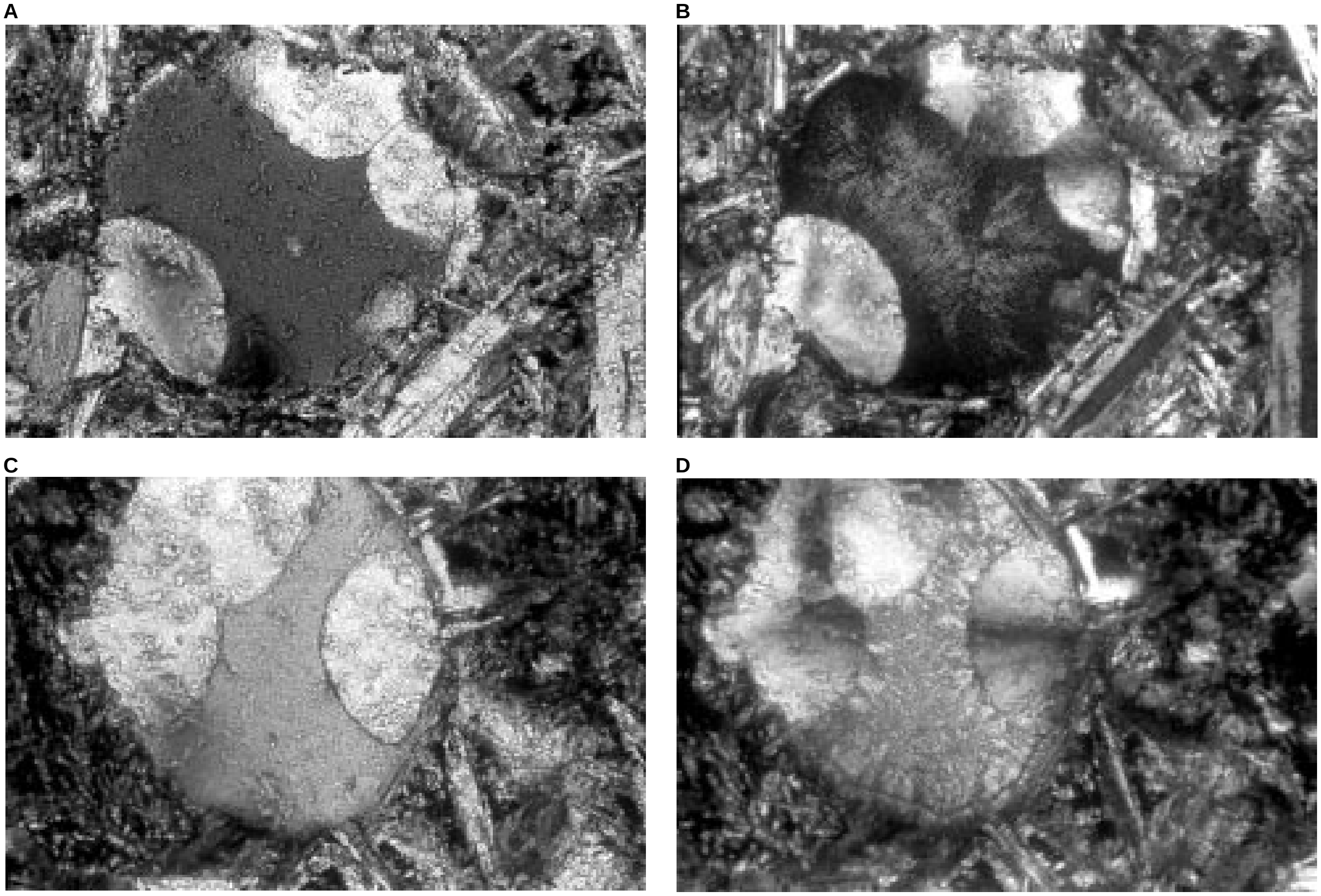

Figure 31. Vesicles filled by clay and carbonate. **A.** Radial carbonates and celadonite fill a vesicle in an alteration halo (Sample 168-1027C-5R-2 [Piece 2, 49–51 cm]) in plane-polarized light. The vesicle is 0.4 mm across. **B.** Same field of view as in A in cross-polarized light. **C.** Radial carbonates with saponite filling a vesicle (Sample 168-1027C-5R-2 [Piece 2, 49–51 cm]) in plane-polarized light. The vesicle is 0.4 mm across. **D.** Same field of view as in C in cross- polarized light.

1026B, basement waters were found to be upwelling through the cased portion of the sediment section. These fluids, which originate from basement at 247 to 262 mbsf, were collected using the WSTP and are the first true basement waters collected from a Deep Sea Drilling Project or ODP drill hole (Table 16; Figs. 38–40). The basement end-member compositions of altered waters from Hole 1026B and from the springs (M. Mottl, unpubl. data) Baby Bare are included in Figures 38 through 40 for comparison.

Bacterial Reduction of Organic Matter and Inorganic Diagenesis

Bacteria reduce organic matter using a series of oxidants. Dissolved oxygen and nitrate are the first oxidants to be consumed, releasing phosphate to pore waters. Phosphate also is released during sulfate reduction of organic matter when alkalinity and ammonia are also generated. As at the Hydrothermal Transition sites, these increases are observed only in the upper portion of the sediment section (Figs. 38–40). In the lower section, bacteria-mediated sulfate reduction also occurs, but there are no measured increases in phosphate or alkalinity. This is because inorganic reactions take place faster than the rate at which sulfate is reduced. Ammonia production may also occur in this lower section, but inorganic reactions clearly predominate. The reactions that remove phosphate, alkalinity, and ammonia from pore waters can include adsorption onto oxides, carbonate formation, and reaction with clays.

Several of these inorganic reactions may be inferred from changes in other pore-water species. For example, the decrease in the concentration of calcium from the bottom seawater value results from the precipitation of carbonates. Deeper in the sediment section, concentrations of calcium increase because of reaction in the sediment column. However, calcium concentrations must decrease near the base of the sediment section as the basement fluid (WSTP) samples contain less calcium than the deepest pore waters sampled.

Several of the other cations (magnesium, sodium, and potassium) also show signs of reaction in the sediment section. Uptake of dissolved magnesium by sediments was inferred in cores from two of the Hydrothermal Transition sites. A deflection in the Mg pore-water profile at 175 mbsf at Site 1026 (Fig. 39) suggests that uptake is similarly occurring, but results are inconclusive for Site 1027. In contrast, concentrations of magnesium in pore waters of samples from within the upper 50 mbsf at Site 1027 are higher than in bottom seawater. Thus, in the upper sections at this site, magnesium is released to pore waters, probably from ion-exchange reactions with clays. Such an anomaly may be lacking at Site 1026 because of its eradication by diffusion with low-Mg waters within and near basaltic basement.

Concentration profiles of sodium and potassium, like calcium, show evidence for inorganic reaction in the lower part of the sediment column. It appears that the sediments are both a source and sink for sodium and potassium. The sharp decrease in concentration in the lowermost pore waters (Fig. 39) suggests that the sediment provides a sink for sodium (by exchange for calcium) just above basement because the underlying basement fluid has a much higher sodium concentration. Unless this sodium uptake began recently, this behavior also requires a source of sodium, at a depth of about 150 mbsf at Site

Table 14. Comparison of vein data from the Costa Rica Rift, Hole 896A, with data from Hole 1027C.

Type	Number in Hole 896A (27% recovery)	Total (%)	Number in Hole 1027C (64% recovery)	Total (%)
Clays	1209	60.7	19	25.7
Clays + carbonates	467	23.4	36	48.6
Clays + iddingsite ± carbonates	218	10.9	4	5.4
Carbonates	99	5	15	20.3
Totals	1993	100	74	100

Note: Hole 896A data from Alt, Kinoshita, Stokking, et al. (1993).

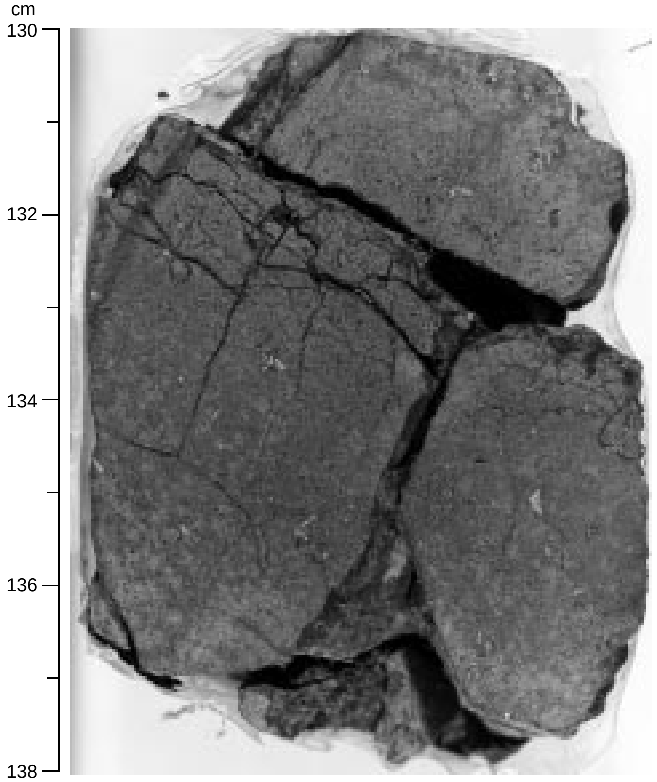

Figure 32. Close-up photograph of a pillow basalt fragment (Sample 168-1027C-5R-5 [Piece 12, 130–138 cm]) with a network of green clay veins.

1026 and 500 mbsf at Site 1027, to maintain the steep concentration gradient. Alternatively, a transient process may have occurred in basement within the past 10 k.y. (given that the deepest pore-water samples are within 10 m of the present-day basement composition defined by waters from the WSTP). This transient water would be more evolved than the pore fluids in the overlying sediments. However, only calcium and sodium are affected, and one would expect to observe anomalies in other dissolved chemical species as well. Therefore, the explanation that the sodium profiles result from reaction in the sediment section seems more likely. Moreover, calcium-sodium exchange has been observed at other sites drilled near basement (e.g., Sites 677 and 678, Mottl, 1989). It is noteworthy that the sill encountered at 576–591 mbsf in Hole 1027C does not appear to interrupt the trends established in the sediment above it. Profiles of virtually all dissolved species extrapolate smoothly across this interval, suggesting that the sill is no more reactive than the sediments above and below it.

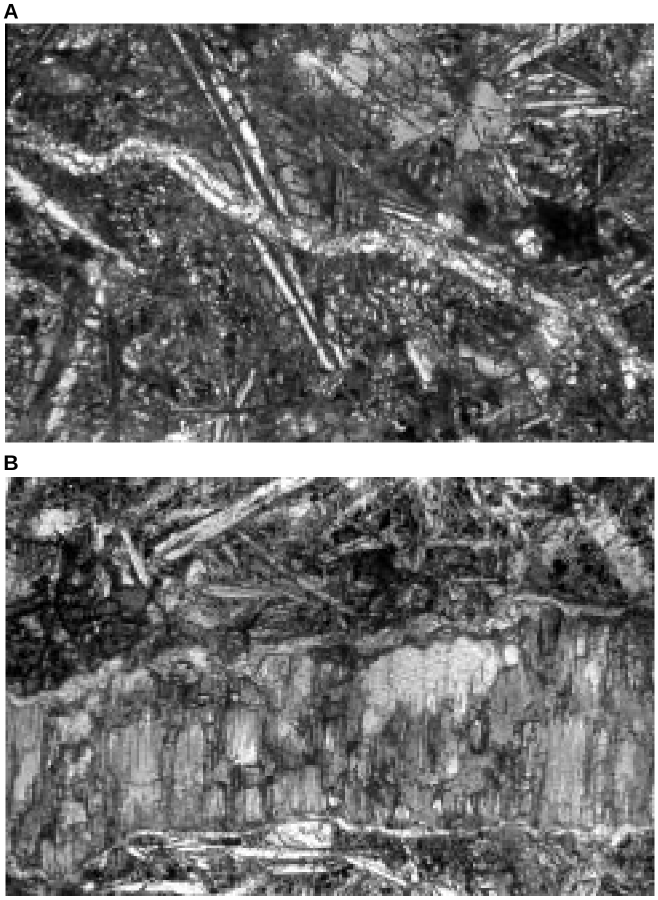

Figure 33. Photomicrographs of veins. **A.** Saponite vein, 25 µm across, cutting an aphanitic microcrystalline basalt (Sample 168-1027B-62X-CC, 7–10 cm) in cross-polarized light. **B.** Fibrous calcite-clay vein, 0.45 mm wide, cutting diabase (Sample 168-1027C-1R-6 [Piece 2, 67–70 cm] in plane-polarized light.

Potassium, like sodium, reacts with the sediment in two depth ranges at both sites. Potassium is taken up in the lower part of the sediment column (the lower half at Site 1027), where the lowest concentrations of 1.0–1.8 mmol/kg are reached that may represent equilibrium for the given lithology and temperature. The release of potassium from the sediment occurs above this zone at about 280 mbsf at Site 1027 and possibly at 90 mbsf at Site 1026. The increase in concentration at the base of the sediment section is consistent with diffusional contact with altered seawater in basement having a greater potassium concentration than that in the lowermost sediment sections.

Dissolved silica is highly reactive in the sediment section (Fig. 40). Concentrations are high in the upper section and decrease abruptly at about 150 mbsf at Site 1026 and 290 mbsf at Site 1027, consistent with a change in equilibrium from amorphous silica to chalcedony (Wheat and Tribble, 1994). Concentrations generally decrease with depth below this sharp concentration boundary, whereas an increase would be expected because of the increase in temperature. This behavior may reflect sluggish reaction coupled with diffusive interaction with low-Si fluids in basement.

Unlike dissolved silica, chlorinity remains unreactive in the sediment section. Changes in concentration reflect glacial-interglacial changes in the concentration of bottom seawater, rates of sediment

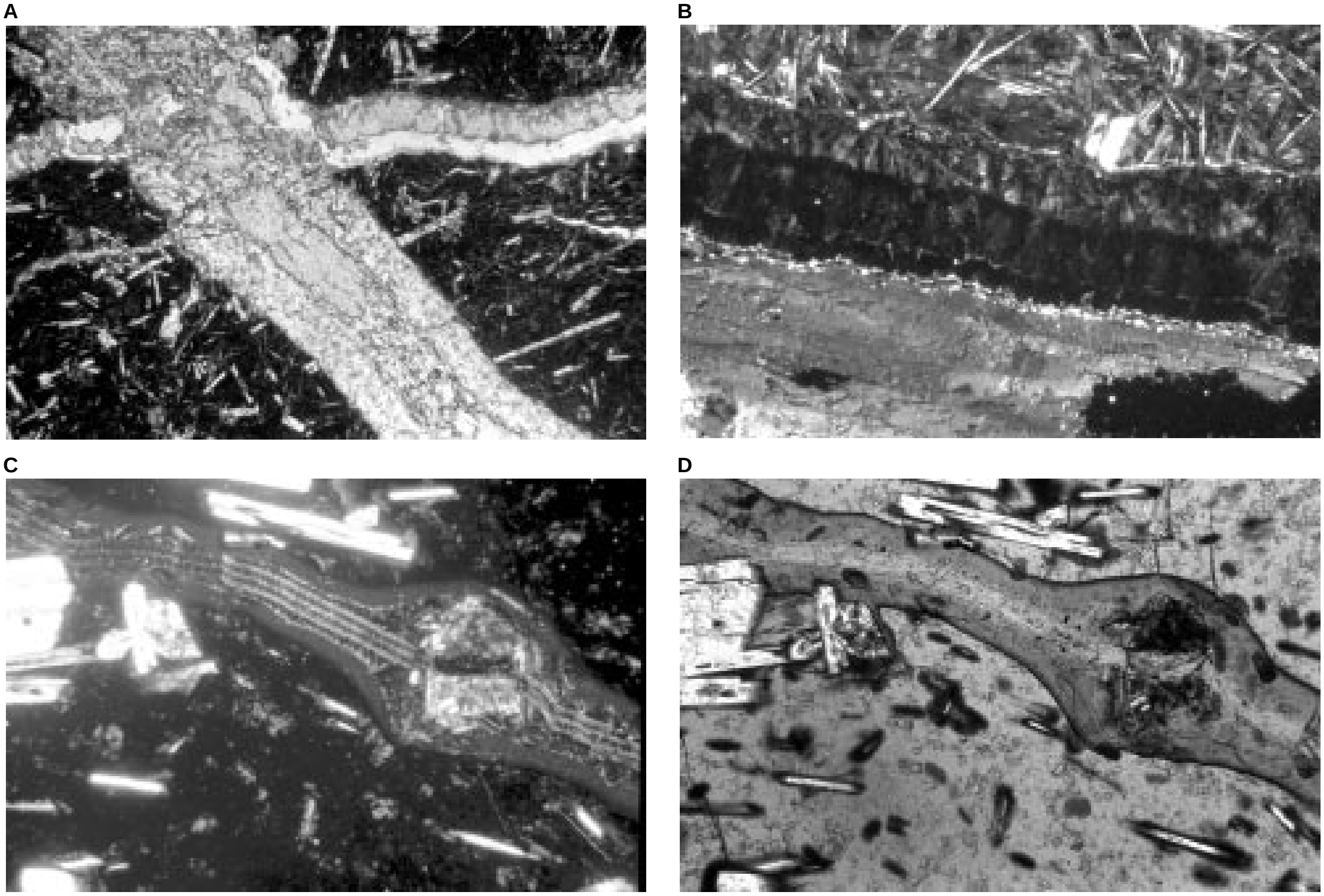

Figure 34. Photomicrographs of veins with zeolites. **A.** Clay-zeolite-calcite vein cutting an aphanitic microcrystalline basalt (Sample 168-1027C-4R-2 [Piece 9C, 85–89 cm]) in plane-polarized light. The vein has a thin clay edge, followed by zeolite (clear), and is then completely filled by calcite (slightly cloudy). Field of view = 5.6 mm. **B.** Detail of the same vein as in A in cross-polarized light. The central calcite is bright, whereas the flanking zeolite has low birefringence and has a layered structure (consisting of an outer radial-fibrous layer and an inner columnar layer). Field of view = 1.4 mm. **C.** A zeolite veinlet cuts fresh glass in a pillow basalt rim (Sample 168-1027C-5R-2 [Piece 1A, 1–9 cm]) in cross-polarized light. The zeolite crystals form a layered structure. An olivine microphenocryst is cut by the veinlet and completely altered to saponite. A zone of glass alteration extends outward from the veinlet. Field of view = 1.4 mm across. **D.** The same field of view as in C in plane-polarized light. Note the olivine and glass alteration in contrast to the lack of alteration of a plagioclase microphenocryst.

deposition, and communication with seawater in basement that has a higher chlorinity than recent bottom seawater.

Fluid Flow and Reaction in Basement

There is no evidence from the chemical profiles for vertical flow of pore water through the sediment column at Sites 1026 and 1027. However, on our return to Hole 1026B to set the CORK we found from a temperature log that water from 256 ± 7 mbsf in basement was flowing up the casing. We sampled this 63.8°C water twice from the open borehole using the WSTP. It contained higher than expected dissolved silica, indicating that it probably encountered drilling mud on its path to the sampler. In most other respects, this basement water is similar to the 25°C springs on the Baby Bare outcrop and to the water from several short sediment pore-water profiles from areas of focused upwelling near Mama Bare outcrop, both sampled using the manned submersible *Alvin* in 1995 (M. Mottl, unpubl. data). The basement water from Hole 1026B is also similar to the basal sediment pore water from Sites 1026 and 1027. This similarity is especially close if the sediment pore-water profiles from Holes 1026A and 1026C are extrapolated to 256 mbsf, the depth in basement from which the water sampled by the WSTP apparently originated (Figs. 38–40). All of these similarities taken together imply that the water circulating through basement in the vicinity of the Rough Basement sites is relatively uniform in composition.The long extrapolations in composition required for sulfate and especially potassium at Site 1026 to match the WSTP samples at 256 mbsf (Figs. 38–40) suggest that transport within the upper 9 ± 7 m of basement may be mainly by diffusion and that the top of the presumed high-permeability zone in basement may be 9 ± 7 m below the sediment/basement interface.

Besides potassium and sulfate, there are two other elements that have different concentrations in the Hole 1026B basement water than compared to the basal sediment pore water from Holes 1026A and 1026C: sodium and calcium. These two elements exhibit small reversals within the 22 m of highly altered sediment sandwiched between the sill at 585–592 mbsf in Hole 1027C and basement at 614 mbsf that, if extrapolated to 256 mbsf where the basement water originated, nearly match the basement water composition. These reversals in concentration imply that the pore water reacts with the basal sediment, which takes up sodium and supplies calcium to solution, as discussed above. Because the reversals are small, the extrapolations are

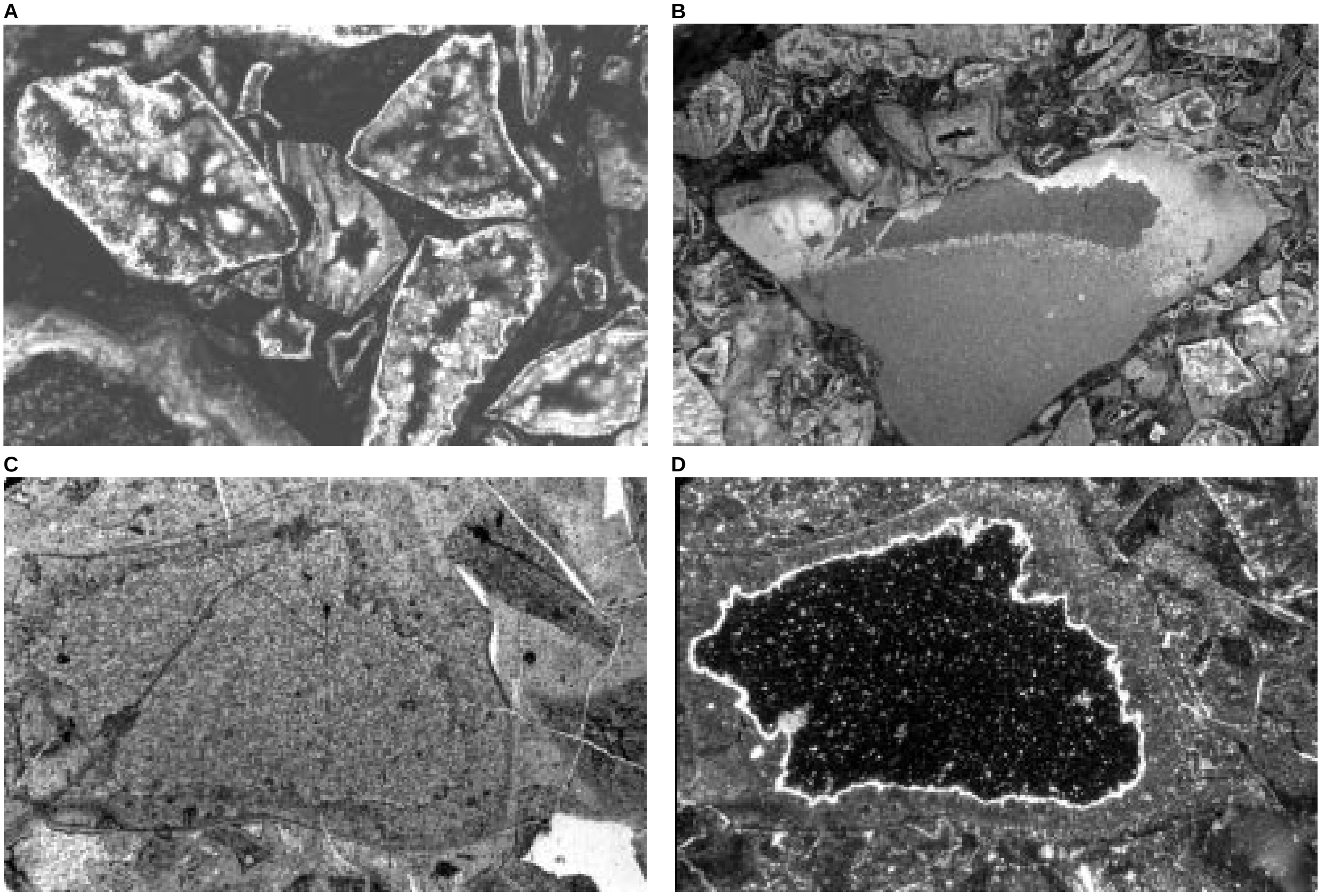

Figure 35. Basalt-hyaloclastite breccia (Sample 168-1026B-3R [Piece 4]). **A.** Photomicrograph of a rock slab with incident illumination showing altered glass clasts totally replaced by green and white clays. Field of view = 0.28 mm wide. **B.** Photomicrograph of a rock slab showing altered basalt fragments and glass clasts from the same sample as in A. Field of view = 0.9 mm. **C.** Photomicrograph of a partially altered glass shard in the basalt-hyaloclastite breccia (Sample 168-1026B-3R-1 [Piece 8, 59–62 cm]) in transmitted plane-polarized light. Field of view = 5.58 mm. **D.** Same field as in C in cross-polarized light. Note the thin layer of optically continuous aragonite separating the fresh glass inside from the saponite replacement rim.

highly uncertain, but they are consistent with similar extrapolations for sulfate, potassium, and other species.

The altered seawater in basement at the Rough Basement sites displays the same net directions of elemental transport between basalt and seawater as do the inferred basement waters at the Hydrothermal Transition Transect, but to a greater extent. This highly altered basement water is also quite similar to the basement water at Sites 677 and 678 on the southern flank of the Costa Rica Rift (Mottl, 1989). Even though these two ridge-flank areas have different sediment types, sedimentation rates, crustal ages, and heat flow, they have similar basement temperatures and formation-water compositions.

Conclusions

The composition of the waters from basement at Site 1026 are similar to those in springs at Baby Bare, in zones of focused diffuse upflow at Mama Bare, and as extrapolated from pore waters from Sites 677 and 678 on the southern flank of the Costa Rica Rift. In addition, these basement waters are similar (by most chemical species) to those determined from extrapolation of gradients in pore-water data for most chemical species at Sites 1026 and 1027. The major exceptions are calcium and sodium, both of which are believed to be involved with ion-exchange reactions in the basal sediments, an interpretation that is consistent with results from other ODP sites.

ORGANIC GEOCHEMISTRY

Volatile Hydrocarbons

Results from headspace gas analyses are listed in Table 17 and illustrated in Figure 41. The methane concentration profile at Site 1026 is characterized by a sharp rise at 50–60 mbsf to a maximum near 100 mbsf. Below this depth, methane decreases rapidly and remains low with increasing depth. In samples from Hole 1027B, methane concentrations increase abruptly below 150 mbsf to a relatively constant value. Concentrations decrease abruptly again near the bottom of the hole. The two headspace samples taken in the sediment recovered from between the diabase sill and basement in Hole 1027C contained only minor amounts of methane. Higher molecular weight hydrocarbon gases are absent in samples from Hole 1027B down to 200 mbsf, where minor amounts of ethane and propane appear. The total amount of higher molecular weight hydrocarbon gases increases stepwise with depth to a maximum value at 450 mbsf. The cores in which the higher hydrocarbons were found also possessed a marked petroliferous odor. Methane varies inversely with dissolved sulfate concentration at Sites 1026 and 1027 (see “Inorganic Geochemistry” section, this chapter). The highest methane concentrations occur within the interval where sulfate is completely exhausted. This relationship indicates that the methane results from bacterial production.

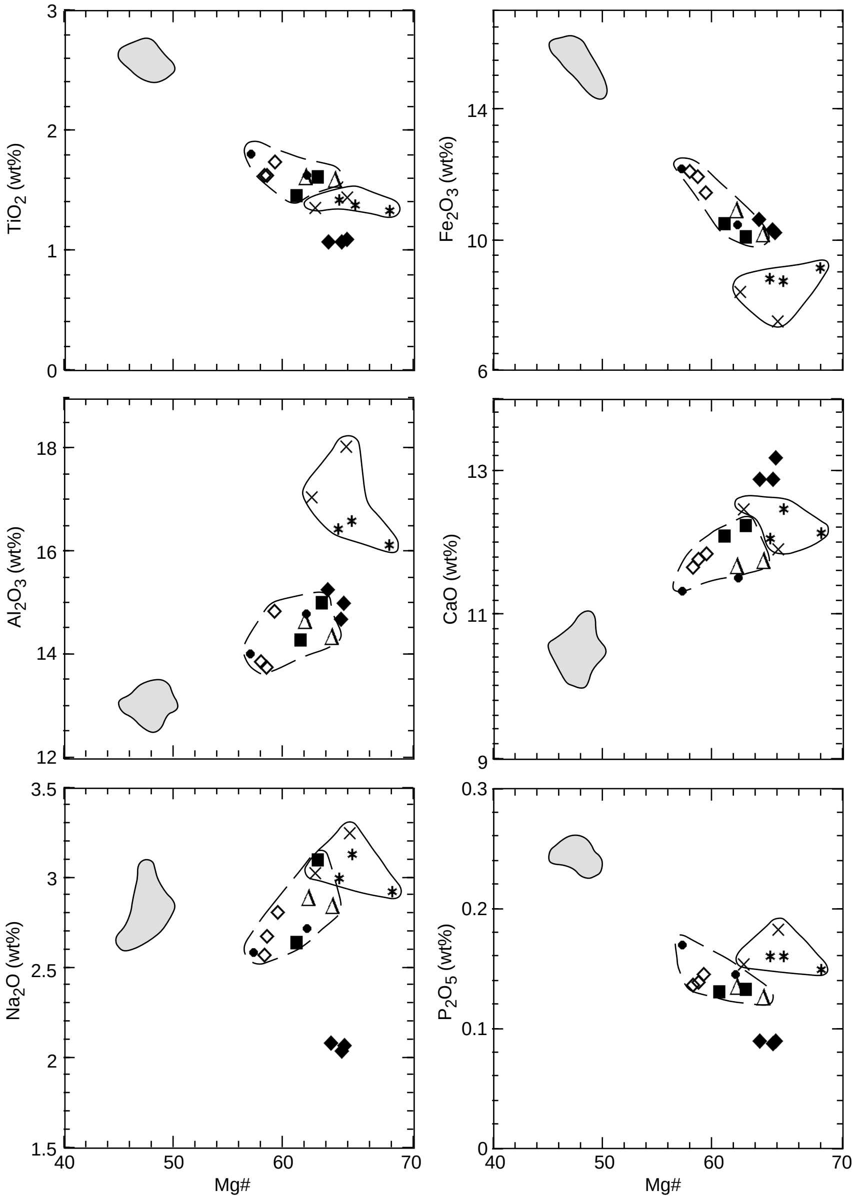

Figure 36. Selected basalt chemical data plotted against Mg#. The data enclosed by solid lines represent diabase from Hole 1027C and massive basalt from Hole 1027B. These are all chemically distinct from pillow basalts from Site 1024, Hole 1026B, Hole 1026C, and Cores 168-1027C-3R and 4R (enclosed by dashed lines). Pillow basalts from Core 168-1027C-5R are also distinct and may represent the least-fractionated pillow basalts. The ferrobasalt fields (shaded) from Site 1025 are shown for comparison. Solid squares = Holes 1024B and 1024C; solid circles = Hole 1026B; triangles = Hole 1026C; × symbols = Hole 1027B; asterisks = Core 168-1027C-1R; open diamonds = Cores 168-1027C-3R and 4R; and solid diamonds = Core 168-1027C-5R.

Methanogenic bacteria usually become active only after dissolved sulfate is almost completely depleted, as occurs in sediment from 166–533 mbsf in Hole 1027B. Similarly, in Hole 1026A, little methane is produced until the dissolved sulfate concentration drops below 1–2 mmol/kg, which is close to the threshold value of 0.5 mmol/kg sulfate generally thought necessary for the accumulation of methane (Whiticar et al., 1994). Methane that diffuses out from the methane production zone is oxidized, maintaining low methane levels in zones without active methanogenesis. There is no apparent correlation between total organic carbon (TOC) and methane in zones of methanogenesis at Sites 1026 and 1027. Figure 41 also shows the C_1/C_2 (methane/ethane) ratio profile for Hole 1027B. Bacterial processes can only form trace amounts of higher molecular weight hydrocarbons (Tissot and Welte, 1984); the negative correlation between headspace methane and ethane indicates that the higher molecular weight hydrocarbon gases are thermogenically produced in situ.

Organic Carbon

The sediments cored at Sites 1026 and 1027 have relatively low organic carbon content (Table 18 on CD-ROM, back pocket; Fig. 42). At both sites, the highest concentrations are found in sediment from near the seafloor. TOC concentrations decrease within the top 100 m then increase abruptly and remain nearly constant to the bottom of the holes.

Sulfur, Nitrogen, and Hydrogen

The results of total sulfur, nitrogen, and hydrogen analyses are listed in Table 18 on CD-ROM (back pocket). The total sulfur content of the sediment cored at Sites 1026 and 1027 is generally low. In most samples, the NCHS analyzer was not able to detect any sulfur. The sulfur data for Sites 1026 and 1027 only represent rough estimates and should be treated with caution because the NCHS analyzer was unable to measure sulfur with acceptable precision and reproducibility during Leg 168. Total nitrogen and hydrogen have depth trends similar to TOC. Within the top 200 m, the concentration profiles of organic carbon, nitrogen, and hydrogen vary sympathetically (Fig. 42). Below 200 mbsf this correlation becomes less distinct, but the general trend of relatively constant concentrations continues to the bottom of the hole. A comparison between the concentration profiles of total nitrogen and dissolved ammonium (see "Inorganic Geochem-

Table 15. Stratigraphic list of calcareous nannofossil events for Rough Basement Sites 1026 and 1027.

Nannofossil event	Site 1026 Hole, core, section, interval (cm)	Site 1026 Depth (mbsf)	Site 1027 Hole, core, section, interval (cm)	Site 1027 Depth (mbsf)	Age (Ma)
B acme *E. huxleyi*	1026A-4H-1, 75	25.15	1027B-5H-3, 60	36.30	0.09
T *G. caribbeanica*	1026A-8H-2, 124	65.14	1027B-9H-1, 82	71.52	0.22
B *E. huxleyi*	1026C-3R-CC, 20	104.28	1027B-17X-3, 51	149.01	0.28
T *P. lacunosa*	1026C-5R-CC, 7	124.93	1027B-22X-4, 88	198.88	0.46
B *G. caribbeanica*	1026C-12R-2, 68	192.68	1027B-28X-2, 30	253.10	0.76
T *R. asanoi*	1026C-14R-1, 132	211.02			0.90
B *R. asanoi*	1026C-14R-CC, 13	217.65	1027B-39X-5, 25	363.55	1.15
T *H. sellii*	1026C-15R-6, 150	228.30	1027B-46X-4, 52	429.62	1.55
T *C. macintyrei*	1026C-15R-CC, 14	229.07	1027B-47X-1, 8	434.28	1.58
B *G. lumina*			1027B-48X-2, 42	445.82	1.68

Note: B = bottom, and T = top.

istry" section, this chapter) shows that the decrease in dissolved ammonium with depth below 300 mbsf in Hole 1027B does not correspond to an observable increase in sedimentary nitrogen content. This means either that the ammonium decrease results from diffusion into basement or that the incorporation of ammonium nitrogen into diagenetic mineral phases is minor compared to the total nitrogen content of the sediment.

Organic Matter Type:
C/N Ratios and Rock-Eval Pyrolysis

Calculated C/N ratios fluctuate about a value of 7.3 at Site 1027 and about 14.3 at Site 1026, which is indicative of a predominantly marine origin for the organic matter at Site 1027 and a mixed marine/terrigenous origin at Site 1026. A positive correlation between TOC and C/N ratio (Fig. 43) at Site 1027 indicates that enhanced TOC values likely resulted from an episodic supply of terrigenous organic matter. Seventeen samples were analyzed on the Rock-Eval instrument (Table 19). In Figure 44, the hydrogen index is plotted against the oxygen index in a variation of a van Krevelen diagram (Espitalié et al., 1977). The majority of the data points fall in the region of a type III kerogen, indicating that the organic matter is derived from higher plants and/or seagrass (Tissot and Welte, 1984).

PHYSICAL PROPERTIES

Sediment Properties

Physical properties were measured continuously with the multisensor track (MST) and on discrete samples from the cores recovered from Sites 1026 and 1027. A summary of results for each hole is presented in Figure 45. Based on the visual core descriptions, the data for Holes 1026A, 1026B, 1026C, 1027B, and 1027C were separated into mud, sand, diabase, pillow basalt, and hyaloclastite lithotypes. Criteria for distinguishing between mud and sand for the sedimentary layers are described in the "Methods" chapter (this volume). Table 20 lists the average, standard deviation, and number of measurements included in each category.

To assess a possible sampling bias, the total thickness of recovered sand relative to the thickness of the recovered sediment section was compared to the number of measurements in sand relative to the total number of measurements in sediment (Table 21). Thermal conductivity, index properties (IP), and digital sonic velocimeter (DSV) measurements are biased toward an oversampling of the mud layers, indicating that a weighted mean, rather than a simple mean, may better characterize average conditions throughout the drilled interval. Furthermore, because the section of low recovery in Hole 1027B (87–250 mbsf) likely consists of thick sand units, the degree of bias in the measurements in that interval may be underestimated.

Multisensor Track Measurements

Gamma-ray attenuation porosity evaluator (GRAPE) bulk densities are shown without the corrections suggested by Boyce (1976) (see discussion in "Physical Properties" section, "Hydrothermal Transition Transect" chapter, this volume) and thus are greater than IP bulk densities by as much as 15% in the higher porosity sediments. As illustrated in Figure 45, this offset is less for the deeper, lower porosity material.

An anomalous, relatively homogeneous, fine-grained layer about 5 m thick was encountered between 70 and 75 mbsf in Hole 1026A. Figure 46 compares MST data and IP porosity measurements in this interval. The correlation between GRAPE bulk density and IP porosity is clear at this fine scale. Natural gamma-ray (NGR) values increase dramatically in this section (see Fig. 45).

When MST data for Holes 1026A and 1027B are compared, direct hole-to-hole correlation is evident only in the upper 3 mbsf. This correlation is shown for magnetic susceptibility (MS) data in Figure 47 but exists for GRAPE bulk density as well. Below 3 mbsf, no correlations are evident.

Index Properties

The porosity data for the sediments from Sites 1026 and 1027 are plotted together in Figure 48. Porosity in mud decreases from >80% at the seafloor to about 55% around 80 mbsf. This trend is not seen in the sand layers. Between 100 and 300 mbsf, porosity shows little variation with depth. Below 300 mbsf, including the sedimentary rock of Hole 1027C, porosity decreases consistently with depth to about 40% at 600 mbsf. Lower porosity values found at 258 and 476 mbsf are thin layers of highly lithified mud and calcareous mudstone, respectively (Table 22 on CD-ROM, back pocket).

DSV P-12wave Velocity

The empirical relationship between *P*-wave velocity and porosity can be used to generate two-dimensional pseudo-porosity profiles from seismic data. A plot of IP porosities vs. DSV velocities from the sediments of both the Hydrothermal Transition and Rough Basement sites is shown in Figure 49 with curves derived from laboratory measurements from the Labrador Sea cores from Leg 105 (Shipboard Scientific Party, 1987) and borehole logging measurements from Leg 146 in Cascadia Basin (Shipboard Scientific Party, 1994). In unfractured sediment, it is generally expected that laboratory porosities will be higher and velocities lower than borehole values because of core expansion and rebound effects. Nevertheless, it appears that although the two curves parallel the behavior we observed, Leg 168 velocities are consistently lower than predicted with either curve.

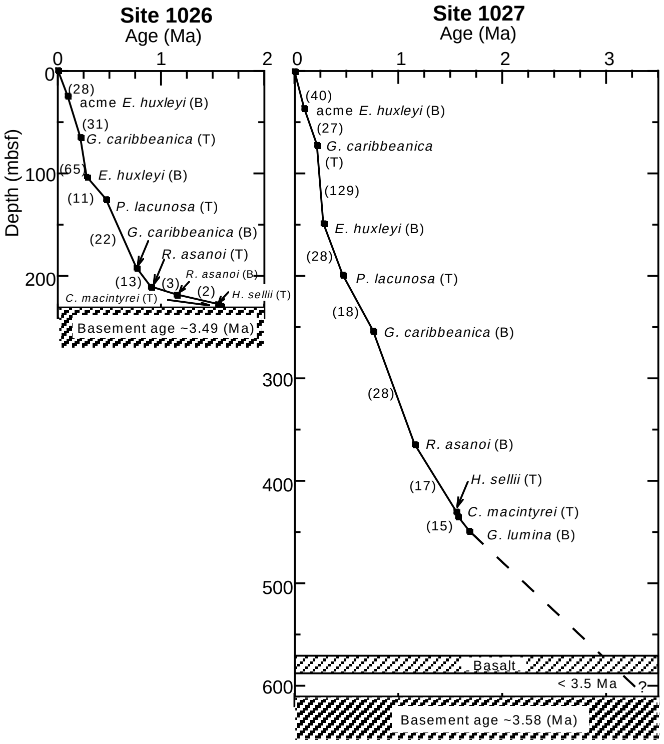

Figure 37. Age and depth correlation of nannofossil datums in Rough Basement Sites 1026 and 1027. Sedimentation rates (in centimeters per thousand years) are given in parentheses. Basement ages of these two sites are also given and show that sedimentation did not begin for several thousand years after basement formation at Site 1026, whereas it seems to have started soon after basement formation at Site 1027.

Figure 50 shows velocity anisotropy for the sediment and sedimentary rocks of Holes 1026C, 1027B, and 1027C. From approximately 250 to 460 mbsf in Hole 1027B, only horizontal (DSV 3) velocities were measured because of the semilithified condition of the core. The increase in anisotropy with depth probably results from greater compaction, increasing the preferred orientation of anisotropic mineral grains.

Thermal Conductivity

Thermal conductivity values were obtained from full-space needle-probe measurements on all cores recovered from Hole 1026B and, for Hole 1027B, until the sediment became lithified (Section 168-1027B-46X-4; 430 mbsf). The rest of the extended core barrel (XCB) cores from Hole 1027B and the RCB cores from Hole 1027C were measured using half-space line source in the split liner. Sediments were wetted for better contact. Hard rocks were removed from the liner, resaturated for at least 12 hr, and immersed with the probe in water during the measurement.

The correlation between porosity and thermal conductivity is shown in Figure 51. The data suggest matrix thermal conductivities from 1.3 to 5.0 W/(m·K). The calculated matrix thermal conductivities are greater in cores from the upper 100 mbsf of Holes 1026B and 1027B than from below 150 mbsf in Hole 1027B (no core recovery between 100 and 150 mbsf), averaging 3.6 and 2.6 W/(m·K), respectively. The former value is comparable to matrix thermal conductivity values determined during Leg 139 (Davis, Mottl, Fisher, et al., 1992). The lower matrix thermal conductivity below 150 mbsf may result from a lower quartz content and higher phyllosilicate content in these sediments.

A systematic increase in thermal conductivity with depth is apparent in cores from Hole 1027C from 280 to 580 mbsf, where the porosity decreases linearly from almost 60% to 40%, and thermal conductivity increases from 1.0 to 1.5 W/(m·K) (see Fig. 45). However, there is no indication that this relationship holds for the high-porosity sediments recovered in the upper 100 mbsf at any of the Hydrothermal Transition or Rough Basement sites. As with the observed relationship between *P*-wave velocity and porosity (Fig. 49), thermal conductivity appears to vary consistently with porosity only within the deeper, more compacted material. The thermal conductivity of shallow sediments depends more strongly on the relative abundance of sand, despite the fact that compaction gradients are expected to be the greatest near the seafloor.

The mean values of thermal conductivity at the Rough Basement sites are higher than those observed at the Hydrothermal Transition sites at equivalent depths. Thermal conductivity values for mud and sand also differ significantly within the upper 100 mbsf (Table 20). The difference between the two lithologies cannot be explained solely by differences in porosity. The matrix thermal conductivity of sand appears to be higher than that of mud, which is consistent with XRD analyses that suggest higher quartz and feldspar contents in sand than in mud (see Fig. 9).

Formation Factor

Formation factor calculated from electrical resistance measurements in sediment increases from about 1.5 to 5 with depth at Site 1026 and from 2 to 24 at Site 1027. Sandy layers generally have higher values than does mud, so each of the two sediment types was fit separately with a power function for Site 1026 (Table 23 on CD-ROM, back pocket). A weighted value for this function was then calculated from the proportions of mud vs. sand given in Table 21. For Site 1027, too few sand layers were measured to fit reliably. We have adjusted the exponential curve fit to the clay data upward based on the proportion of sand present and its general effect at the other sites; the uncertainty in this curve is therefore larger than for the others. The resulting functions are $FF = 1.802d^{0.1881}$ for Site 1026 and $FF = 2.3845e^{0.0026d}$ for Site 1027, where d is depth in mbsf.

Rock Properties

The igneous rocks of Sites 1026 and 1027 are categorized as (1) pillow basalt, which includes most of the igneous rock of Holes 1026B and 1027C; (2) diabase, which was found between 584.8 and 594.4 mbsf in Hole 1027C; and (3) hyaloclastite, which was mainly found between 267.4 and 277.0 mbsf in Core 168-1026B-3R. Table 20 shows the average, standard deviation, and number of measurements included in each category.

The MS, GRAPE, and NGR measurements in the relatively unbroken sections of diabase show smooth profiles except for the low values at core sections and breaks. For the pillow basalt, some of the variability in magnetic susceptibility and GRAPE bulk density profiles results from the small piece sizes, fractures, and the space between pieces. The pieces of pillow basalt from Hole 1026B are typically rounded and have dimensions no larger than 15 cm, whereas the pieces from Hole 1027C are generally longer and more cylindrical.

The DSV *P*-wave velocity of the diabase is higher than that of the pillow basalt (Table 22 on CD-ROM, back pocket). The higher porosities, lower velocities, and lower grain densities of samples from Hole 1026B are associated with hyaloclastite samples (Fig. 45). Diabase and pillow basalt samples display no significant *P*-wave anisotropy of (Fig. 52).

Table 16. Composition of pore waters from sediments from Sites 1026 and 1027.

Core, section, interval (cm)	Volume (mL)	Squeeze T (°C)	In situ T (°C)	Depth (mbsf)	Salinity (R.I.,%)	pH	Alkalinity (meq/kg)	Chlorinity (mmol/kg)	Sulfate (mmol/kg)	Na (mmol/kg)	K (mmol/kg)	Mg (mmol/kg)	Ca (mmol/kg)	Si (µmol/kg)	NH_3 (µmol/kg)	PO_4 (µmol/kg)	Na/Cl
168-1026A-																	
1H-1, 140–150	55	5.3	2.2	1.45	35.0	7.73	5.03	543.3	25.70	466.6	12.24	50.38	10.05	655	214	25.5	0.8589
1H-2, 140–150	30	7.2	2.6	2.95	35.0	7.83	9.41	543.4	25.70	471.5	12.11	50.32	10.03	622	398	41.8	0.8675
1H-3, 140–150	55	8.0	3.0	4.45	34.5	7.85	9.90	544.4	22.87	468.8	11.75	50.03	9.71	710	555	52.0	0.8612
2H-2, 140–150	55	8.2	4.0	8.35	34.5	7.83	16.46	547.8	15.21	466.6	10.23	49.90	9.01	548	1014	34.1	0.8518
2H-3, 140–150	55	8.6	4.4	9.85	34.5	7.85	17.88	551.7	13.78	470.2	10.20	49.52	8.85	546	1061	27.9	0.8522
2H-5, 140–150	55	10.4	5.2	12.85	34.5	8.02	20.45	555.1	12.08	472.8	9.99	49.97	8.49	522	1234	30.4	0.8517
3H-5, 140–150	20	12.0	7.6	22.35	34.5	8.16	27.98	560.9	7.30	477.9	8.93	50.99	7.32	339	1425	10.0	0.8521
4H-5, 140–150	55	11.3	10.1	31.85	34.5	8.08	31.74	563.3	4.21	484.4	7.53	48.76	7.04	441	1743	48.6	0.8598
5H-5, 140–150	55	12.0	12.6	41.35	34.5	7.92	32.96	562.4	0.33	479.1	7.58	47.75	6.92	581	1855	41.2	0.8519
6H-1, 140–150	55	10.0	13.5	44.85	34.5	7.92	30.55	561.4	0.85	478.0	7.84	47.57	6.33	439	2001	30.1	0.8515
7H-5, 140–150	55	—	17.6	60.35	34.5	8.03	26.53	561.4	0.31	477.0	6.99	45.48	6.83	576	1306	8.5	0.8496
8H-6, 140–150	50	12.2	20.5	71.35	34.0	7.91	25.67	559.5	0.11	477.7	6.42	42.42	8.23	320	1190	5.7	0.8538
9H-4, 140–150	55	12.9	22.2	77.85	34.0	7.86	23.77	561.5	1.76	485.3	6.67	39.53	8.84	469	1295	8.2	0.8644
10H-5, 140–150	55	12.5	25.1	88.85	34.0	7.87	22.70	560.5	1.08	484.6	7.14	37.51	9.26	544	1418	10.3	0.8647
11H-5, 140–150	55	12.7	27.5	98.35	33.5	7.69	19.22	562.6	1.57	487.0	6.67	35.47	10.17	516	1392	7.9	0.8657
Post-MST samples:																	
4H-3, 140–150	37	18.7	9.4	28.85	34.5	7.57	27.01	561.4	4.01	475.3	7.68	49.64	7.07	458	1634	23.9	0.8467
6H-2, 60–70	50	19.5	13.7	45.55	34.0	7.74	30.57	557.5	0.49	473.7	7.55	47.49	6.42	535	1924	40.3	0.8497
8H-6, 130–140	35	18.9	20.4	71.25	33.5	7.80	25.12	558.5	0.55	478.4	6.59	41.81	8.07	335	1222	9.1	0.8565
10H-3, 110–120	55	19.4	24.2	85.55	33.5	7.72	21.86	557.6	0.55	480.0	7.11	37.79	8.92	646	1365	10.3	0.8609
168-1026C-																	
4R-1, 45–128	26	—	31.8	114.71	32.0	7.70	5.18	552.7	0.89	471.3	4.45	30.37	11.60	321	1097	3.5	0.8527
5R-1, 135–150	48	—	34.4	124.53	32.5	7.72	6.99	561.5	0.68	484.8	5.28	22.06	17.81	100	1145	33.7	0.8635
7R-1, 128–148	46	—	39.4	143.68	33.0	7.70	3.17	563.5	3.46	482.4	3.28	16.64	27.29	755	1151	2.0	0.8562
8R-1, 63–78	55	—	41.8	152.71	33.0	7.29	1.82	561.1	3.88	480.5	2.78	13.36	30.34	101	799	54.4	0.8564
9R-1, 135–150	50	—	44.5	163.03	34.0	8.06	1.10	561.5	5.56	477.3	2.06	9.82	37.37	379	953	4.2	0.8500
10R-2, 135–150	30	—	47.4	174.13	34.0	8.11	0.89	561.5	9.18	476.4	1.75	6.29	45.01	245	774	3.3	0.8485
10R-5, 135–150	32	—	48.5	178.63	34.0	8.00	0.37	561.5	10.06	471.6	1.46	6.15	47.13	226	629	3.8	0.8400
12R-1, 130–150	48	—	52.0	191.90	34.0	8.29	0.53	556.6	11.75	460.7	1.68	5.63	52.51	188	538	3.3	0.8277
13R-4, 130–150	42	—	55.7	206.00	34.0	7.77	0.33	551.7	13.90	451.8	1.63	5.50	57.69	252	354	0.6	0.8190
14R-4, 130–150	50	—	58.2	215.60	34.5	8.16	0.55	555.1	13.87	452.2	2.16	5.63	58.90	210	301	0.6	0.8146
15R-1, 81–104	49	—	59.4	220.23	35.0	7.85	0.36	550.8	14.10	442.7	2.24	5.87	61.33	176	247	0.8	0.8037
15R-2, 66–86	46	—	59.8	221.56	34.5	8.63	0.84	552.7	14.75	451.0	2.47	5.76	61.36	94	286	0.4	0.8161
15R-3, 59–79	60	—	60.2	222.99	34.5	8.57	0.29	551.7	14.62	444.3	2.50	5.34	61.88	155	218	1.1	0.8053
15R-4, 130–150	38	—	60.7	225.20	35.0	8.24	0.42	553.7	14.09	443.1	2.64	5.01	63.24	169	206	0.6	0.8003
15R-5, 45–65	40	—	60.9	225.85	35.0	8.03	0.32	550.8	14.81	445.3	2.71	4.85	61.49	159	220	1.1	0.8086
15R-6, 70–90	50	—	61.4	227.60	35.0	8.01	0.29	553.7	15.09	450.2	2.62	4.60	61.08	149	194	0.8	0.8131
15R-7, 25–45	30	—	61.6	228.65	35.0	8.00	0.35	551.3	14.43	437.3	2.38	4.64	65.72	173	171	0.8	0.7934
Basement at:			61.7	228.9													
168-1026B-																	
WSTP-1																	
Prime	10	—	63.8	256		—	—	554.2	17.28	465.5	6.56	2.18	56.17	427	118	0.5	0.8400
Overflow	353	—	63.8	256		6.83	1.70	464.8	17.08	466.5	6.72	2.74	55.69	985	81	1.2	0.8417
WSTP-2																	
Prime	10	—	63.8	256		—	—	550.8	16.73	461.0	6.57	2.21	56.13	759	124	1.3	0.8370
Overflow	1005	—	63.8	256		7.30	0.63	526.7	17.04	461.5	6.53	2.53	56.19	1062	87	1.0	0.8379
Basement at:			61.4	247.1													
Baby Bare Springs:				25.0		8.33	0.43	554.4	17.8	473	7.05	0	55.2		76	0.4	0.853
Basement age = 3.516 Ma																	
168-1027B-																	
1H-1, 140–150	55	3.9	1.9	1.45	34.5	7.74	5.18	541.3	26.16	468.2	11.68	49.45	9.98	679	208	32.2	0.8650
1H-2, 140–150	55	4.8	2.1	2.95	35.0	7.75	7.26	543.2	25.13	469.8	12.06	49.56	9.87	701	384	53.5	0.8649
3H-1, 140–150	55	8.9	3.3	15.15	35.5	7.70	20.76	552.2	15.31	467.1	9.14	53.56	10.09	462	1174	29.7	0.8459
3H-2, 140–150	55	9.2	3.5	16.65	35.5	7.80	24.02	553.2	15.96	474.0	8.72	53.40	9.80	484	1186	39.1	0.8569
3H-3, 140–150	55	9.6	3.6	18.15	35.5	7.80	23.81	553.8	15.25	471.5	8.68	54.21	9.74	396	1222	30.5	0.8514
3H-4, 140–150	55	8.8	3.8	19.65	35.5	7.75	24.19	554.6	14.58	473.6	8.42	53.31	9.67	447	1252	26.9	0.8539
3H-5, 140–150	55	6.5	3.9	21.15	35.5	7.70	24.17	553.6	14.67	474.2	8.31	53.18	9.12	409	1270	10.3	0.8566
4H-3, 140–150	55	9.8	4.5	27.65	36.0	7.55	25.61	554.6	11.85	472.9	7.46	53.58	8.19	392	1349	2.2	0.8527
5H-2, 140–150	55	7.9	5.3	35.65	36.0	7.82	26.83	553.6	10.77	473.6	7.77	52.40	7.93	367	1474	16.1	0.8554
6H-5, 140–150	55	9.2	6.7	49.65	36.0	7.73	27.31	555.6	9.62	475.0	8.31	51.38	8.05	420	1454	25.1	0.8549
7H-3, 0–18	55	10.2	7.2	54.79	36.0	7.64	28.11	555.6	10.18	476.8	8.39	49.72	9.70	512	1306	38.7	0.8582
8H-1, 140–150	55	8.6	8.0	62.65	35.5	7.54	26.95	552.2	10.53	473.9	8.16	48.80	10.28	514	1096	28.3	0.8582
17X-2, 130–140	55	8.2	16.5	148.35	34.0	7.61	24.21	547.8	6.34	469.9	7.59	47.72	5.89	843	1216	31.9	0.8578

Table 16 (continued).

Core, section, interval (cm)	Volume (mL)	Squeeze T (°C)	In situ T (°C)	Depth (mbsf)	Salinity (R.I.,%)	pH	Alkalinity (meq/kg)	Chlorinity (mmol/kg)	Sulfate (mmol/kg)	Na (mmol/kg)	K (mmol/kg)	Mg (mmol/kg)	Ca (mmol/kg)	Si (µmol/kg)	NH_3 (µmol/kg)	PO_4 (µmol/kg)	Na/Cl
19X-2, 0–12	55	8.3	18.3	166.26	33.5	7.74	29.49	550.7	1.72	477.4	8.83	42.65	6.04	655	1929	20.9	0.8669
22X-1, 135–150	40	—	21.2	194.93	33.5	7.87	29.17	547.2	0.69	476.8	7.32	40.23	6.57	827	2241	41.3	0.8714
22X-3, 135–150	55	—	21.5	197.93	33.5	7.57	26.13	548.8	0.59	475.7	8.16	39.85	6.27	908	2295	23.4	0.8668
23X-1, 85–100	20	7.9	22.1	204.13	33.0	7.76	25.90	549.1	0.46	478.1	7.82	37.90	7.11	653	2249	15.1	0.8706
25X-1, 135–150	20	8.6	24.0	223.83	33.0	7.78	23.07	544.0	0.78	473.4	7.59	35.23	8.58	650	2230	13.0	0.8703
26X-2, 135–150	24	8.6	25.2	234.93	32.5	7.83	19.88	546.9	1.11	476.3	8.04	33.96	8.34	863	2283	9.3	0.8710
27X-1, 135–150	47	—	26.0	243.03	32.5	7.80	17.18	548.8	1.06	476.7	8.12	33.65	7.96	901	2338	7.9	0.8687
28X-4, 135–150	46	—	27.4	257.23	32.5	7.85	13.81	549.8	0.48	474.3	7.44	32.32	9.06	540	2302	2.6	0.8628
29X-5, 135–150	28	—	28.5	268.33	32.5	7.85	12.30	547.8	1.67	473.7	7.40	30.90	10.26	609	2288	3.6	0.8648
30X-5, 135–150	48	—	29.4	277.93	32.5	7.83	11.39	551.7	1.48	477.9	7.03	29.57	10.98	892	2320	3.9	0.8662
31X-5, 135–150	15	—	30.4	287.53	32.0	7.80	8.83	550.8	3.06	477.6	6.52	29.25	11.53	836	2162	5.9	0.8672
32X-5, 135–150	44	—	31.3	297.23	32.0	7.70	6.87	546.9	0.84	469.4	5.22	27.48	12.92	512	1917	2.2	0.8583
33X-5, 130–150	42	—	32.3	306.80	32.0	7.80	5.29	548.3	0.46	467.8	4.11	26.91	14.40	424	1740	1.2	0.8532
34X-5, 135–150	50	—	33.3	316.53	32.0	7.70	5.11	549.3	0.92	471.3	3.65	24.99	15.64	1072	1754	2.2	0.8581
35X-2, 130–150	42	8.6	33.8	321.60	32.0	7.96	3.90	550.2	0.91	470.3	2.99	24.48	16.85	310	1526	1.2	0.8547
36X-5, 130–150	38	—	35.2	335.80	32.0	8.09	2.99	547.8	0.91	467.2	2.33	22.61	18.94	227	1406	1.6	0.8528
37X-5, 130–150	18	—	36.1	345.40	32.0	8.00	2.76	549.2	0.86	468.9	2.03	21.70	19.70	318	1331	2.2	0.8537
38X-5, 130–150	32	—	37.1	355.10	32.0	7.94	2.99	552.6	0.56	471.9	1.78	20.68	20.82	439	1239	0.9	0.8540
39X-5, 125–150	38	—	38.0	364.68	32.0	7.93	2.29	551.3	0.49	467.9	1.67	20.50	21.99	285	1130	1.6	0.8488
40X-5, 125–150	45	—	39.0	374.38	32.0	8.08	3.00	554.5	0.89	474.7	1.70	19.51	21.92	266	1242	1.6	0.8561
41X-2, 125–150	40	—	39.5	379.48	32.0	8.04	2.57	560.8	0.03	478.9	1.60	19.14	22.35	281	1172	1.2	0.8539
42X-5, 125–150	35	—	40.9	393.58	32.0	8.26	2.34	555.8	0.42	473.8	1.22	19.05	22.93	173	1100	1.6	0.8524
43X-5, 125–150	29	—	41.9	403.18	32.0	8.16	1.89	554.7	0.30	472.3	1.39	17.88	23.85	216	1034	1.2	0.8515
44X-5, 125–150	42	—	42.8	412.78	32.0	7.83	2.16	555.5	0.35	473.5	1.42	17.56	24.17	295	1019	1.9	0.8523
45X-5, 125–150	55	—	43.8	422.38	32.0	7.83	1.70	551.7	0.68	470.6	1.35	17.32	24.06	316	910	1.2	0.8531
46X-3, 125–150	44	—	44.4	428.98	32.0	8.08	2.22	551.7	0.25	470.5	1.18	16.38	25.00	243	878	2.9	0.8528
47X-5, 125–150	55	—	45.7	441.58	32.0	8.17	2.14	553.6	0.25	473.7	1.32	15.30	25.33	206	941	1.9	0.8556
48X-5, 125–150	42	—	46.7	451.28	32.0	8.24	1.35	549.2	0.55	469.6	1.27	14.79	25.61	177	877	0.9	0.8550
49X-5, 125–150	50	—	47.6	460.88	32.0	8.34	1.61	552.3	0.69	473.7	1.33	14.24	25.90	161	840	1.9	0.8577
50X-5, 125–150	22	—	48.6	470.38	32.0	8.13	1.54	552.2	0.41	471.5	1.03	14.15	26.86	183	828	1.3	0.8539
51X-5, 125–150	40	—	49.5	479.98	32.0	8.10	2.04	551.2	0.88	471.6	1.08	13.88	27.25	237	831	0.8	0.8557
52X-5, 125–150	42	—	50.5	489.58	32.0	8.18	2.07	553.8	0.74	474.6	1.22	13.08	27.67	231	801	0.8	0.8570
53X-5, 125–150	42	—	51.4	499.08	32.0	8.34	1.52	545.9	1.58	468.8	1.37	11.85	27.71	181	844	1.1	0.8587
54X-5, 125–150	25	—	52.4	508.68	32.0	6.72	9.52	545.9	0.80	472.5	1.82	11.24	29.10	807	958	1.3	0.8655
55X-5, 125–150	20	—	53.3	518.38	32.0	8.24	1.19	546.9	0.63	463.0	1.34	10.48	31.56	118	698	1.1	0.8466
56X-5, 125–150	34	—	54.3	527.98	32.0	8.11	0.99	551.7	1.04	465.8	1.42	9.96	34.03	97	660	1.0	0.8443
57X-2, 125–150	42	—	54.8	533.18	32.0	7.96	1.15	551.7	1.34	463.3	1.29	9.08	36.58	173	526	0.6	0.8399
57X-6, 125–150	20	—	55.4	539.18	32.5	8.47	0.74	553.6	2.78	468.9	1.52	8.51	36.73	79	583	0.5	0.8470
58X-5, 125–150	32	—	56.2	547.28	32.5	8.41	0.82	552.7	2.86	459.1	1.30	7.55	41.50	111	478	1.0	0.8308
59X-5, 125–150	16	—	57.2	556.88	32.5	8.54	1.07	551.7	4.20	456.2	1.52	7.35	45.89	91	406	0.6	0.8269
60X-2, 125–150	22	—	57.7	561.98	33.0	8.32	0.68	559.4	6.99	466.7	2.15	7.11	46.30	93	343	0.8	0.8344
60X-3, 125–150	26	—	57.8	563.48	32.5	8.44	1.39	553.1	6.07	457.5	1.97	6.10	49.12	89	360	0.8	0.8271
60X-4, 125–150	22	—	58.0	564.98	33.0	8.50	0.65	553.6	6.25	458.4	1.95	6.10	48.38	77	331	0.3	0.8281
60X-5, 125–150	36	—	58.1	566.48	33.5	8.12	0.48	556.5	6.11	456.8	1.76	5.70	50.04	111	339	0.3	0.8208
60X-6, 125–150	35	—	58.3	567.98	33.0	8.19	1.06	548.0	7.25	448.5	1.80	6.63	50.66	156	315	0.8	0.8184
168-1027C-																	
1R-6, 117–131	18	—	60.6	591.75	34.5	7.96	0.43	553.7	14.49	441.8	2.71	6.22	62.32	114	162	0.4	0.7980
2R-2, 130–150	40	—	61.1	596.36	34.5	8.62	0.52	554.7	14.99	443.6	2.88	5.90	65.45	96	160	0.4	0.7998
2R-4, 130–150	40	—	61.4	599.36	34.5	8.46	0.49	551.8	14.37	438.8	2.64	5.18	65.94	92	155	0.4	0.7952
2R-6, 125–150	32	—	61.7	602.36	34.5	9.06	0.48	550.8	14.47	445.9	3.28	4.98	62.47	70	160	0.4	0.8096
3R-1, 86–100	1	—	61.9	605.03	35.0	—	—	547.8	17.51	—	2.72	4.54	—	80	130	0.4	—
Basement at:			62.8	613.8													
Baby Bare Springs:			25.0			8.33	0.43	554.4	17.8	473	7.05	0	55.2		76	0.4	0.853
Basement age = 3.586 Ma																	

Notes: T = temperature, and R.I. = refractive index. — = not determined. Mg concentrations reported for Sections 168-1026-9R-1 and below and 1027B-53X-5 and below were determined by flame atomic absorption spectrophotometry rather than titrimetry. Aliquot from overflow chamber, with pH and chlorinity reported as measured; all other values have been corrected to the chlorinity of the prime aliquot, from the titanium coil.

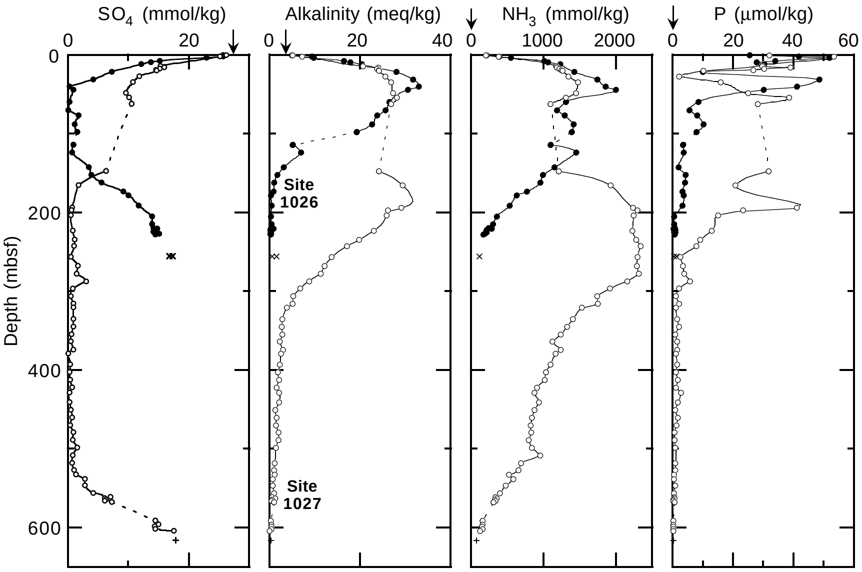

Figure 38. Composition of pore waters from the Rough Basement sites: sulfate, alkalinity, ammonia, and phosphate. Arrows = the composition of bottom seawater. Solid circles = Hole 1026A and 1026C; × symbols = Hole 1026B WSTP samples (plotted at the depth in basement where these waters originated before flowing into the cased hole); open circles = Holes 1027B and 1027C; and + symbols = Baby Bare springs (M. Mottl, unpubl. data; plotted below the sediment section for comparison).

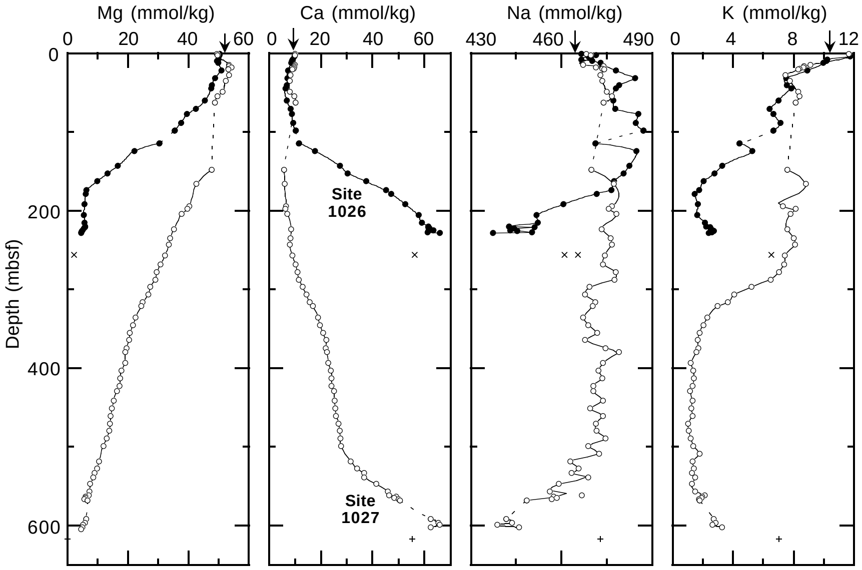

Figure 39. Composition of pore waters from the Rough Basement sites: magnesium, calcium, sodium, and potassium. Arrows = the composition of bottom seawater. Solid circles = Hole 1026A and 1026C; × symbols = Hole 1026B WSTP samples (plotted at the depth in basement where these waters originated before flowing into the cased hole); open circles = Holes 1027B and 1027C; and + symbols = Baby Bare springs (M. Mottl, unpubl. data; plotted below the sediment section for comparison).

THERMAL STUDIES

Sediment Measurements

In situ temperatures were measured at five depths in Hole 1026A, five depths in Hole 1026C, and 22 depths in Hole 1027B (Table 24). All tool deployments returned data, but DVTP runs 168-1027B-41X, 49X, and 62X did not provide useful constraints on in situ temperatures, probably because of insufficient probe penetration, cracking of the formation, or probe motion. Results of deployments in all three holes are illustrated in Figures 53 through 55.

The use of idealized thermal models to simulate tool response and the methods used for matching observations to the models to extrapolate equilibrium temperatures are discussed in the "Downhole Tools" section of the "Methods" chapter (this volume) and Davis et al. (1997). The selection of sediment thermal conductivity greatly influenced the results of the APC tool extrapolations, and it was difficult to determine a priori what value would produce results most consistent with surrounding values. Extrapolations based on a range of reasonable thermal conductivities (1.0 to 1.5 W/[m·K]) were calculated for all measurements (Table 24), and an intermediate value of 1.1 W/(m·K) was used for calculation of preliminary thermal gradients and heat flow (Figs. 56–58; Table 25). The symbols used to indicate equilibrium temperatures in these figures generally span the range of likely temperatures estimated using the range of thermal conductivities listed above. A more sophisticated analysis of these extrapolations will be conducted post cruise.

Figures 56 through 58 illustrate the thermal gradients determined at Sites 1026 and 1027, thermal conductivity-depth structures, and Bullard plots of heat flow. The thermal conductivity structure for each hole along the Rough Basement Transect was calculated as the weighted harmonic mean of measured values (see "Physical Properties" section, this chapter) within the depth intervals of the temperature measurements. Apparent thermal conductivities were generally higher along the Rough Basement Transect than along the Hydrothermal Transition Transect, reflecting the sandier nature of the sediments (see "Lithostratigraphy" and "Physical Properties" sections, this chapter). Because there was no sediment recovered between 88 and 146 mbsf in Hole 1027B, assumed conductivities were calculated for this depth interval as the values required to maintain constant, conductive heat flow. That these assumed values are relatively high (1.2 to 1.7 W/[m·K]) is consistent with the presence of sandy material thought to dominate the sedimentary section over these depths.

As along the Hydrothermal Transition Transect, DVTP data seem to provide the most consistent thermal gradients and heat-flow deter-

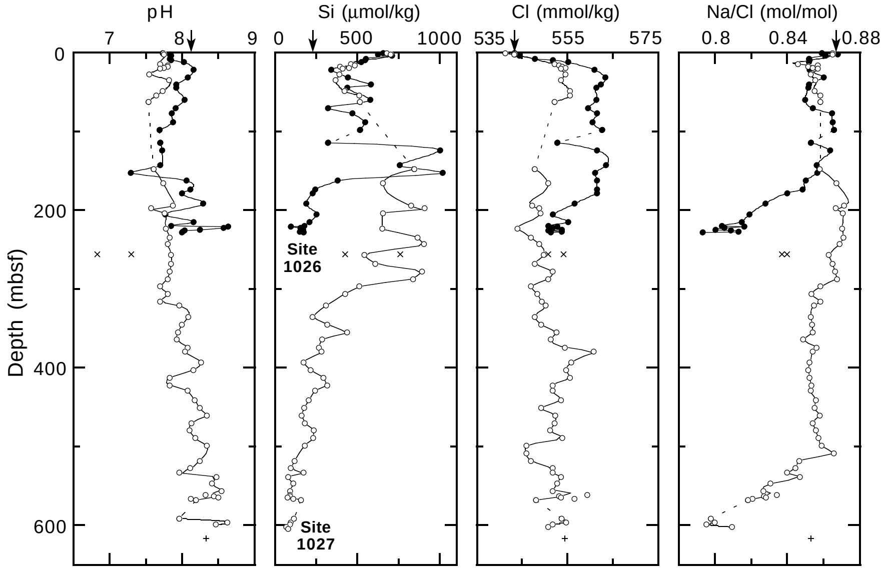

Figure 40. Composition of pore waters from the Rough Basement sites: pH, silica, chloride, and the sodium/chloride ratio. Arrows = the composition of bottom seawater. Solid circles = Hole 1026A and 1026C; × symbols = Hole 1026B WSTP measurements (plotted at the depth in basement where these waters originated before flowing into the cased hole); open circles = Holes 1027B and 1027C; and + symbols = Baby Bare springs (M. Mottl, unpubl. data, plotted below the sediment section for comparison).

minations, although there were some inconsistent apparent equilibrium temperatures obtained with both the DVTP and APC tool. The DVTP data from Hole 1027B suggest a somewhat steeper thermal gradient than that determined with DVTP and APC tool data combined. A comparison of bottom-water readings from the DVTP and APC tools suggests a significant temperature offset between the various tools (perhaps as great as 0.15°C), but the offset apparent in Hole 1027B sediment data is considerably greater than this (Fig. 58A). Analysis of these results will be the subject of additional post-cruise work.

The heat-flow values determined at the Rough Basement sites during Leg 168 are broadly consistent with earlier seafloor measurements (Davis et al., this volume), although values calculated at both Sites 1026 and 1027 are slightly lower than those determined with nearby surface measurements. The overall linearity of all Bullard plots from the Rough Basement sites indicates that thermal transport through the sediment column at these sites is entirely conductive.

Estimating temperatures at the top of basement at Sites 1026 and 1027 required a determination of sediment thickness at each site, as well as extrapolation of temperature trends to these depths. Drilling ended well above basement in Hole 1026A, but sediment thickness in this hole was assumed to be the same as that in Hole 1026B (only 4 m to the north) as identified from driller's records (Table 25). The depth to basement in Hole 1027B similarly was assumed to be the same as that in Hole 1027C (offset 50 m to the south-southwest). True basement (the shallowest possible occurrence of high permeability) in Hole 1027C was assumed to correspond to the shallowest pillow basalts below the sill (Fig. 58A; Table 25; see "Igneous Petrology" in the "Basement Lithology, Petrology, Geochemistry, and Alteration" section, this chapter).

As at other sites drilled during Leg 168, the thermal data presented in this section provide no constraints on the actual location or sharpness of hydrologic basement. Conductive conditions may persist through massive units some distance into the upper igneous crust, although drilling conditions, basalt recovery, packer experiments, and the open-hole temperature log described below suggest that high permeability is present no more than a few meters below the first occurrence of pillow basalts in Hole 1026B.

Open-Hole Measurements

Because of drilling and hole-cleaning difficulties in Hole 1026B, a piece of old drill pipe was drilled into the hole as a liner (see "Operations" section, this chapter). After coring in Hole 1026C, Hole 1026B was reentered to make a final check of hole depth inside the liner before terminating the CORK thermistor string.

The DVTP was run into the hole on the coring line so that we could also determine the bottom-hole temperature and look for evidence of fluid flow either into or out of the formation. The lower 50 m of Hole 1026B was "logged" with the DVTP by pausing for 2 min at 5-m depth intervals. The DVTP data suggested that warm water was flowing out of the formation somewhere within the upper 20 m of basement, around the liner, and up the hole. We decided to collect a water sample of this fluid and make detailed measurements of shallower borehole fluid temperatures so that we could estimate the velocity of the water flowing up the hole.

The WSTP was prepared for sampling in the borehole, and an APC tool was installed in place of the normal WSTP landing shoe, about 0.5 m behind the sample intake port, to collect temperature data during the deployment. The WSTP data logger was also run to collect temperature data from the WSTP thermistor sensor, about 5 cm in front of the sample intake port. The pipe was positioned near the top of the hole, and the WSTP was lowered on the coring line to 211 mbsf (8 m above the top of the liner) to collect a fluid sample (Fig. 59). The hole was then logged by raising the tool in 10-m depth increments and pausing for 3 min to allow partial thermal equilibration.

The water sample collected during this deployment was too small for carbon-14 dating, and the APC tool and WSTP data loggers had stopped recording before reaching the uppermost part of the hole, so the tools were deployed a second time to collect additional water and temperature data. During the second deployment, a larger water sample was obtained (see "Inorganic Geochemistry" section, this chapter) and temperatures in the shallowest part of the borehole were logged at depth increments of 2–5 m.

A composite record of the DVTP and both APC tool open-hole deployments in Hole 1026B is shown in Figure 59. Despite measuring many of the borehole temperatures within drill pipe (below the top of the liner at 218 mbsf and above the bottom of the drill string at 60 mbsf), the data provide convincing evidence of fluid flow out of the formation and up the borehole. Fluid seems to enter the borehole between 247 and 262 mbsf, where temperatures measured within the liner are nearly isothermal at 64°C. The gentle, but consistent, decrease in measured temperatures as the tools were pulled up the hole documents heat loss through the casing and into the surrounding formation. The abrupt increase in the thermal gradient near the seafloor reflects the juxtaposition of warm formation water flowing up the

Table 17. Headspace composition data from Sites 1026 and 1027.

Core, section, interval (cm)	Depth (mbsf)	C_1 (ppmv)	C_2 (ppmv)	C_3 (ppmv)	C_2 (ppmv)	C_1/C_2
168-1026A-						
1H-3, 0–5	3.03	2				
2H-6, 0–5	12.93	3				
3H-6, 0–5	22.43	2				
4H-6, 0–5	31.93	2				
5H-6, 0–5	41.43	3				
6H-5, 0–5	49.43	3				
7H-6, 0–5	60.43	977				
8H-6, 0–5	69.93	4,053				
9H-4, 0–5	76.43	5,526				
10H-6, 0–5	88.93	10,257				
11H-6, 0–5	98.43	13,204				
12H-1, 0–5	100.43	10,616				
168-1026C-						
1R-1, 0–5	84.63	978				
2R-1, 0–5	94.23	1,740				
3R-1, 0–5	103.83	1,369				
4R-1, 0–5	113.53	303				
5R-1, 0–5	123.13	22				
6R-1, 0–5	132.73	10				
7R-1, 0–5	142.33	8				
8R-1, 0–5	152.03	8				
9R-2, 0–5	163.13	8				
10R-6, 0–5	178.73	8				
12R-1, 0–5	190.53	8				
13R-5, 0–5	206.13	10				
14R-5, 0–5	215.73	5				
15R-5, 0–5	225.33	5				
168-1027B-						
1H-3, 0–5	3.03	2				
3H-6, 0–5	21.23	2				
4H-6, 0–5	30.73	104				
5H-6, 0–5	40.23	72				
6H-6, 0–5	49.73	47				
7H-6, 0–5	59.23	30				
17X-3, 0–5	148.53	2				
19X-2, 0–5	166.23	16,437				
22X-5, 0–5	199.53	16,919	0.6			28,198
23X-2, 0–5	204.83	16,004	0.6			26,673
25X-2, 0–5	223.93	12,165	0.6			20,275
26X-3, 0–5	235.03	27,681	1.2			23,068
27X-1, 0–5	241.63	32,806	1.4		0.7	23,433
28X-5, 0–5	257.33	16,831	1.2			14,026
29X-6, 0–5	268.43	18,162	1.4			12,973
30X-6, 0–5	278.03	26,136	1.7			15,374
31X-6, 0–5	287.63	11,504	1.2			9,587
32X-6, 0–5	297.43	21,292	2.6			8,189
33X-6, 0–5	306.93	29,689	3.4			8,732
34X-6, 0–5	308.63	12,922	2.4			5,384
35X-6, 0–5	326.23	8,678	1.7			5,105
36X-6, 0–5	335.93	22,121	4.2			5,267
37X-6, 0–5	345.53	15,111	2.8			5,397
38X-6, 0–5	355.23	20,906	3.9			5,361
39X-5, 0–5	363.33	18,809	4.0	1.5		4,702
40X-6, 0–5	374.53	13,121	2.6			5,047
41X-3, 0–5	379.63	12,514	2.5			5,006
42X-6, 0–5	393.73	13,794	3.2	1.5		4,311
43X-6, 0–5	403.33	11,351	3.6	5.0		3,153
44X-6, 0–5	412.93	7,294	2.3	1.0		3,171
45X-6, 0–5	422.53	15,405	5.0	5.0		3,081
46X-4, 0–5	431.13	14,642	5.5	7.9		2,662
47X-6, 0–5	441.73	12,106	3.0	8.0		4,035
48X-6, 0–5	451.43	8,081	6.0	12.0		1,347
49X-6, 0–5	461.03	12,357	4.0	5.5		3,089
50X-6, 0–5	470.53	8,269	4.7	7.9		1,759
51X-6, 0–5	480.13	2,825	1.6	2.2		1,766
52X-6, 0–5	489.73	2,747	1.8	4.2		1,526
53X-6, 0–5	499.23	2,556	2.0	3.9		1,278
54X-6, 0–5	508.83	2,428	2.0	3.0		1,214
55X-6, 0–5	518.53	2,509	4.0	1.0	2.8	627
56X-6, 0–5	528.13	2,776	3.0			925
57X-6, 0–5	537.83	1,689	2.0			845
58X-6, 0–5	547.43	1,812	2.0			906
59X-6, 0–5	557.03	936	1.0			936
60X-6, 0–5	566.63	465				
168-1027C-						
1R-6, 117–131	593.54	2				
2R-6, 0–5	601.93	3				

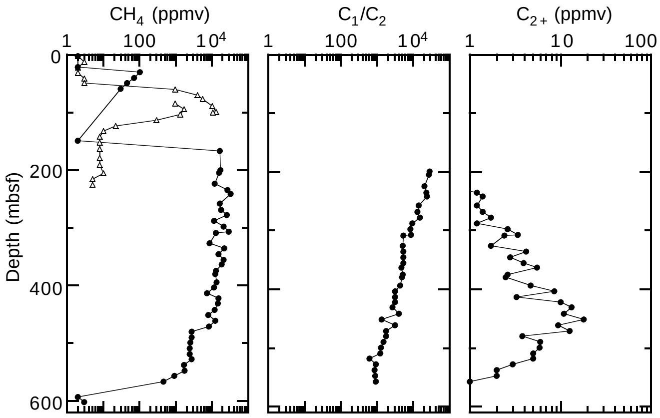

Figure 41. Profiles of methane, C_1/C_2 and C_{2+} in headspace samples from Sites 1026 and 1027. Open triangles = Holes 1026A and 1026C; solid circles = Holes 1027B and 1027C.

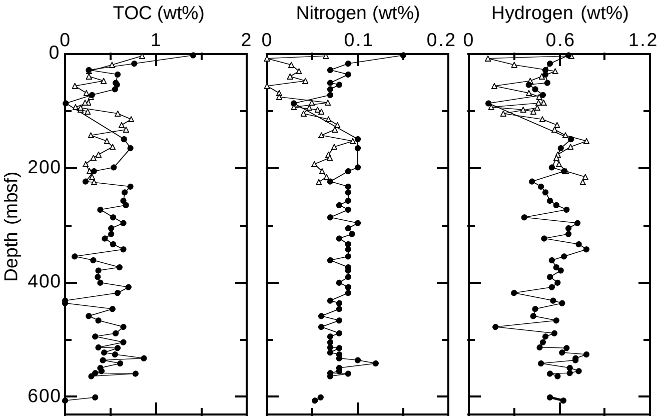

Figure 42. Depth distribution of organic carbon, total nitrogen, and total hydrogen in sediment from Sites 1026 and 1027. Open triangles = Holes 1026A and 1026C; solid circles = Holes 1027B and 1027C.

borehole and cold bottom water in the overlying ocean. These data will be analyzed post cruise to estimate the velocity of fluid flow within the borehole.

PACKER EXPERIMENTS

The drill-string packer was deployed in both Holes 1026B and 1027C to determine permeability and estimate in situ pressures of the uppermost basement at these sites. Hole conditions were very poor in the basement section of Hole 1026B, so the packer could be inflated only in casing. Although 46.7 m of open hole had been drilled or cored in basement beneath the casing shoe, more than 30 m of fill had accumulated by the time of the packer experiments. The fill precluded any possibility of inflating the packer in open hole and introduced a large ambiguity in the length and composition of the section actually tested during the packer experiments. In contrast, hole conditions were much better in the basement section in Hole 1027C, and the packer could be inflated at two positions: first in casing and then in the sill intruded into sediments above extrusive basement. The packer experiments in both holes were conducted during a single pipe trip, with the ship offset in DP mode between holes. The results of these

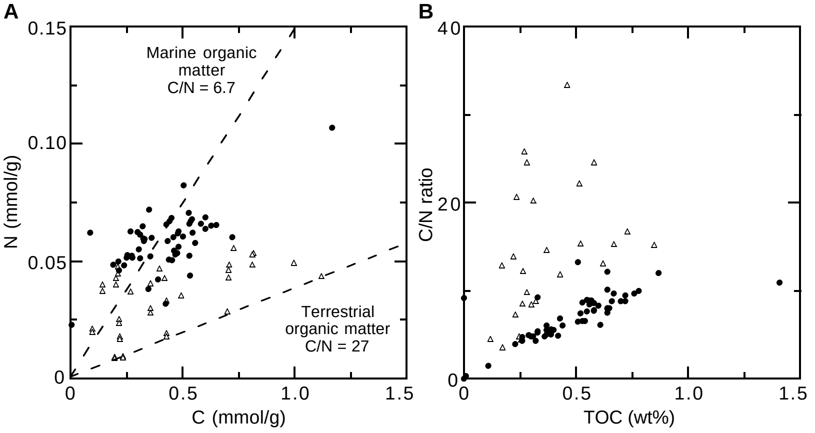

Figure 43. **A.** Total nitrogen vs. total organic carbon in sediment from Sites 1026 and 1027. **B.** Total organic carbon vs. C/N ratio in sediments from Sites 1026 and 1027. Open triangles = Holes 1026A and 1026C; solid circles = Holes 1027B and 1027C.

Table 19. Results of Rock-Eval pyrolysis on samples from Sites 1026 and 1027.

Core, section, interval (cm)	Depth (mbsf)	Weight (mg)	T_{max} (°C)	S_1	S_2	S_3	PI	S_2/S_3	PC	TOC (wt%)	HI	OI
168-1026A-												
3H-3, 102–103	18.93	100.80	434	0.04	0.25	0.56	0.14	0.44	0.02	0.51	49	109
168-1027B-												
1H-2, 97–98	2.48	99.30	392	0.29	3.11	1.48	0.09	2.10	0.28	1.41	220	104
3H-3, 38–40	17.09	101.60	513	0.09	0.50	1.25	0.16	0.40	0.04	1.76	28	71
5H-3, 63–64	36.34	102.30	434	0.04	0.28	1.21	0.12	0.23	0.02	1.58	17	76
19X-1, 54–55	165.25	100.20	548	0.03	0.52	0.69	0.06	0.75	0.04	0.72	72	95
26X-1, 29–31	323.30	99.40	381	0.03	0.13	2.13	0.19	0.06	0.01	0.30	43	710
32X-4, 103–104	295.34	100.10	433	0.03	0.54	0.96	0.05	0.56	0.04	0.64	84	150
40X-5, 65–66	373.66	100.60	448	0.03	0.49	0.31	0.06	1.58	0.04	0.60	81	51
44X-2, 110–112	408.01	100.90	467	0.03	0.38	0.59	0.07	0.64	0.03	0.70	54	84
45X-3, 14–15	418.15	100.90	431	0.06	0.27	3.46	0.19	0.07	0.02	0.58	46	596
51X-4, 55–56	477.66	100.10	405	0.04	0.16	0.62	0.20	0.25	0.01	0.64	25	96
54X-2, 134–135	504.15	100.40	440	0.03	0.52	0.34	0.06	1.52	0.04	0.64	81	53
57X-2, 28–29	532.09	103.40	439	0.02	0.39	0.39	0.05	1.00	0.03	0.87	44	44
58X-1, 89–91	540.80	103.00	546	0.01	0.39	0.47	0.02	0.82	0.03	0.61	63	77
59X-4, 51–52	554.52	101.00	427	0.04	0.44	0.31	0.08	1.41	0.04	0.40	110	77
59X-6, 73–74	557.74	101.30	434	0.03	0.36	0.57	0.08	0.63	0.03	4.27	8	13
60X-4, 28–29	563.89	100.90	449	0.01	0.36	0.34	0.03	1.05	0.03	0.29	124	117

Note: PI = production index = $S_2/(S_1+S_2)$, PC = pyrolyzed carbon = $0.083(S_1 + S_2)$, TOC = total organic carbon, HI = hydrogen index, and OI = oxygen index.

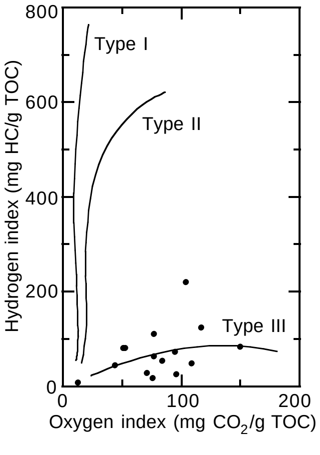

Figure 44. Hydrogen index plotted vs. the oxygen index for Hole 1027B.

experiments require post-cruise processing to determine formation transmissivity and permeability, and only qualitative interpretation is presented here.

Figure 60 shows the pressure record collected by the downhole gauge during the experiments conducted with the packer inflated in Hole 1026B at 229.2 mbsf in casing, 19.3 m above the casing shoe. Two slug tests were conducted, with moderately rapid decay rates indicative of moderately high transmissivity in the tested section. The rig floor pressure readings did not show the full decays of these slug tests, which were masked by the differential observed downhole between hydrostatic pressure in the unsealed borehole and the lower reference pressure observed when the packer was inflated (Fig. 60). Such a negative differential is consistent with cooling of the formation near the hole by circulation during drilling operations, and its observation during the packer experiments attests to the hydraulic integrity of the cement behind the casing. When Hole 1026B was revisited nearly three weeks later for installation of a CORK, a temperature log showed the hole was producing formation fluids (see "Thermal Studies" section, this chapter). For the hole to produce fluids required that the negative differential pressures induced by drilling operations be reversed as the formation re-equilibrated from the drilling disturbance, showing that true formation pressures were actually greater than hydrostatic pressure in the cold borehole. After the slug tests, two injection tests were conducted. These tests did not display the expected linear rise of pressures with log time, possibly indicating inadvertent fracturing of the formation and/or radial heterogeneities in the hydrologic properties of the rock in the test section as might be expected with the large amount of fill in the hole.

Figure 61 shows the downhole pressure records collected from the two packer inflations in Hole 1027C. The packer was first inflated at 560.7 mbsf, 17.7 m above the casing shoe, and a sequence of three slug tests and two injection tests was conducted (Fig. 61A). The packer was then moved 30 m deeper (for an inflation in a 6-m-thick sill cored beneath the casing shoe), where two slug tests and two injection tests were conducted (Fig. 61B). The sill overlies about 10 m

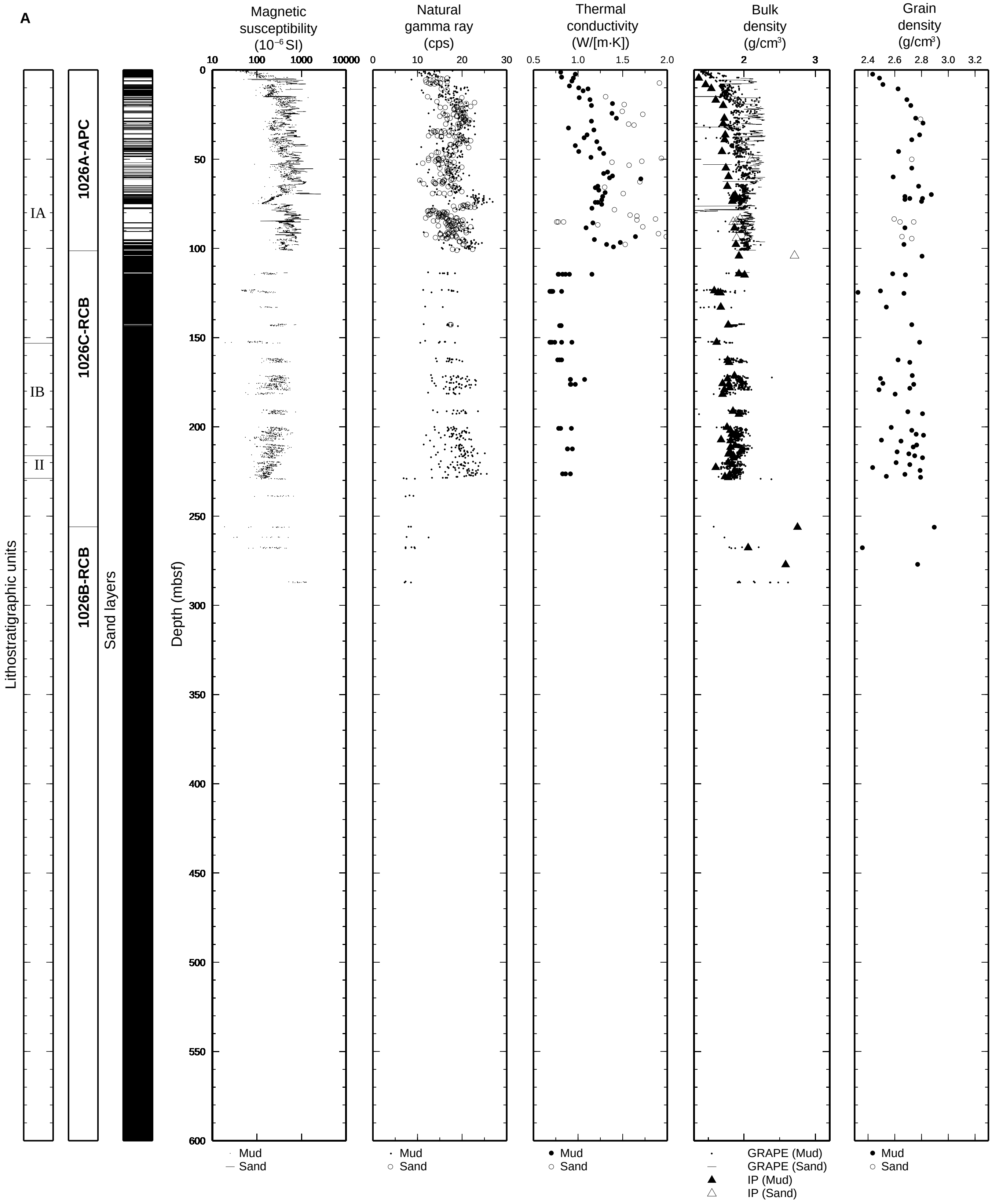

Figure 45. Summary plots for physical properties with lithostratigraphic units and identified sand (white) layers for (**A**) Holes 1026A and 1026B and (**B**) Holes 1027B and 1027C. Data in (A) from below 229 mbsf at Site 1026 and in (B) from 580–592 mbsf and below 610 mbsf at Site 1027 are from measurements of basalt rather than sediment.

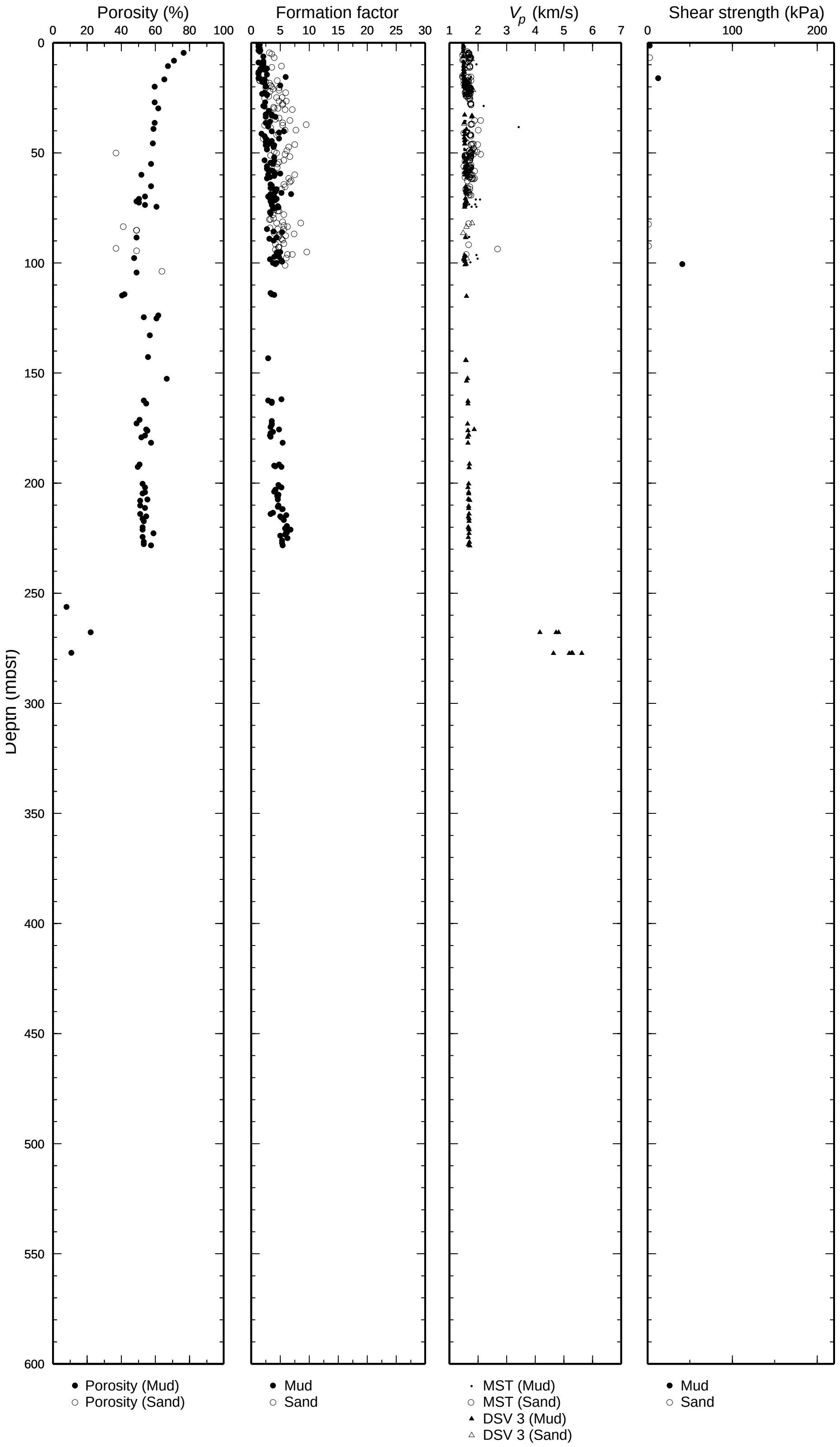

Figure 45 (continued).

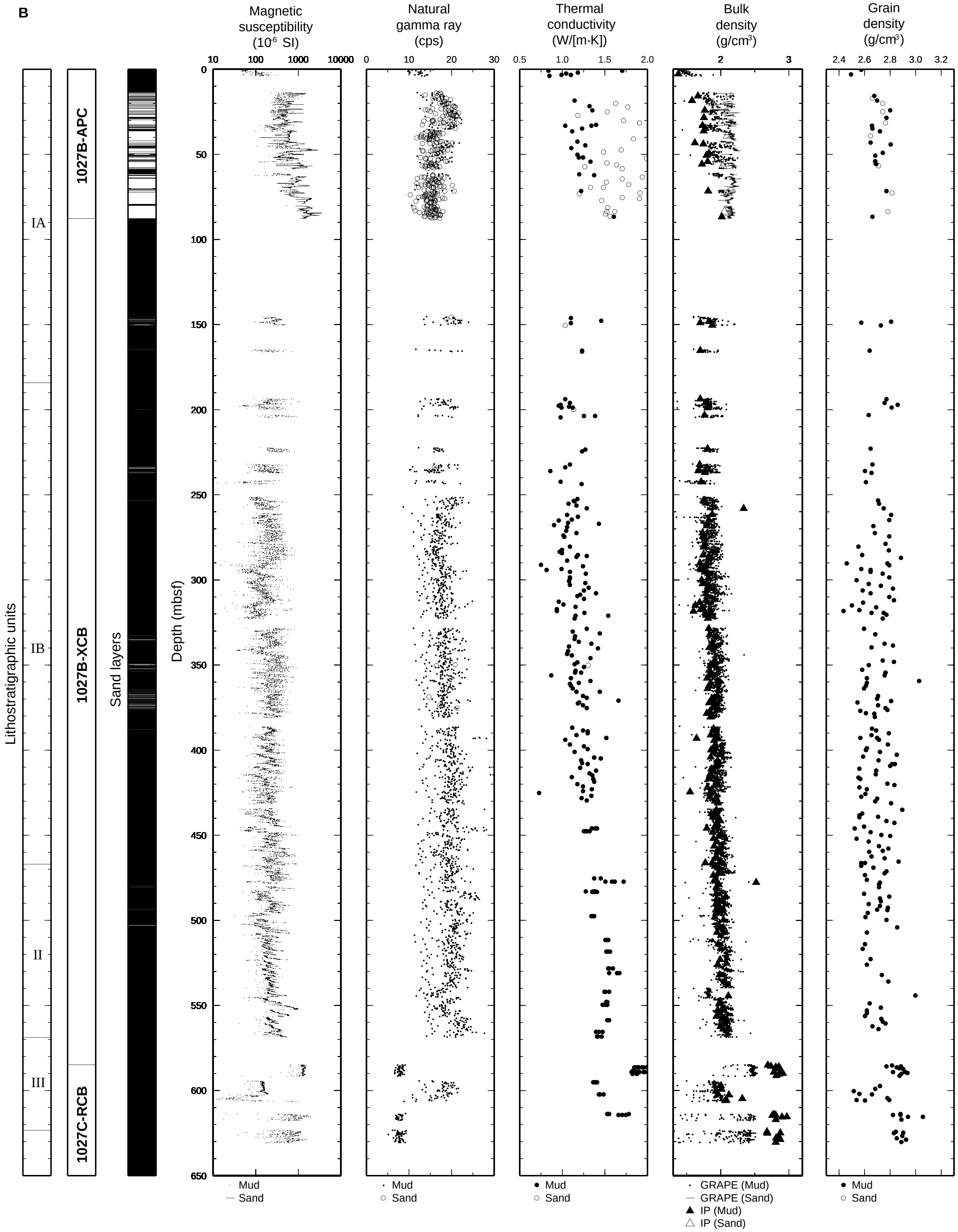

Figure 45 (continued).

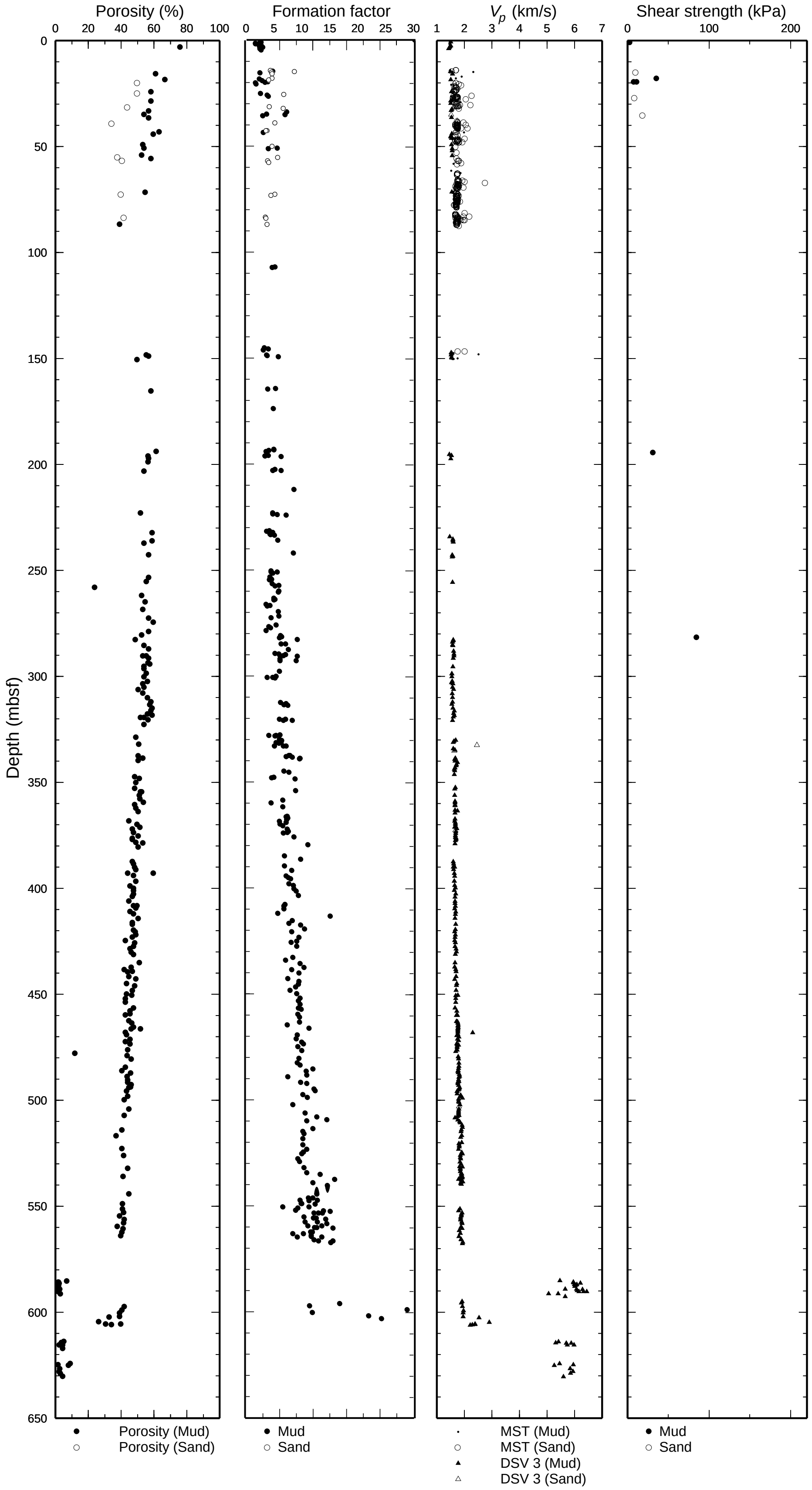

Figure 45 (continued).

Table 20. Physical properties measurements for mud, sand, diabase, pillow basalts, and hyaloclastite from Sites 1026 and 1027.

		Mud			Sand			Diabase			Pillow basalt			Hyaloclastite		
	Hole	Average	SD	*n*	Average	SD	*n*	Average	SD	*n*	Average	SD	*n*	Average	SD	n
MS (10^{-6} SI)	1026A	300	100	1797	600	200	1583	—	—	—	—	—	—	—	—	—
	1026B	—	—	—	—	—	—	—	—	—	500	300	46	220	80	27
	1026C	230	80	1506	400	100	19	—	—	—	—	—	—	—	—	—
	1027B	400	300	822	1000	500	1558	—	—	—	—	—	—	—	—	—
	1027C	—	—	—	—	—	—	1300	100	232	700	300	427	—	—	—
GRAPE (g/cm^3)	1026A	1.9	0.2	1032	2.1	0.2	907	—	—	—	—	—	—	—	—	—
	1026B	—	—	—	—	—	—	—	—	—	2	0.4	15	1.7	0.3	7
	1026C	1.89	0.09	847	1.97	0.05	9	—	—	—	—	—	—	—	—	—
	1027B	1.9	0.2	472	2.14	0.09	895	—	—	—	—	—	—	—	—	—
	1027C	2.44	0.06	132	2.44	0.06	132	2.44	0.06	132	2.1	0.3	203	—	—	—
IP bulk density (g/cm^3)	1026A	1.8	0.4	23	2.06	0.09	4	—	—	—	—	—	—	—	—	—
	1026B	—	—	—	—	—	—	—	—	—	2.67	0.08	2	2.06	—	1
	1026C	1.79	0.07	42	—	—	—	—	—	—	—	—	—	—	—	—
	1027B	1.7	0.2	17	2.02	0.08	9	—	—	—	—	—	—	—	—	—
	1027C	2.82	0.02	4	2.82	0.02	4	2.82	0.07	11	2.82	0.08	13	—	—	—
IP grain density (g/cm^3)	1026A	2.7	0.1	22	2.7	0.09	4	—	—	—	—	—	—	—	—	—
	1026B	—	—	—	—	—	—	—	—	—	2.84	0.06	2	2.36	—	1
	1026C	2.7	0.1	42	—	—	—	—	—	—	—	—	—	—	—	—
	1027B	2.69	0.08	17	2.73	0.06	9	—	—	—	—	—	—	—	—	—
	1027C	2.86	0.02	4	2.86	0.02	4	2.87	0.05	11	2.89	0.06	13	—	—	—
IP porosity (%)	1026A	58	8	23	38	2	4	—	—	—	—	—	—	—	—	—
	1026B	—	—	—	—	—	—	—	—	—	9	1	2	22	—	1
	1026C	53	3	42	—	—	—	—	—	—	—	—	—	—	—	—
	1027B	60	10	17	42	5	9	—	—	—	—	—	—	—	—	—
	1027C	2.4	0.4	4	2.4	0.4	4	2.41	1.57	11	4.14	2.26	13	—	—	—
Therm. cond. (W/[m·K])	1026A	1.2	0.2	49	1.7	0.2	27	—	—	—	—	—	—	—	—	—
	1026B	—	—	—	—	—	—	—	—	—	—	—	—	—	—	—
	1026C	0.83	0.08	42	—	—	—	—	—	—	—	—	—	—	—	—
	1027B	1.3	0.3	27	1.7	0.3	34	—	—	—	—	—	—	—	—	—
	1027C	1.89	0.05	22	1.89	0.05	22	1.89	0.05	22	1.66	0.08	6	—	—	—
PWL (km/s)	1026A	1.54	0.06	486	1.69	0.07	242	—	—	—	—	—	—	—	—	—
	1027B	1.6	0.1	87	1.75	0.05	321	—	—	—	—	—	—	—	—	—
DSV 3 velocity (km/s)	1026A	1.56	0.06	44	1.7	0.1	9	—	—	—	—	—	—	—	—	—
	1026B	—	—	—	—	—	—	—	—	—	5.2	0.2	7	4.6	0.3	3
	1026C	1.67	0.03	36	—	—	—	—	—	—	—	—	—	—	—	—
	1027B	1.53	0.02	20	1.68	0.08	10	—	—	—	—	—	—	—	—	—
	1027C	5.9	0.3	8	5.9	0.3	8	5.84	0.33	59	5.61	0.27	69	—	—	—
NGR (cps)	1026A	18	3	343	17	3	279	—	—	—	—	—	—	—	—	—
	1026B	—	—	—	—	—	—	—	—	—	9	1	7	8.2	0.8	7
	1026C	18	3	271	17.5	0.1	2	—	—	—	—	—	—	—	—	—
	1027B	17	3	160	16	2	282	—	—	—	—	—	—	—	—	—
	1027C	7.9	0.5	43	7.9	0.5	43	7.9	0.5	43	7.8	0.6	78	—	—	—
FF	1026A	3.04	1.18	136	5.09	1.41	98	—	—	—	—	—	—	—	—	—
	1026B	—	—	—	—	—	—	—	—	—	—	—	—	—	—	—
	1026C	4.56	1.00	297	—	—	—	—	—	—	—	—	—	—	—	—
	1027B	6.40	2.69	293	3.99	1.07	21	—	—	—	—	—	—	—	—	—
	1027C	16.03	5.86	6	—	—	—	—	—	—	—	—	—	—	—	—

Notes: SD = standard deviation, and *n* = number. — = no samples. Measurements are for magnetic susceptibility (MS), bulk density from GRAPE and index properties (IP) measurements, IP grain density and porosity, thermal conductivity (Therm. cond.), *P*-wave velocities from the MST (PWL) and DSV, natural gamma-ray activity (NGR), and formation factor (FF) from electrical resistivity.

Table 21. The number of measurements for identified sand samples relative to the total number of measurements in comparison with the total thickness of sand layers relative to the depth of drilled section.

Measurement type	Site 1026 (% sand)	Site 1027 (% sand)
Sand (full hole)	31.25	12.39
GRAPE	32.77	12.89
MS	32.66	12.87
NGR	31.39	12.42
PWL	33.24	78.68
DSV	10.1	4.84
IP	5.88	4.46
TC	23.89	14.18
FF	33.33	6.56

Note: In this table, Sites 1026 and 1027 consist of Holes 1026A, 1026C, and 1027B, respectively. Measurements: GRAPE = gamma-ray attenuation porosity evaluator; MS = magnetic susceptibility; NGR = natural gamma-ray activity; PWL = *P*-wave logger; DSV = digital sonic velocimeter; IP = index properties; TC = thermal conductivity; and FF = formation factor.

of mudstones and extrusive basement, so both inflations tested the integrated hydraulic properties of a sequence of disparate lithologies. At both inflation depths, there was a clear differential between baseline pressure in the sealed hole and hydrostatic pressure in the open borehole. As at Hole 1026B, this is consistent with cooling of the zone surrounding the hole by the fluids circulated during drilling, and it confirms the hydraulic integrity of the cement behind the casing. The decays of the slug tests were of similar duration at both inflation depths, indicating comparable transmissivities in the underlying isolated zones and suggesting that much of the moderately high permeability in the cored section resides in the extrusive basement. The injection tests were conducted at low rates, and the pressure records are well behaved. Injection at similar rates produced somewhat greater pressure rises at the deeper inflation point, where a shorter zone was isolated. This suggests that the transmissivity of the zone between the casing shoe and the second inflation point is not insignificant. Careful post-cruise processing and interpretation will be required to quantify the transmissivity and permeability values, but the data from the packer experiments in Hole 1027C appear to be of sufficient quality to document the permeability structure in the complex sequence cored at the sediment/basement contact in the hole.

CORK EXPERIMENTS

CORK instruments were successfully deployed in both Holes 1026B and 1027C to seal the holes and allow long-term monitoring of in situ temperatures and pressures, particularly in uppermost basement. As described by Davis et al. (1992), each CORK consists of a seal in the reentry cone, a long-term data logger, a pressure sensor inside the seal as well as a reference pressure gauge outside the seal, and a cable with 10 thermistors. In addition, each CORK experiment included an “OsmoSampler” (see “Methods” chapter, this volume) carried on the bottom of the thermistor cable. The configurations of the sensor strings deployed in Holes 1026B and 1027C are shown in Figure 62, and relevant data are summarized in Table 26. No data were available from the CORK experiments during Leg 168; the first data recovery is planned for the summer of 1997 using the ROV *Jason.*

Several unusual aspects of hole preparation and/or CORK deployment in these two holes should be noted. First, hole conditions were very poor in the entire open-hole section of Hole 1026B, and deployment of the CORK sensor string beyond the casing and into the basement section first required emplacement of a liner fabricated out of scrap drill pipe (Fig. 62). Second, the CORK was deployed in this hole about 20 days after installation of the liner; the deployment had been scheduled earlier but was postponed twice because of poor weather. Third, in this time period, Hole 1026B began to produce formation fluids (see “Thermal Studies” section, this chapter), indicating that this CORK should record a formation overpressure. Finally, hole conditions were much better in Hole 1027C, but the total depth of the hole was about 17 m greater than the cable prepared before the leg for the hole; the deepest thermistor in the cable reached only to just above extrusive basement. We fabricated an extension to this cable to place a thermistor and the OsmoSampler within extrusive basement. This required running a lead from the breakout for thermistor 5 outside the cable to the bottom of the extension. Unfortunately, the final check of logger data during deployment, conducted with the cable suspended in the pipe below the rig floor, shows poor data from this thermistor. We surmise that this was due to damage to the external leads to this thermistor, probably caused by excessive detorquing and stretching of the polypropylene rope used as the strength member for the cable extension.

REFERENCES

Alt, J.C., Kinoshita, H., Stokking, L.B., et al., 1993. *Proc. ODP, Init. Repts.,* 148: College Station, TX (Ocean Drilling Program).

Andrews, A.J., 1977. Low-temperature fluid alteration of oceanic layer 2 basalts, DSDP Leg 37. *Can. J. Earth Sci.,* 14:911–926.

Boyce, R.E., 1976. Definitions and laboratory techniques of compressional sound velocity parameters and wet-water content, wet-bulk density, and porosity parameters by gravimetric and gamma-ray attenuation techniques. *In* Schlanger, S.O., Jackson, E.D., et al., *Init. Repts. DSDP,* 33: Washington (U.S. Govt. Printing Office), 931–958.

Davis, E.E., Becker, K., Pettigrew, T., Carson, B., and MacDonald, R., 1992. CORK: a hydrologic seal and downhole observatory for deep-ocean boreholes. *In* Davis, E.E., Mottl, M.J., Fisher, A.T., et al., *Proc. ODP, Init. Repts.,* 139: College Station, TX (Ocean Drilling Program), 43–53.

Davis, E.E., Mottl, M.J., Fisher, A.T., et al., 1992. *Proc. ODP, Init. Repts.,* 139: College Station, TX (Ocean Drilling Program).

Davis, E.E., Wang, K., He, J., Chapman, D.S., Villinger, H., and Rosenberger, A., 1997. An unequivocal case for high Nusselt-number hydrothermal convection in sediment-buried igneous oceanic crust. *Earth Planet. Sci. Lett.,* 146:137–150.

Espitalié, J., Laporte, J.L., Leplat, P., Madec, M., Marquis, F., Paulet, J., and Boutefeu, A., 1977. Méthode rapide de caractérisation des roches mères, de leur potentiel pétrolier et de leur degré d’évolution. *Rev. Inst. Fr. Pet.,* 32:23–42.

Fisher, A.T., Becker, K., Narasimhan, T.N., Langseth, M.G., and Mottl, M.J., 1990. Passive, off-axis convection through the southern flank of the Costa Rica rift. *J. Geophys. Res.,* 95:9343–9370.

Flood, R.H., Vernon, R.H., Shaw, S.E., and Chappell, B.W., 1977. Origin of pyroxene-plagioclase aggregates in a rhyodacite. *Contrib. Mineral. Petrol.,* 60:299–306

Honnorez, J., Laverne, C., Hubberten, H.-W., Emmermann, R., and Muehlenbachs, K., 1983. Alteration processes in Layer 2 basalts from Deep Sea Drilling Project Hole 504B, Costa Rica Rift. *In* Cann, J.R., Langseth, M.G., Honnorez, J., Von Herzen, R.P., White, S.M., et al., *Init. Repts. DSDP,* 69: Washington (U.S. Govt. Printing Office), 509–546.

Laverne, C., Belarouchi, A., and Honnorez, J., 1996. Alteration mineralogy and chemistry of the upper oceanic crust from Hole 896A, Costa Rica Rift. *In* Alt, J.C., Kinoshita, H., Stokking, L.B., and Michael, P.J. (Eds.), *Proc. ODP, Sci. Results,* 148: College Station, TX (Ocean Drilling Program), 151–170.

Mottl, M.J., 1989. Hydrothermal convection, reaction, and diffusion in sediments on the Costa Rica Rift flank: pore-water evidence from ODP Sites 677 and 678. *In* Becker, K., Sakai, H., et al., *Proc. ODP, Sci. Results,* 111: College Station, TX (Ocean Drilling Program), 195–213.

Scarfe, C.M., and Fujii, T., 1987. Petrology of crystal clots in the pumice of Mount St Helens March 19, 1982 eruption: significant role of Fe-Ti oxide crystallization *J. Volcanol. Geotherm. Res.,* 34:1–14

Shipboard Scientific Party, 1987. Site 646. *In* Srivastava, S.P., Arthur, M., Clement, B., et al., *Proc. ODP, Init. Repts.,* 105: College Station, TX (Ocean Drilling Program), 419–674.

————, 1994. Site 888. *In* Westbrook, G.K., Carson, B., Musgrave, R.J., et al., *Proc. ODP, Init. Repts.,* 146 (Pt. 1): College Station, TX (Ocean Drilling Program), 55–125.

Tartarotti, P., Vanko, D.A., Harper, G.D., and Dilek, Y., 1996. Crack-seal veins in upper Layer 2 in Hole 896A. *In* Alt, J.C., Kinoshita, H., Stokking, L.B., and Michael, P.J. (Eds.), *Proc. ODP, Sci. Results,* 148: College Station, TX (Ocean Drilling Program), 281–288.

Teagle, D.A.H., Alt, J.C., Bach, W., Halliday, A.N., and Erzinger, J., 1996. Alteration of upper ocean crust in a ridge-flank hydrothermal upflow zone: mineral, chemical, and isotopic constraints from Hole 896A. *In* Alt, J.C., Kinoshita, H., Stokking, L.B., and Michael, P.J. (Eds.), *Proc. ODP, Sci. Results,* 148: College Station, TX (Ocean Drilling Program), 119–150.

Thomson, R.E., Davis, E.E., and Burd, B.J., 1995. Hydrothermal venting and geothermal heating in Cascadia Basin. *J. Geophys. Res.,* 100:6121–6141.

Tissot, B.P., and Welte, D.H., 1984. *Petroleum Formation and Occurrence* (2nd ed.): Heidelberg (Springer-Verlag).

Wheat, C.G., and Tribble, J.S., 1994. Diagenesis of amorphous silica in Middle Valley, Juan de Fuca Ridge. *In* Mottl, M.J., Davis, E.E., Fisher, A.T., and Slack, J.F. (Eds.), *Proc. ODP, Sci. Results,* 139: College Station, TX (Ocean Drilling Program), 341–349.

Whiticar, M.J., Faber, E., Whelan, J.K., and Simoneit, B.R.T., 1994. Thermogenic and bacterial hydrocarbon gases (free and sorbed) in Middle Valley, Juan de Fuca Ridge, Leg 139. *In* Mottl, M.J., Davis, E.E., Fisher, A.T., and Slack, J.F. (Eds.), *Proc. ODP, Sci. Results,* 139: College Station, TX (Ocean Drilling Program), 467–477.

Ms 168IR-105

NOTE: For all sites drilled, core-description forms (“barrel sheets”) and core photographs can be found in Section 3, beginning on page 213. Smear-slide data and thin-section data can be found on CD-ROM. See Table of Contents for material contained on CD-ROM.

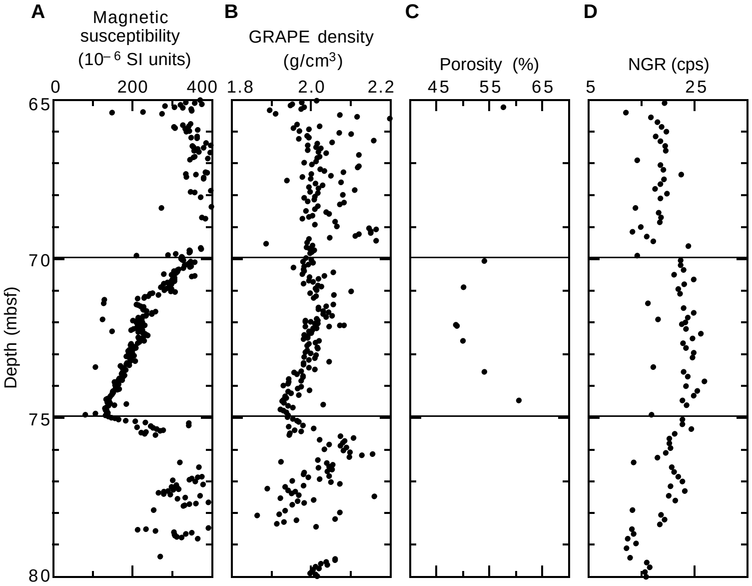

Figure 46. Plots of (**A**) magnetic susceptibility, (**B**) GRAPE bulk density, (**C**) IP porosity, and (**D**) natural gamma radiation for a fine-grained interval from Hole 1026A between 70 and 75 mbsf. Note the peak in GRAPE density and local minimum in IP porosity near 72 mbsf.

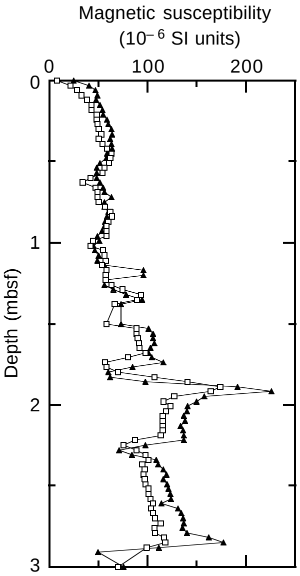

Figure 47. Magnetic susceptibility in sediment from the upper 3 mbsf of Holes 1026A and 1027B. A similar correlation is apparent in GRAPE bulk densities. Solid triangles = Hole 1027B; open squares = Hole 1026A.

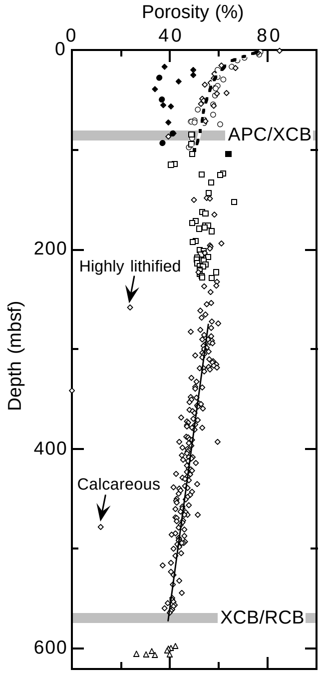

Figure 48. Porosity profile for Holes 1026A (circles), 1026C (squares), 1027B (diamonds), and 1027C (triangles). Porosity of mud (open symbols) decreases with depth as ϕ = 84.7 − 7.44 l*n*(*z*) for depths above approximately 100 mbsf, and ϕ = 71.0 − 0.06 *z* below approximately 280 mbsf, where ϕ is porosity (%) and *z* is depth (mbsf). Sand (solid symbols) has a lower porosity relative to mud at comparable depths, but it shows no general dependence on depth.

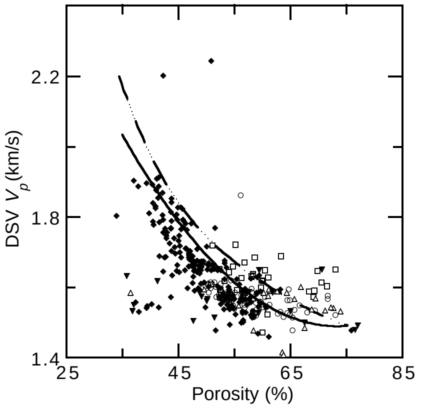

Figure 49. IP porosity vs. DSV velocity for Holes 1023A, 1024B, 1025B, 1026A, and 1027B. Curves shown are from relationships derived from Leg 105 data from the Labrador Sea (Shipboard Scientific Party, 1987) and from Leg 146 in Cascadia Basin (Shipboard Scientific Party, 1994). Open circles = Hole 1023A; open squares = Hole 1024B; open triangles = Hole 1025B; solid triangles = Hole 1026B; and solid diamonds = Hole 1027B. Dashed line = Leg 105; solid line = Leg 146.

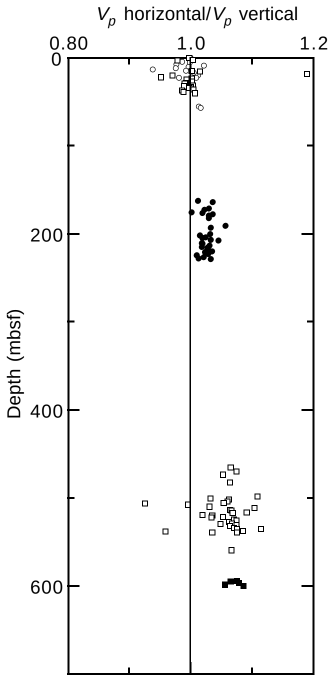

Figure 50. Velocity anisotropy for Holes 1026A (open circles), 1026C (solid circles), 1027B (open squares), and 1027C (solid squares).

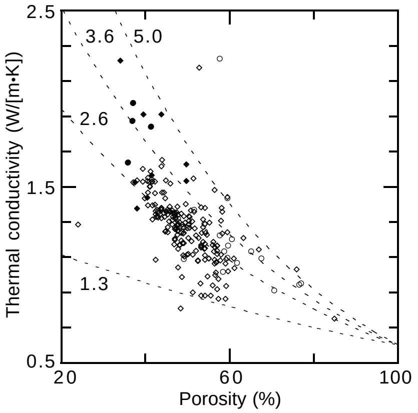

Figure 51. Porosity vs. thermal conductivity for mud (open symbols) and sand (solid symbols). The data are from Holes 1026A (circles), 1027B (squares), and 1025B (diamonds). The lines indicate theoretical values based on the geometric mean mixing model. The curve parameter is the matrix thermal conductivity in W/(m·K). Matrix thermal conductivities of 1.3 and 5.0 W/(m·K) represent the upper and lower limit; 3.6 W/(m·K) is the best fit for data from all of Hole 1026A and the upper 100 mbsf of Hole 1027B; and 2.6 W/(m·K) is the best fit for data from Hole 1027B between 150 and 580 mbsf.

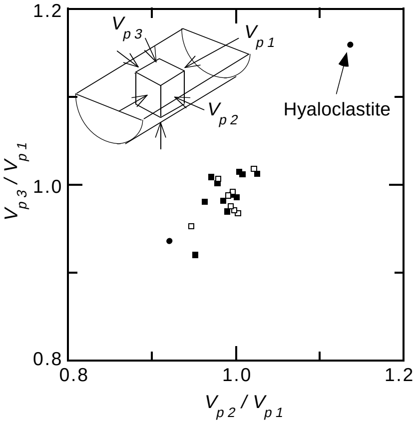

Figure 52. Velocity anisotropy for diabase, pillow basalt, and hyaoclastite from Sites 1026 and 1027. All velocities were measured with the Hamilton Frame Velocimeter. Solid circles = Hole 1026B pillow basalt and hyaloclastite; solid squares = Hole 1027C pillow basalt; and open squares = Hole 1027C diabase.

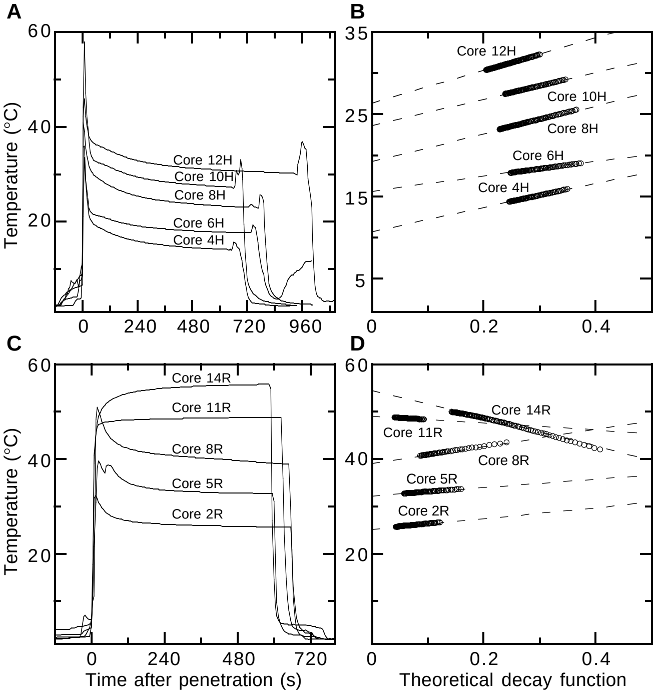

Figure 53. Temperature vs. time and temperature vs. theoretical decay functions for all tool deployments in Holes 1026A and 1026C. **A.** Temperature vs. time following tool penetration for APC tool 11 in Hole 1026A. **B.** Temperature vs. the APC tool theoretical decay function for Hole 1026A measurements, showing selected observations (circles) and extrapolated final temperatures (intersection of dashed lines with ordinate). **C.** Temperature vs. time following tool penetration for the DVTP in Hole 1026C. **D.** Temperature vs. the DVTP theoretical decay function in Hole 1026C, showing selected observations (circles) and extrapolated final temperatures (intersection of dashed lines with ordinate).

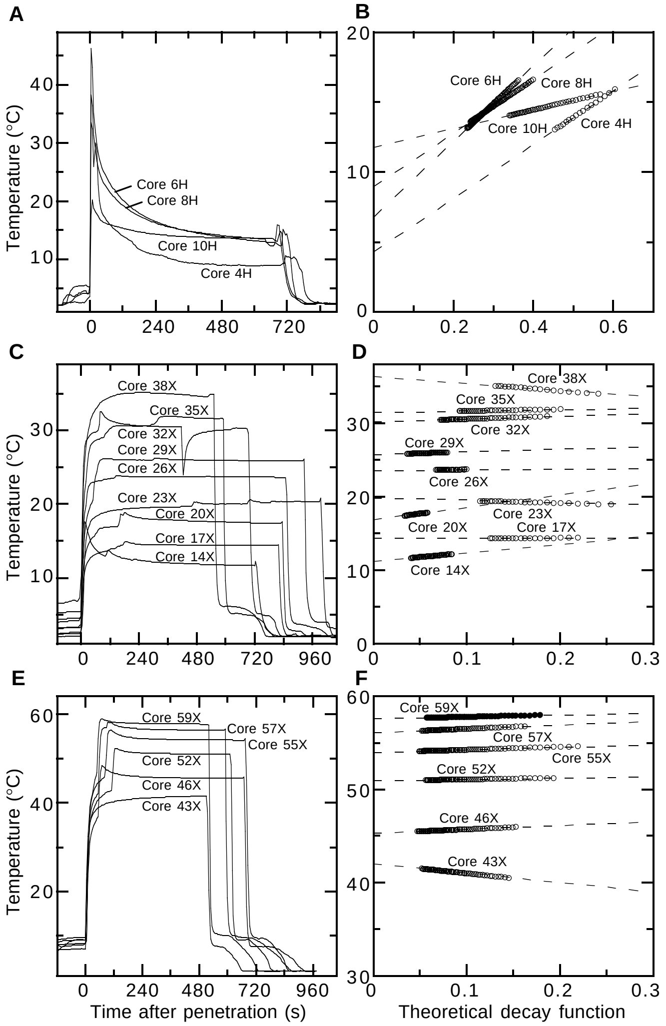

Figure 54. Temperature vs. time and temperature vs. theoretical decay functions for most tool deployments in Hole 1027B. Successful DVTP measurements are split into several figures for clarity. Symbols as in Figure 53. **A.** Temperature vs. time following tool penetration for APC tool 11. **B.** Temperature vs. the APC tool theoretical decay function for APC tool 11. **C.** Temperature vs. time following tool penetration for nine deployments of the DVTP. **D.** Temperature vs. the DVTP theoretical decay function for the nine deployments shown in C. **E.** Temperature vs. time following tool penetration for six deployments of the DVTP. **F.** Temperature vs. the DVTP theoretical decay function for the six deployments shown in E.

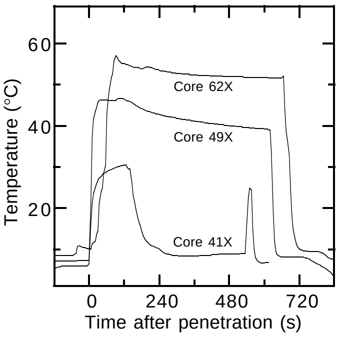

Figure 55. Temperature vs. time following penetration of three DVTP deployments in Hole 1027B that did not provide useful constraints on in situ temperatures because of insufficient probe penetration, probe motion, or splitting of the formation.

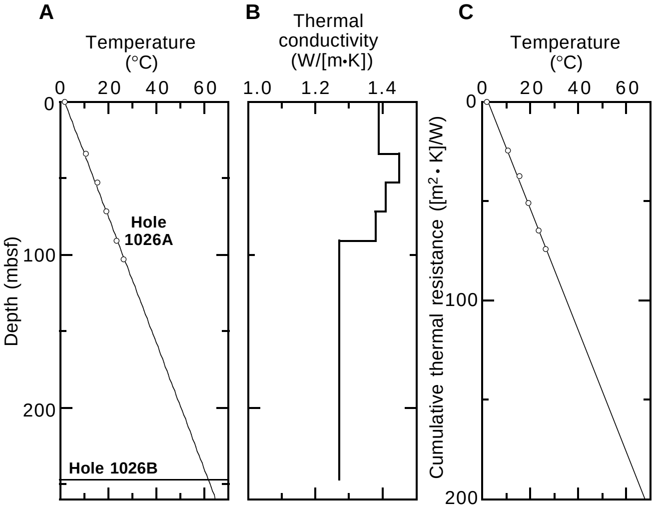

Figure 56. **A.** Equilibrium temperatures vs. depth within Hole 1026A. All data were collected with the APC tool. The range in estimated temperatures shown in Table 24 (based on different assumed thermal conductivities) is generally smaller than the symbols used to represent final temperature values. The subvertical line is a least-squares best fit of all data, including a bottom-water temperature of 1.85°C at the seafloor. The horizontal line indicates the depth to basement in nearby Hole 1026B. **B.** Calculated thermal conductivity vs. depth profile, based on a lithology-weighted harmonic mean of measured values within depth intervals of temperature measurements. **C.** Bullard Plot showing heat flow in Hole 1026A. The line is the least-squares best fit of all data, including a bottom-water temperature of 1.85°C at the seafloor.

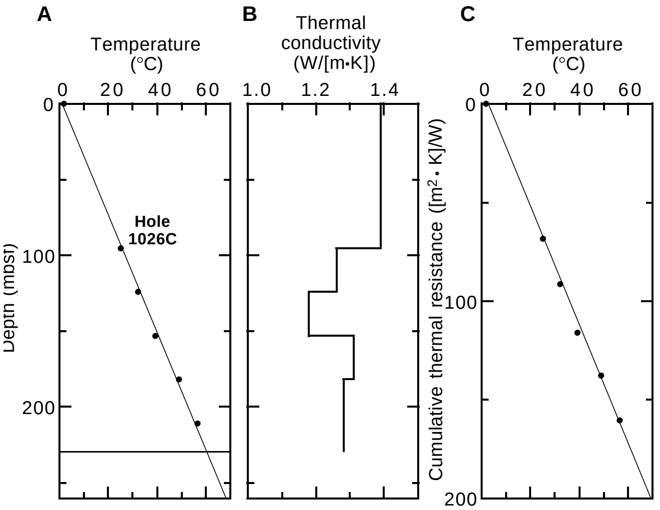

Figure 57. **A.** Equilibrium temperatures vs. depth within Hole 1026C. All data were collected with the DVTP. The subvertical line is the least-squares best fit of all subseafloor data. The horizontal line indicates the depth to basement. **B.** Calculated thermal conductivity vs. depth profile, based on a lithology-weighted harmonic mean of measured values within depth intervals of temperature measurements. **C.** Bullard plot showing heat flow in Hole 1026C. The line is the least-squares best fit of all subseafloor data.

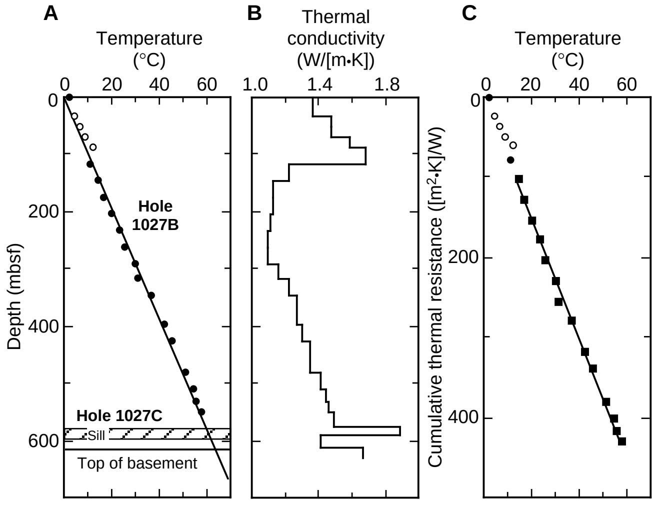

Figure 58. **A.** Equilibrium temperatures vs. depth within Hole 1027B. Open circles = APC tool 11 data; filled symbols = DVTP data. The subvertical line is the least-squares best fit of all data, including a bottom water temperature of 1.85°C at the seafloor. The position of the sill and the top of basement in nearby Hole 1027C are shown for reference. **B.** Calculated thermal conductivity vs. depth profile, based on a lithology-weighted harmonic mean of measured values within depth intervals of temperature measurements (see text for discussion of interval of low recovery). **C.** Bullard plot showing heat flow in Hole 1027B. Solid squares = DVTP data used in calculating heat flow and extrapolating to the temperature at the top of basement; open circles = data not used in these calculations. The line is the least-squares best fit of selected data.

Table 24. Extrapolated equilibrium temperatures from APC tool and DVTP deployments along the Rough Basement Transect.

				Extrapolated equilibrium temperature (°C)[b]		
Core	Tool	Depth (mbsf)	Error[a] (mbsf)	λ = 1.1 (W/[m·K])	λ = 1.0 (W/[m·K])	λ = 1.5 (W/[m·K])
168-1026A-						
4H	A11	33.9	1.0	10.73	11.07	9.79
6H	A11	52.9	1.0	15.60	15.77	14.96
8H	A11	71.9	1.0	19.29	19.67	18.32
10H	A11	90.9	1.0	23.60	23.91	22.58
12H	A11	102.9	8.5	26.35	26.61	25.96
168-1026C-						
2R	DVTP	95.2	1.0	25.22	25.22	25.22
5R	DVTP	124.1	1.0	32.23	32.25	32.22
8R	DVTP	153.0	1.0	39.15	39.06	39.20
11R	DVTP	181.8	1.0	49.09	49.09	49.09
14R	DVTP	210.7	1.0	56.60	56.61	56.58
168-1027B-						
4H	A11	32.7	1.0	4.29	4.30	3.38
6H	A11	51.7	1.0	6.77	7.28	5.08
8H	A11	70.7	1.0	8.95	9.31	7.64
10H	A11	87.7	1.0	11.76	11.85	11.34
14X	DVTP	118.0	1.0	11.19	11.19	11.19
17X	DVTP	147.0	1.0	14.32	14.32	14.32
20X	DVTP	176.0	1.0	16.85	16.85	16.85
23X	DVTP	204.0	1.0	19.83	19.83	19.83
26X	DVTP	232.0	1.0	23.58	23.58	23.58
29X	DVTP	261.0	1.0	25.69	25.70	25.71
32X	DVTP	290.0	1.0	30.14	30.14	30.14
35X	DVTP	319.0	1.0	31.43	31.43	31.43
38X	DVTP	348.0	1.0	36.34	36.34	36.34
41X	DVTP	377.0	1.0	—	—	—
43X	DVTP	396.0	1.0	42.05	42.05	42.05
46X	DVTP	425.0	1.0	45.27	45.27	45.27
49X	DVTP	454.0	1.0	—	—	—
52X	DVTP	482.0	1.0	50.91	50.91	50.91
55X	DVTP	511.0	1.0	53.95	53.95	53.95
57X	DVTP	531.3	1.0	56.07	56.07	56.07
59X	DVTP	550.0	1.0	57.57	57.57	57.57
62X	DVTP	573.0	1.0	—	—	—

Note: Tools: A11 = APC tool 11, and DVTP = Davis/Villinger Temperature Probe. — = data not processed.

[a] Depth error assumed to be no less than the uncertainty of individual depths because of pipe stretch and tides (1.0 m) or as much as the difference between core length and recovery for APC cores that failed to “stroke out” completely during deployment.

[b] A range of equilibrium temperatures is shown based on the assumed thermal conductivity of the sediments surrounding the probe tip. The range in final temperatures illustrates the minimum uncertainty in final temperatures. See text for discussion. The extrapolated temperatures determined using a sediment thermal conductivity of 1.1 W/(m·K) were used in Figures 53 and 54. No equilibrium temperatures were calculated for DVTP deployments 168-1027B-38X, 41X, 49X, and 62X because data records were irregular.

Table 25. Depth to basement, thermal gradient, heat flow, and extrapolated temperature at the top of basement for the Rough Basement sites.

Hole	Depth to basement[a] (m)	Thermal gradient[b] (°C/m)	Heat flow[b] (mW/m^2)	Basement temperature[c] (°C)
1026A	247.1	0.242	328	61.4
1026C	228.9	0.259	345	61.7
1027B	613.7	0.103	135	62.8

[a] See “Lithostratigraphy” section (this chapter) for explanation of how depths to basement were calculated. The depth listed for Hole 1026A is based on the driller’s interpretation in adjacent Hole 1026B. The depth listed for Hole 1027B was recorded in adjacent Hole 1027C for the presumed top of basement below sill.

[b] Based on least-squares best fit of all equilibrium temperature data.

[c] Extrapolation of Bullard plot to cumulative thermal resistance appropriate for top of basement.

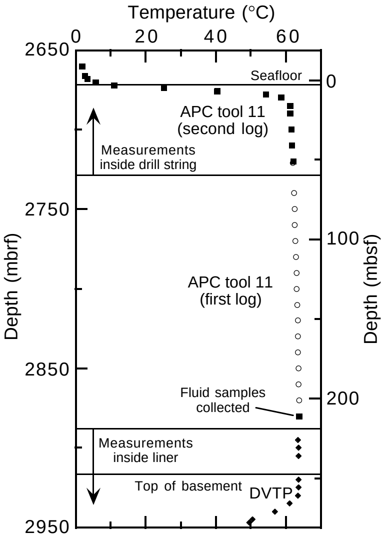

Figure 59. Open-hole temperatures vs. depth recorded with the DVTP and APC tool 11 (two deployments) in Hole 1026B. The tools were held at the depths shown for 2–3 min to allow thermal equilibration. See text for a discussion of the implications of this composite log for fluid flow into and up the borehole.

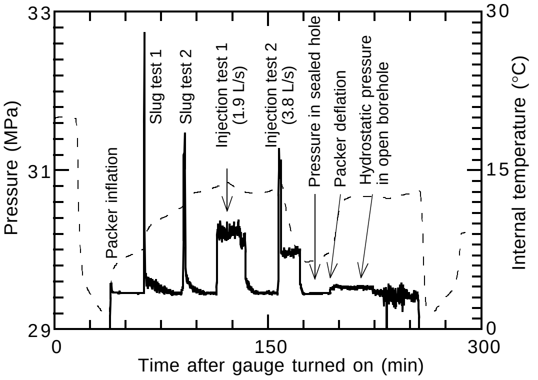

Figure 60. Pressures and internal temperatures recorded with a downhole electronic pressure gauge during the packer experiments in Hole 1026B, conducted with the packer in casing at 229.2 mbsf.

Table 26. Relevant time and depth data for the CORK experiments deployed in Holes 1026B and 1027C.

Hole:	1026B	1027C
Time/date of final basement coring (UTC):	1215 18 July	0700 17 July
Time/date CORK latched in cone (UTC):	1600 7 Aug	1910 21 July
Depths (mbsf):		
Basement	247.1	575.5
Casing shoe	248.5	578.4
Cored depth	295.2	632.4
Liner depth	217.9–285.9	No liner required
Fill level at CORK deployment	278.9	632.4; no fill
T10	77.8	176.8
T9	132.8	311.8
T8	187.8	446.8
T7	242.8	581.8
T6	247.8	586.8
T5	252.8	625
T4	257.8	596.8
T3	262.8	601.8
T2	267.8	606.8
T1	273.3	612.3
OsmoSampler orifice	273.6	624
Sinker bar	273.8–277.3	625.8–629.3

Notes: UTC = Universal Time Coordinated. T = thermistor (e.g., T10 = thermistor 10).

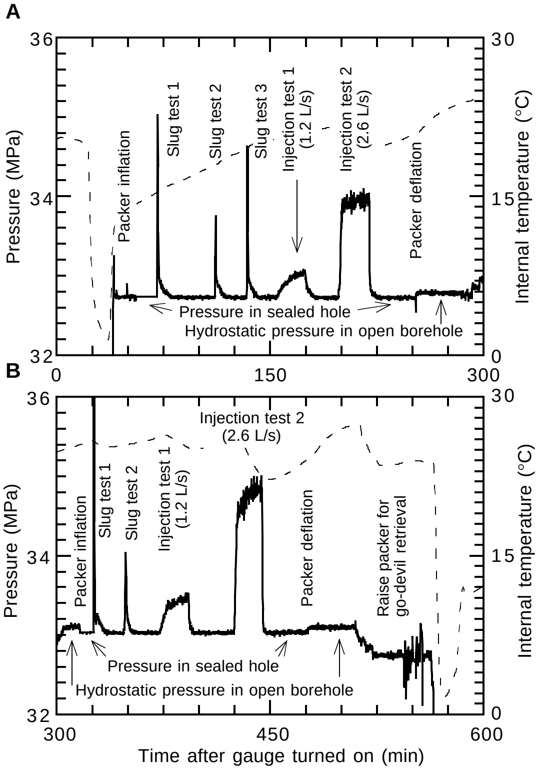

Figure 61. Pressures and internal temperatures recorded with a downhole electronic gauge during the two packer inflations in Hole 1027C. **A.** Packer inflated in casing at 560.7 mbsf. **B.** Packer inflated at 590.7 mbsf within a massive sill. Note that the pressure gauge was left in place for the full sequence of testing, such that A and B constitute two halves of a 10-hr record.

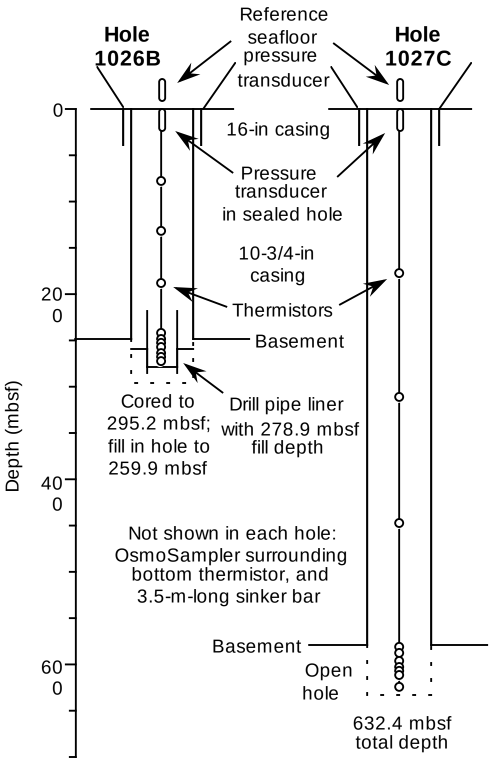

Figure 62. Configurations of the downhole sensor strings deployed in the CORK experiments in Holes 1026B and 1027C.

Previous Chapter
Table of Contents
Next Chapter